3D Modelling of Brain Metastasis Microenvironment for Evaluation of Tumour-Stromal Interactions

Birgitte Feginn Berle

This thesis is submitted in partial fulfilment of the requirements for the degree of Master in Medical Biology

Biomedicine The Faculty of Medicine and Dentistry - Department of

Biomedicine University of Bergen

Spring 2023

Acknowledgement:

First and foremost, I would like to express my utmost gratitude to Professor Frits Thorsen for his guidance and support throughout the year. His insightful feedback and expertise have been invaluable to my academic journey. I am sincerely grateful for the opportunity to work under his mentorship.

I want to thank my co-supervisor Emma Rigg, for your patience and support throughout the year. Thank you for your valuable input and for being a source of inspiration and encouragement.

Thank you to the technicians, Halala Sdik Saed and Aurea Castilho, for your assistance in the lab and to all those in the Translational Cancer Research group who have helped me throughout the duration of my thesis. Thank you to the personnel at MIC, Endy Spriet, Hege Avsnes Dale, and Hans Olav Rolfsnes, for your training on instruments around the faculty. I would also like to thank Professor Hrvoje Miletic for his assistance in interpreting the immunohistochemistry results.

Thank you to Annabeth and Magnus for the long lunch breaks and conversations in the cell lab. I am grateful to Inger Johanne and Hanna for their company during long days in the study room and for the endless breaks we took over much-needed cups of coffee.

I especially want to thank my family and friends in Bergen and afar for their immeasurable support and motivation throughout my thesis.

Last, but certainly not least, thank you to the University of Bergen, Department of Biomedicine, for offering such an insightful and hands-on master's experience. It has been of immense value to my educational progress.

Bergen, May 2023
Birgitte Feginn Berle

Table of Contents

Abbreviations:

BBB = blood-brain barrier
BM = brain metastases
BSC = biological safety cabinet
CAF = cancer-associated fibroblast
CNS = central nervous system
CT = computed tomography
CTC = circulating tumour cells
DAB = Diaminobenzidine
DLS = dynamic light scattering
DMEM = Dulbecco's modified eagle medium
DMSO = dimethyl sulfoxide
EC = endothelial cell
ECM = extracellular matrix
EMT = epithelial-mesenchymal transition
ER = endoplasmic reticulum
ER = estrogen
ESCRT = endosomal sorting complex required for transport
EV = extracellular vesicle
FBS = fetal bovine serum
FFPE = formalin fixed paraffin embedded
HER2 = human epidermal growth factor receptor 2
HLA = human leukocyte antigen
HRP = horseradish peroxidase
IFN-α = interferon-alpha
IHC = immunohistochemistry
ILV = intraluminal vesicle
IP = incidence proportion
ISEV = The International Society for Extracellular Vesicles
LDS = lithium dodecyl sulfate
MC = methylcellulose
MDCSS = Metropolitan Detroit Cancer Surveillance System
MHC = major histocompatibility complex
miRNA = microRNA
MISEV = The Minimal Information for Studies of Extracellular Vesicles
MMP = matrix metalloproteinases
MRI = magnetic resonance imaging
mRNA = messenger RNA
MVB = multivesicular body
NF-kB = nuclear factor kappa-light-chain-enhancer of activated B cells
NHA = normal human astrocyte
NK = natural killer
NSCLC = non-small cell lung cancer
O/N = overnight
PBS = phosphate-buffered saline
PDL1 = programmed cell death 1 ligand 1
PFA = paraformaldehyde
PR = progesterone
RA = reactive astrocyte
REC = Regional Ethical Committee

ROS = reactive oxygen species
RPM = revolutions per min
rRNA = ribosomal RNA
SCLC = small cell lung cancer
SD = standard deviation
SDS = sodium dodecyl sulfate
SEC = size exclusion chromatography
SPION = superparamagnetic carboxyl iron oxide nanoparticle
SRS = stereotactic radiosurgery
STAT-1 = signal transducer and activator of transcription 1
STR = short tandem repeat
T2W = T2 weighted MRI
TEM = transmission electron microscopy
TJ = tight junction
TME = tumour microenvironment
TNBC = triple-negative breast cancer
TNF- α = tumour necrosis factor-alpha
tRNA = transfer RNA
VEGF = vascular endothelial growth factor
WBRT = whole-brain radiotherapy

1.0 Summary:

Brain metastases (BM) occur when cancer cells from the primary location spread to the brain through the bloodstream. BM affects approximately 20-40 % of cancer patients, with the majority originating from lung, breast, and skin cancers. If left untreated, the median survival time is usually only one month, and aggressive treatment only extends survival to around four months. Despite the advances in modern medicine, the blood-brain barrier (BBB) poses a significant challenge in treating BM, restricting the entry of approximately 98 % of chemotherapeutic drugs into the brain. Thus, better model systems are needed to understand the complex interplay between cancer cells and normal brain cells.

In order to generate novel models, a range of cell lines derived from lung, breast and skin BM were characterized to understand their behaviour *in vitro*. Subsequently, their distinguishing features were analyzed to identify the most suitable candidates for generating three-dimensional models, which can later be used for drug testing. We found that LBM1, derived from a lung cancer BM, and H16, developed from a melanoma BM, were the best candidates for spheroid formation. The two cell lines underwent treatment with thioridazine, an antipsychotic drug that has been previously tested by our group on various melanoma BM cell lines and demonstrated a significant reduction in their viability. Comparable results were seen with LBM1 and H16 cells.

The potential of LBM1- and H16-derived exosomes to serve as imaging agents was also investigated, with focus on iron oxide labelling using carboxyl-coated superparamagnetic iron oxide nanoparticles (SPIONs), through electroporation. To verify the electroporation, further investigation is necessary to confirm the presence of the iron oxide particles within the exosomes. However, dextran-coated SPIONs were successfully internalised by LBM1 cells following 24 h incubation, suggesting its potential labelling attributes and potential uptake by LBM1-derived exosomes.

Lastly, LBM1 and H16 cells were injected intracardially into four non-obese diabetic/severe combined immunodeficient (NOD-SCID) mice each for evaluation of their tumourigenic potential. Despite a small sample size, H16-injected mice demonstrated a 23 % increased survival time compared to LBM1-injected mice, but no tumours were observed at week 4. In contrast, 3 out of 4 LBM1-injected mice displayed brain tumours four weeks following injection, thus demonstrating its potential as a model system for future BM research.

2.0 Introduction:

2.1 What is Cancer?

Cancer is a group of diseases characterised by an abnormal and uncontrollable growth of cells, which can remain localised or spread to other parts of the body. The body comprises around 30 trillion cells, most of which divide and multiply to replace old or damaged cells once they reach the end of their lifespan. However, there are instances when this orderly process fails, and abnormal or damaged cells continue to multiply. These cells can accumulate, and form masses of tissue known as tumours. They can be malignant, meaning they are cancerous, or benign, meaning they are not cancerous. Malignant tumours can infiltrate surrounding tissues and spread to far-off areas of the body, forming new tumours in a process known as metastasis[1]. Contrarily, benign tumours typically do not present a significant risk to surrounding tissues unless their growth causes compression or pressure on vital organs. When surgically removed, they do not typically return, unlike malignant tumours, which can reoccur following treatment.

More than half of cancers seen in the clinic today are preventable, as most are a consequence of modifiable causes such as tobacco use, obesity, and physical inactivity. Despite this, the cancer burden has increased tremendously in the past 60 years, due to changes in everyday habits in combination with longer life expectancies in the developing world[2]. Environmental effects can cause cancer through DNA damage, hormonal imbalance, or inflammation and irritation. Evidence suggests that tumour formation in humans is a gradual process that transforms normal cells into malignant ones by acquiring genetic mutations. Such genetic mutations each offer a growth benefit which ultimately can lead to the formation of a viable tumour[3]. This concept is reflected in Vogelstein and Kinzler's review[4], stating that “cancer is fundamentally a genetic disease.”

2.2 The Hallmarks of Cancer

All cancer cells that proceed to malignancy exhibit eight hallmarks[5] that jointly facilitate and permit their expansion and spread. These include:

1. *Abnormal cell growth and division in the absence of growth signals*: Cancer cells can surpass their expected lifespan, unlike normal cells, whose growth is regulated by growth factors and hormones. Mutations, especially in those encoding for kinases and kinase

receptors[6], result in uncontrolled signalling pathways leaving cancer cells resistant and independent of growth signals[7].

2. *Unrestricted growth and division despite signals to stop:* Cancer cells evade multiple regulatory mechanisms to remain proliferative. Dysregulation of tumour suppressor genes as a result of mutations leads to the activation of aberrantly functioning signalling pathways continuously driving the proliferation of cancer cells[8].
3. *Resistance to programmed cell death (apoptosis):* Apoptosis is a highly regulated type of programmed cell death in response to unrepairable DNA damage. Apoptosis plays a crucial role in preventing cancer development by inducing cells to undergo self-destruction[9] by increasing the expression of anti-apoptotic genes (e.g., Bcl-2) and decreasing the expression of pro-apoptotic genes (e.g., Bax)[10,11].
4. *Unlimited cell replication potential*: Telomerase repression prevents unlimited cell replication, leading to cellular senescence. In cancer cells, telomerase activity is amplified, leading to longer telomeres allowing cell lineages to accumulate genetic changes that render the cells "immortal" [12,13].
5. *New blood vessel (angiogenesis) promotion*: Angiogenesis enables tumour cells to access nutrients and oxygen and eliminates metabolic waste while facilitating the spread of cancer cells via entry into the newly-formed vessels[14].
6. *Invasion of tissue and spreading to other parts of the body*: The ability of cancer cells to overcome barriers in the surrounding tissue, establish themselves and grow, is facilitated by communication between the cancer cells and the tumour microenvironment. This behaviour is determined by genetic and epigenetic changes both within the cancer cells and the tumour microenvironment (TME)[15].
7. *Reprogramming of cellular metabolism*: Cancer metabolism plays a vital role in tumour growth as they require more energy than normal cells. The enhanced metabolism of cancer cells supports increased growth, spread to other organs, and thus adaptation to different tissues. It is caused by mutations in oncogenes and tumour-suppressor genes, leading to increased production of i.e. nitric oxide and reactive oxygen species (ROS), contributing to inflammation[16].
8. *Avoiding immune destruction*: Cancer cells escape destruction by the immune system by altering their antigenicity and immunogenicity and establishing an immunosuppressing microenvironment. This occurs when the immune system selects cancer cells with missing or mutated tumour antigens, or when the cancer cells have problems presenting antigens, such as loss of major histocompatibility complex (MHC)[17].

Independently, these hallmarks fall short of encompassing the complexity of the routes into malignantly progressed tumours. In light of this, Weinberg and Hanahan added new elements to the list in 2011, referred to as "enabling characteristics" in an updated version of "Hallmarks of Cancer" [5,18]. The first of which is genome instability, which relates to the malfunction of DNA monitoring and repair enzymes due to, for example, mutated p53 tumour suppressor proteins. P53 aims to preserve the genetic sequence by activating apoptosis in the case of severe DNA damage[19-21]. The second enabling characteristic is tumour-promoting inflammation, emerging due to the interplay between cancer, stromal, and inflammatory cells. This forms a complex microenvironment where tumour cells stimulate the release of inflammatory mediators and attract immune cells[22,23].

Specific cancer cell characteristics are intrinsic, while others arise from interactions between the cancer cells and their microenvironment. These features can be viewed as susceptibilities within a neoplasm, thus presenting opportunities for therapeutic interventions[24].

2.3 The Metastatic Cascade

Tumour cells can detach from the primary lesion and circulate throughout the body to colonise in distal tissues. This progression, referred to as the metastatic cascade, comprises a series of events that the detached cells must navigate to successfully establish a secondary tumour[25]. These include invasion into surrounding tissues, intravasation into the circulatory and/or lymphatic system, survival within the circulatory system, arrest and extravasation, and growth of micro- and macro-metastases at secondary sites[26].

At a certain point during tumour cell proliferation, the demand for oxygen and nutrients is too large for the environment to support its growth, leading to hypoxia, a state of inadequate levels of oxygen to maintain tissue homeostasis[27]. This would typically result in apoptosis[28], but in the case of cancer cells, they have acquired mutations providing protection against such surroundings. Consequently, cells of the microenvironment surrounding the tumour secrete angiogenic factors as a counteractive measure, ultimately facilitating further survival of the tumour cells and providing means of spreading[29].

During local invasion, cancer cells secrete matrix metalloproteinases (MMPs) that break down proteins such as collagen in the extracellular matrix (ECM), thereby disrupting the basal membrane. This allows the cancer cells to detach from the tissue and acquire changes enabling survival in the bloodstream and connective tissue. This process, known as epithelial-

mesenchymal transition (EMT), enables cancer cells to acquire mesenchymal features by modifying their cytoskeleton and switching from E-cadherin to N-cadherin expression[30], allowing them to intravasate through endothelial cells (ECs) of the blood vessels. The most critical stage of the metastatic cascade involves the survival and adaptation of circulating tumour cells (CTCs) to the bloodstream environment[29,31]. Cancer cells can reach the circulation as single cells or clusters, with the latter showing higher metastatic potential[32]. During transit, tumour cells are exposed to hemodynamic forces, immunological stress, and collisions with normal cells such as blood cells and ECs, thus impacting cancer cell survival. Only CTCs that overcome these stressors, in addition to immunosurveillance, will adhere to the vascular endothelium at distant sites and exit the circulation[30].

To do so, CTCs must engage with ECs. Altered permeability of the endothelial barrier is induced by the CTCs and allows extravasation into the tissue[29]. These halted CTCs may release extracellular vesicles (EVs), or more precisely, exosomes. Exosomes can induce changes to the cytoskeleton of ECs, increasing the permeability of the endothelial border. This ultimately facilitates the passage of CTCs across the barrier[33].

Once the cancer cells have lodged in the premetastatic niche - a microenvironment that undergoes specific molecular and cellular changes to become a fertile site for CTCs to settle, they interact with the environment to facilitate their growth through access to nutrients, but most importantly, to evade immune destruction. Cancer cells evade immune surveillance through various strategies, including reduced antigen presentation through downregulation of human leukocyte antigen (HLA) genes and impairing their ability to present neoantigens[34]. They also decrease programmed cell death ligand 1 (PDL1) expression, which activates PD1-mediated signalling in T cells, thus downregulating T cell activities in the TME[35]. Recent evidence indicates that these mechanisms are amplified during metastasis formation[36], collectively promoting the growth of the newly arrived cancer cells.

2.4 Brain Metastasis (BM)

BM, also called secondary brain tumours, arise when cancer cells spread to the brain from their original site through the bloodstream. Amongst the most typical cancer types to metastasize to the brain are lung, breast, colon, kidney, and melanoma. Between 20-40 % of cancer patients develop BM[37], and due to better diagnostic abilities, as well as improved therapies of the primary tumours, this number is expected to increase[38].

BM is a severe health problem globally, with the median duration from the presentation with BM to death, being four months[39]. BM can give rise to further health issues beyond those directly attributed to the presence of BM, which include, neurological decline, reduced motor skills, and overall decreased quality of life[40]. Factors that impact the outlook in the presence of BM include the cancer stage at the time of diagnosis, the number of BM, and the type of treatment given[41].

BM can result in the formation of one or more tumours in the brain, often discovered at the same time as the primary tumour. Single BM is most often associated with improved overall survival, compared to patients with multiple brain lesions[42]. Symptoms directly related to the tumour(s) vary depending on the size, location, and number of tumours but include headache, changes in emotions, cognitive dysfunction, seizures, and nausea[43-46]. Treatment options include radiation therapy, either targeted or whole brain, surgical resection, and chemotherapy, and a combination is often used to achieve the best results.

2.4.1 Diagnosis of Brain Metastasis

Diagnosing BM involves contrast-enhanced magnetic resonance imaging (MRI) and computed tomography (CT) scannig[47]. In addition, stereotactic needle biopsies are used to acquire tissue biopsies in patients where the risk of resection exceeds the potential benefits[48]. Features that often characterise BM include lesions placed at grey-white matter junctions, smooth edges, and surrounding edema[46]. In addition to morphological features on imaging, immunohistochemical and molecular techniques are utilised for determining the characteristics of a metastatic neoplasm whose origin is uncertain[49].

2.4.2 Treatment of BM

Radiotherapy uses ionising radiation in high doses to destroy cancerous cells by damaging their DNA. Two main types of radiation therapy are used to treat metastatic brain tumours: whole-brain radiotherapy (WBRT) and stereotactic radiosurgery (SRS). WBRT exposes both healthy and cancerous tissue to radiation. Therefore, potential adverse effects limit the dosage. To reduce the damage to healthy tissue, WBRT is administered over multiple sessions to allow the normal tissue to recover. The use of WBRT has declined in recent years due to advancements in technology, providing a more targeted delivery of radiation. Although SRS has begun to replace some of the functions of WBRT, the latter continues to serve as a complementary therapy alongside other treatments[50]. SRS is a precise therapeutic

modality that utilises multiple converging beams of ionising radiation. The procedure uses three-dimensional imaging techniques to localise the tumour precisely, and numerous beams collectively deliver high doses of radiation while minimising exposure to surrounding healthy tissues. This optimised targeting ensures the maximum therapeutic effect while reducing the risk of radiation-induced morbidities[51].

Chemotherapeutic agents impede fast-growing cells in the body and are often combined with other treatments, such as surgery or radiation. The assertion that systemic chemotherapy is not a viable option for treating BM stems from the decreased effectiveness due to a limited ability to cross the intact blood-brain barrier (BBB). As BM develop and expands, the new blood vessels formed, lack the characteristic anatomical and physiological properties typically associated with the BBB[52]. Thus, to increase effectiveness, drugs that can cross the BBB or agents that alter its permeability must be investigated.

Corticosteroids temporarily relieve symptoms associated with increased intracranial pressure and oedema. They have been utilised for palliative care and, when used alongside surgery and radiation, can minimise toxicity associated with the treatment[53].

Immunotherapy is another promising approach for managing BM by boosting the ability of the immune system to target the destruction of cancerous cells selectively. For example, inhibitors that act against the checkpoint protein PD-1 (on T cells) or its binding partner PD-L1 (on tumour cells). When PD-L1 binds to PD-1, it inhibits the T cell-mediated killing of tumour cells. When blocking this interaction by binding a checkpoint inhibitor to either protein, it allows T cells to destruct the tumour cells[54].

Studies have demonstrated that modern imaging modalities combined with surgical excision of BM lead to longer survival and better local control, compared to radiosurgery[55]. Clinical guidelines for managing BM, state that surgical intervention should be considered for patients with a limited number and easily accessible tumours[56]. The most effective means of achieving local control of BM include preoperative structural and functional imaging and the utilisation of adjuvant therapies, such as SRS or WBRT, that can enhance the overall efficacy of the procedure[57].

Thioridazine is a dopamine receptor 2 antagonist that has previously been used in the treatment of schizophrenia and psychosis[58]. It has shown a strong cytotoxic effect on

melanoma BM cell lines and can cross an intact BBB[58], one of the major obstacles of many chemotherapeutic agents. These characteristics make the repurposing of thioridazine a compelling candidate for developing novel therapies for BM, while avoiding radiation-induced morbidities.

2.4.3 Causes and Risk Factors

Although it is currently unknown why some types of cancers commonly metastasise to the brain, patients with aggressive subtypes of cancer, such as EGFR-mutant lung cancer[59] and human epidermal growth factor receptor 2 (HER2)-positive breast cancer[60], are advised to undergo regular scanning to locate potential BM at an early stage. Additionally, some studies refer to higher age, advanced grade and stage as prognostic risk factors decreasing the overall survival of patients with lung cancer BM[61]. Consequently, early detection and timely management of BM can improve outcomes for such high-risk patient groups.

There is a multitude of molecular and cellular factors that allow transformed cells to metastasise to distant organs. This is an important area of research because, as systemic treatments become more effective at controlling local tumours, the impact of BM on patient morbidity and mortality will become more significant[62]. The seed and soil hypothesis, first proposed by Stephen Paget in 1889, suggests that the ability of cancer cells (seeds) to grow and form metastases in other organs (soil) depends on the interactions and properties of both the cancer cells and the target organ. By this, Paget's theory suggests that some cancers have a greater tendency to spread to the brain, such as lung, renal, breast, melanoma, and colorectal cancers[62] (**Table 2.4.3.1**). In contrast, other cancers, such as prostate, ovarian, uterine, thyroid, and liver do not typically spread to the brain, according to Leonard Weiss' 1992 analysis of autopsy data[63]. It is thought that the CTCs of certain cancers can survive in the brain, while others will not[62], although the specific mechanisms behind it are not fully understood. It is therefore presumed that the brain provides either an attractive or a hostile environment for the growth of CTCs, depending on the type of cancer they originate from (**Table 2.4.3.1**).

Table 2.4.3.1: Incidence of BM by primary tumour type: *Table adapted from [62].*

Primary site	Incidence of BM (%)
Lung and bronchus	19,9
Melanoma	6,9
Renal	6,5
Breast	5,1
Colorectal	1,8

The incidence of primary cancers varies by race, sex, and age[64], and so it is reasonable to believe that BM also differs by such demographic factors. Incidence Proportions (IPs) of lung, melanoma, renal, breast, and colorectal cancer, presented in **Table 2.4.3.2**, were determined based on a study of patients diagnosed from 1973-2001 by the Metropolitan Detroit Cancer Surveillance System (MDCSS)[65]. This was done to estimate the expected number of BM by demographic characteristics in the US. It is worth noting that a considerable variation in the IPs among different races, sex, and age groups was recorded.

Table 2.4.3.2: The proportion of patients with lung, renal, melanoma, breast, and colorectal cancer, with BM, broken down by race, sex, and age at diagnosis, represented as IPs (%): *Table adapted from [64].*

		Lung IP%	Melanoma IP%	Renal IP%	Breast IP%	Colorectal IP%
Race	White	19,4	7,1	6,8	4,6	1,8
	African American	21,8	11,7	5,3	7,4	2,0
	Other	21,7	8,9	3,9	5,6	0,9
Sex	Male	18,9	8,7	6,6	4,9	1,9
	Female	21,8	4,8	6,2	5,1	1,7
Age	20-39	25,8	5,5	4,3	10,0	2,2
	40-49	31,3	7,4	6,0	6,6	2,4
	50-59	26,3	8,5	8,8	6,4	2,8
	60-69	20,2	7,8	7,7	4,5	2,2
	70+	12,9	5,5	4,1	2,4	1,2
Total		**19,9**	**6,9**	**6,5**	**5,1**	**1,8**

Additionally, as research advances, factors like genetics and epidemiology may contribute to discoveries revealing why some tumour cells metastasise to the brain, and how to better treat them. However, such research is complicated due to the lethality of BM and the short lifespan of BM patients with aggressive subtypes[66]. There are also challenges related to the modelling of metastatic cancer due to the unique and complex brain microenvironment. To effectively address the clinical concern of BM, a comprehensive understanding of the biological processes is crucial. Unfortunately, significant portions of cancer research funding and

awareness are focused on the primary cancer sites[67]. This neglect is particularly problematic because around 90 % of cancer deaths are caused by metastasis[68]. In this respect, investing in research on BM is necessary to improve survival for this patient group.

2.5 Lung Cancer BM

Lung cancer is, as mentioned, one of the most common cancer types to spread to the brain. At the time of diagnosis, around 18-25 % of patients with small cell lung cancer (SCLC) have BM, and approximately 50 % of the patients will acquire central nervous system (CNS) metastases. While WBRT and corticosteroids are considered the primary treatment modalities for lung cancer BM, systemic chemotherapy may provide beneficial therapeutic effects for the patients[69]. At the time of primary diagnosis, BM is observed in around 7-10 % of patients with non-small cell lung cancer (NSCLC) and 20-40 % develop BM. The management strategies for NSCLC include surgical excision and advanced radiation techniques, such as SRS[70]. At autopsy, this condition is about 50 % more common than expected, based on the reported symptoms[69]. Patients diagnosed with BM typically have a limited life expectancy and a survival period of only 3-6 months with treament[71].

2.6 Melanoma BM

Melanoma has one of the highest propensities to metastasise to the brain, as more than 25 % of patients present with BM at the time of diagnosis of metastatic disease[72]. Additionally, BM is present in 36-54 % of the patients at autopsy[73]. The median survival for melanoma BM patients is 6 months following diagnosis, and the standard treatment for single brain metastasis is surgery and radiation therapy, but the outcome is typically poor. In cases of multiple BM, a combination of radiation and chemotherapy is often used[74]. One of the key factors contributing to the unfortunate outcomes in treating BM is the tendency for tumours to recur at the location where they were previously surgically resected and the appearance of new metastatic neoplasms in areas that were not addressed during surgery. This may result in a proliferation of tumours both within and outside the brain, ultimately leading to a poor prognosis[74].

2.7 Breast Cancer BM

Breast cancer is a prevalent cause of BM, affecting approximately 10-16 % of patients, while at autopsy, it is present in 30 % of the patients[75]. The prognosis and treatment options for BM from breast cancer depend on the molecular subtype of the tumour. Breast cancer displays notable phenotypic heterogeneity due to four molecularly distinct subtypes, with a diverse spectrum of tumour characteristics. The subtypes include luminal A (estrogen (ER)+, progesterone (PR)+, human epidermal growth factor receptor 2 (HER2) low), luminal B (ER+, PR+, HER2 +/-), HER2+ (ER-, PR-, HER2+) and triple-negative breast cancer (TNBC) (ER-, PR-, HER2-), in ascending order of histological grade[76]. In addition to affecting the incidence rates, the tumour subtypes act as a prognostic tool[77]. Luminal A patients have a good prognosis and metastasis to CNS occurs in ~10 % of the patients. Treatment options for hormone-positive tumours include hormone therapies, where luminal B patients exhibit decreased effects to hormone therapy. The survival of untreated luminal B patients is comparable to that of TNBC and HER2+ patients, which are widely referred to as high-risk subtypes[77].

2.8 The Tumour Microenvironment (TME)

Tumours are not composed of cancer cells alone, but also contain a complex mixture of other cells known as stromal cells (**Fig. 2.8**). Stromal cells play a critical role in the growth and progression of tumours[78]. For example, ECs, which make up blood vessels and promote angiogenesis, provide the tumour cells with the necessary nutrients and oxygen to survive. The degree of angiogenesis is determined by the level of angiogenic promoters and suppressors produced by the tumour cells and healthy cells. The blood vessels within tumours exhibit abnormal morphological changes depending on the organ of origin and its functional state[79]. Another type of stromal cell found within tumours is immune cells. These infiltrate the tumour from the bloodstream and shape the TME by, e.g., secreting inflammatory factors like tumour necrosis factor alpha (TNF-α), which triggers EMT, a process vital for the successful development of secondary malignant growths[78].

The combination of these stromal cells including e.g. fibroblasts, neutrophils, B and T cells, natural killer cells, and macrophages, participate in tumour progression[80] (**Fig. 2.8**). The importance of the TME in cancer progression has been well-documented for malignancies that originate outside of the brain[81], and recent findings suggest that targeting the TME may

be a promising approach in developing new cancer therapies[80]. Additionally, the TME has also been proposed as a valuable biomarker for predicting patient outcomes[81].

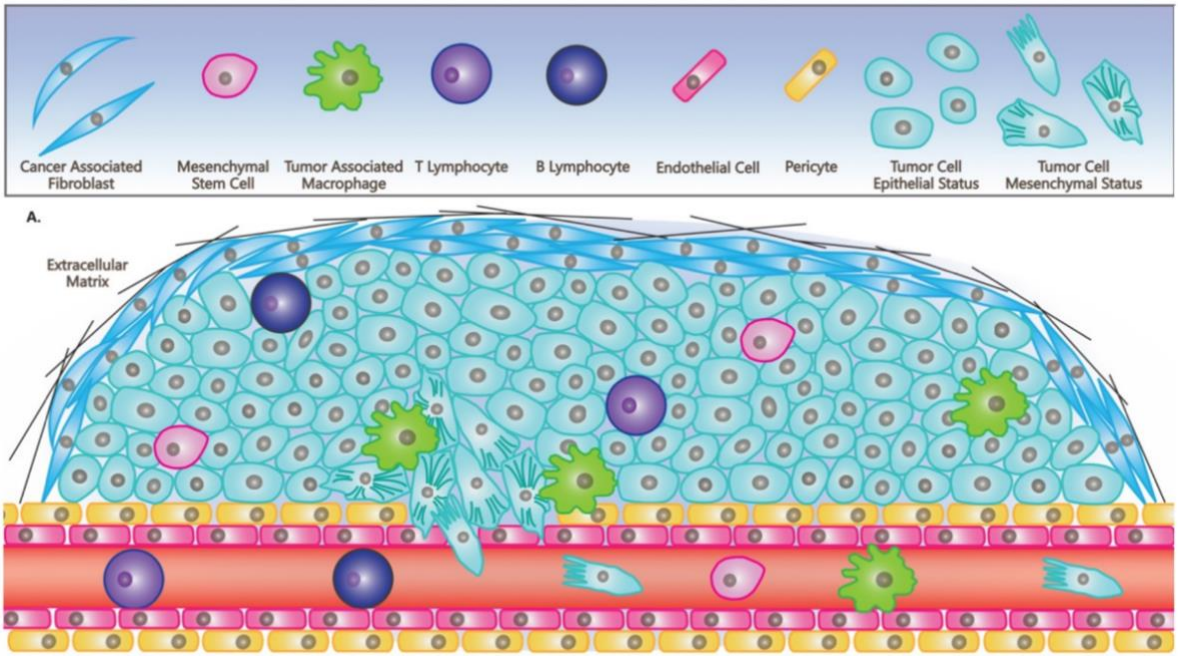

Figure 2.8 - Cells associated with the TME: *The microenvironment of a developing tumour is a complex and dynamic network of various cellular constituents. These include the rapidly dividing tumour cells, the structural support provided by the stromal cells, the blood vessels that nourish the tumour, and inflammatory cells that infiltrate the area. The TME plays a critical role in the growth, development, and progression of the tumour. Figure adapted from [78].*

2.9 The Brain Microenvironment

The CNS is composed of various types of cells unique to this microenvironment. The primary cell types in the brain include neurons, which transmit information through nerve impulses to other neurons, muscles, and tissues throughout the body, and glial cells, which provide structural support and are regulators of the development, protection, and function of synapses. The three main types of glial cells in the brain are microglia, astrocytes, and oligodendrocytes. Microglia are responsible for removing cellular debris and pathogens, modulating synaptic connections, and are essential for CNS tissue maturation[82]. One of the functions of glia in the adult nervous system is the formation of myelin sheaths around axons[83]. These myelin sheaths are composed of lipids and proteins produced by oligodendrocytes[84]. Myelination allows for the fast conduction of electrical signals along axons, which is essential for normal nervous system function. In addition to myelination, glial cells play a vital role in maintaining the appropriate concentrations of ions and neurotransmitters in the neuronal environment. Astrocytes, in particular, are responsible for

buffering extracellular potassium ions and releasing neurotransmitters, which helps to ensure proper neuronal function[83].

Within the brain microenvironment lies the BBB, a specialized structure that separates the brain from the bloodstream (**Fig. 2.9**). It plays a critical role in maintaining the integrity of the CNS and comprises specialized ECs that line the blood vessels that supply the brain. These cells are interconnected by junctional complexes, such as tight junctions (TJs) and adherens junctions, which help maintain the integrity of the BBB[85]. Surrounding the ECs are pericytes and astrocytic end-feet, which provide structural support and help to regulate the transport of molecules across the barrier[86]. The BBB is also surrounded by a basal lamina, a layer of the ECM that provides additional structural support and scaffolding[87].

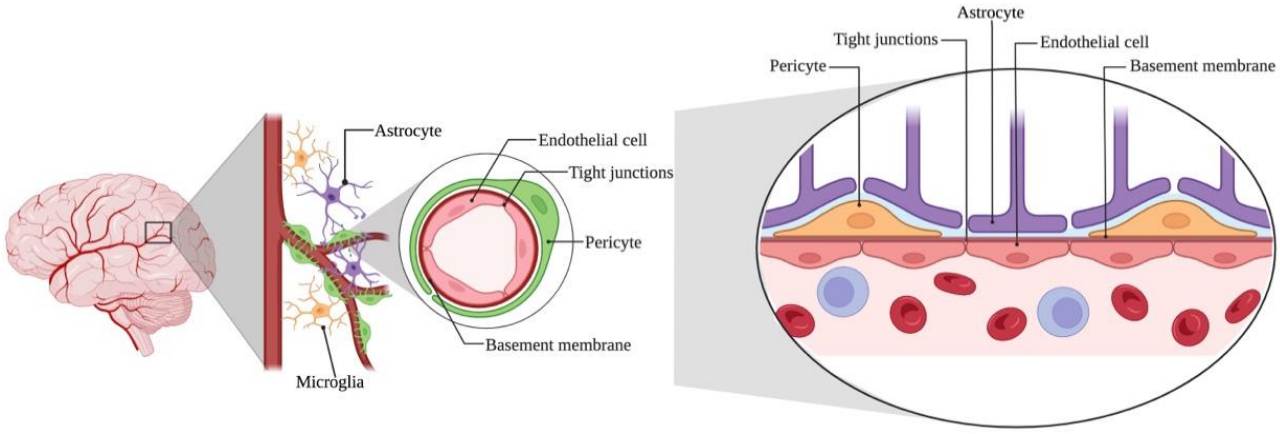

Figure 2.9 - The BBB: *The BBB is a selective semipermeable border composed of various cells, some of which are unique to the brain microenvironment. They all contribute to the integrity of the barrier, which prevents the non-selective crossing of solutes from circulating blood into the extracellular fluid of the CNS, where neurons reside. Created with BioRender.com with inspiration from [88].*

The process of BM presents unique challenges as the microenvironment in the brain is vastly different from that in other parts of the body. The interactions between tumour cells and the resident cells of the brain, such as astrocytes and microglia, and secreted factors from ECs and endogenous plasma factors, are ongoing topics of study to better understand the mechanisms responsible for cell-cell interactions in the brain. Thus, the entire brain microenvironment must be considered when studying BM[89].

2.9.1 Intercellular Communication Between Tumour Cells and Stromal Cells in the Brain

Due to their many functions and vital role in the brain, astrocytes play an essential role in the progression of cancer within the CNS. In the case of BM, astrocytes exhibit both pro- and anti-tumour functions. At the initial stages of tumour cell infiltration, astrocytes undergo a process called reactive gliosis. The astrocytes become activated and work to protect the brain through the secretion of growth factors and cytokines[90]. This process induces the death of cancer cells through the production of nitric oxide[91] and forming reactive astrocyte (RA) boundaries that help separate the cancerous lesion from the surrounding healthy brain tissue[92]. Through these mechanisms, astrocytes work to limit the spread of cancer cells in order to maintain the integrity of the brain. However, over time, this barrier of RAs around the tumour can promote tumour cell survival. Chen et al. [93] revealed that specific lung cancer cells express cadherins that release inflammatory cytokines from RAs. These include TNF- α and interferon-alpha (IFN-α), which thereupon activate the pro-proliferative signal transducer and activator of transcription 1 (STAT-1) and nuclear factor kappa-light-chain-enhancer of activated B cells (NF-kB) pathways in the CTCs. This ultimately induces proliferation as well as chemoprotection of the tumour cells[93]. Despite the initial tumour suppression by the astrocytic border, cadherin expression by the tumour cells causes successive astrocyte secretions and thereby chemically converts their influence to becoming promotive of tumour growth.

There is evidence that BM causes great stress to surrounding brain tissue, resulting in neuronal loss and neurological dysfunction[94]. In addition to the stress caused by tumour cells, persistent inflammation caused by RAs and microglia also contribute to neuronal death[92]. The seed and soil hypothesis suggests that for BM to be successful, tumour cells must possess the ability to adapt to the environment of the designated site, here, the neural environment. This idea is supported by recent findings uncovering evidence of tumour cells acquiring neuro-adaptive characteristics when they migrate to the brain, particularly in the case of breast cancer. The study by Neman and colleagues[95] revealed that metastatic breast cancer cells in the brain undergo metabolic changes and begin to exhibit GABAergic properties, which are typically associated with neurons. Tumour cells also form synapses with glutamatergic neurons due to their insufficient glutamate secretions, allowing them to utilise the glutamate secreted by these presynaptic neurons[96]. This example indicates that tumour cells adapt to

their new environment by shifting e.g., their metabolic requirements to thrive and successfully establish BM.

2.10 Extracellular Vesicles (EVs)

EVs are a complex and diverse set of membranous structures derived from all cell types. They include exosomes, microvesicles, and apoptotic bodies. Exosomes were initially discovered as a means for cells to eliminate unwanted cellular content. However, it has been found that exosomes also serve as vital mediators of intercellular communication by transporting proteins, metabolites, and nucleic acids to target cells[97]. The ability of exosomes to selectively deliver cargo to specific recipient cells underscores their potential utility as vehicles for therapeutic intervention in a range of pathological conditions.

Exosomes, the smallest type of EVs, range in size from 30 to 150 nm. Their biogenesis starts when the cell membrane invaginates to create multivesicular bodies (MVBs) that fuse with the plasma membrane. In contrast, microvesicles are vesicular structures shed by outward blebbing of the plasma membrane, with sizes ranging from 0,1 to 1,0 μm. Apoptotic bodies are the largest type of EVs ranging from 1-5μm[98], and are released by cells undergoing apoptosis (**Fig. 2.10.2**).

Cancer-derived EVs serve as a type of intercellular communication that facilitates cell survival, growth, and modulation of the tumour microenvironment to enhance the metastatic potential. Cancer cell-derived exosomes are critical players in their development and spread, by transporting molecules in the local and distant microenvironments. This exosome-mediated crosstalk triggers alterations in the recipient cells to prepare the microenvironment for the tumour cells through, e.g., the modulation of immune responses by exhibiting antigen-presenting properties, the reprogramming of stromal cells, and alteration of the ECM[99].

2.10.1 Exosomal Content and Molecular Composition

Exosomes carry molecular components that vary depending on the cell origin, environment, developmental stage, and epigenetics. They contain various RNA species such as messenger RNA (mRNAs), microRNAs (miRNA), ribosomal RNAs (rRNAs), and transfer RNAs (tRNAs) that can reflect epigenetic changes and biological functions of the cells. Exosomal protein profiles can also imply cancer mutations, protein expression patterns, and parental cell activity[99]. They also contain a range of proteins, including receptors, transcription

factors, enzymes, and ECM proteins, some specific to the cell of origin, such as MHC Class I and II, and others common across all exosomes. The common proteins include, e.g., fusion and transferring proteins such as flotillin and annexin. The lipid composition is an example of cell-specific constituents of exosomes, as well as integrins and tetraspanins such as CD9 and CD81 (**Fig. 2.10.1**)[100]. Exosomes can both initiate and suppress various signalling pathways in the recipient cells by transporting their heterogeneous cargo.

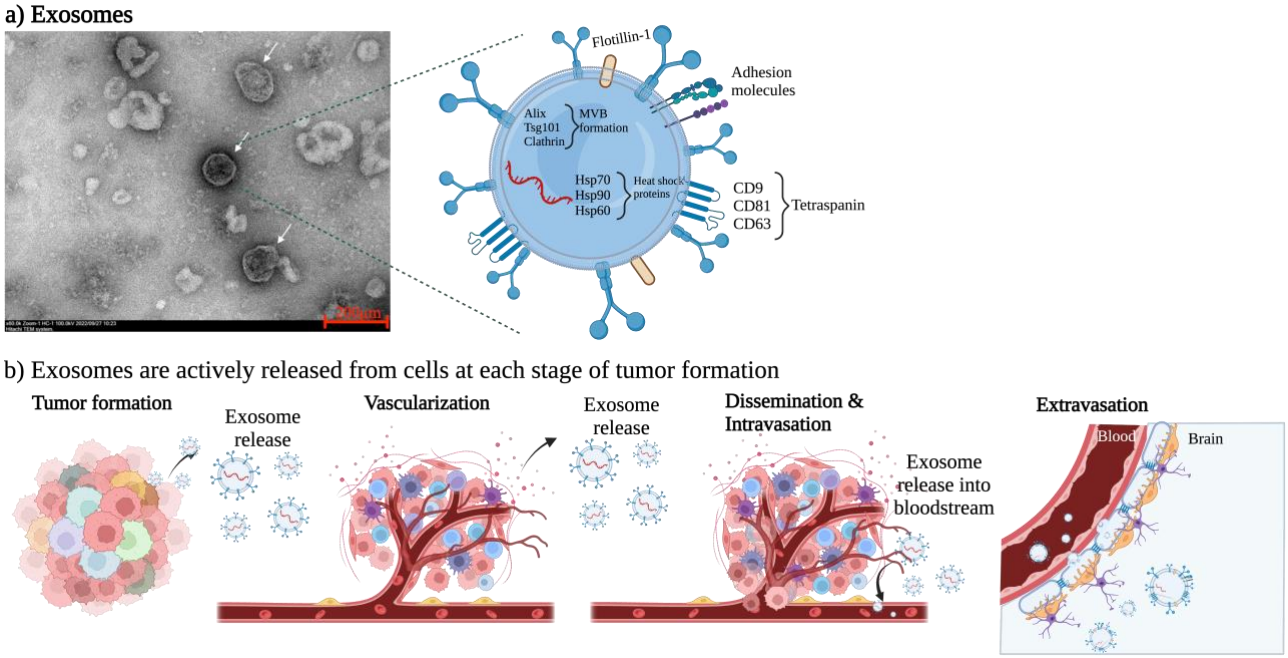

Figure 2.10.1 - Exosomal content and circulation in the bloodstream: *a) Exosomes are easily distinguished when imaged with transmission electron microscopy (TEM) due to their lipid bilayer and cup-shaped morphology (arrows). Their composition varies depending on the cell type of origin and its biological function. Some proteins enclosed within exosomes are cell-type specific, while others, typically transmembrane proteins, are non-specific. b) When released from cells of the primary tumour, exosomes enter the bloodstream and can travel to the brain, where they are able to cross the BBB and enter the brain parenchyma. Here they influence normal brain cells, such as astrocytes, to facilitate the arrival of CTCs. The exact mechanisms of exosomal uptake and transport are not fully understood, but studies bring evidence of a non-random process dependent on the exosomal transmembrane proteins and brain stromal cells. Created with BioRender.com*

2.10.2 Exosomal Biogenesis and Release

Exosomal biogenesis begins with endocytosis, which can occur through clathrin-dependent or clathrin-independent pathways. Endocytosis results in the invagination of various cell-specific receptors and signalling proteins in what is called early endosomes. The endosomal sorting complex required for transport (ESCRT)-dependent pathway and ESCRT-independent pathways facilitate the formation of intraluminal vesicles (ILVs)/exosomes, via

inward budding of late endosomes/MVBs. These ILVs can selectively incorporate cytoplasmic and nuclear molecules, including heat shock proteins, miRNAs, mRNAs, cytoskeletal proteins, transcriptional factors, and DNA. The MVBs are then transported to the plasma membrane via cytoskeletal and microtubule networks, and fuse with the plasma membrane releasing the exosomes into the extracellular space via exocytosis (**Fig. 2.10.2**)[99].

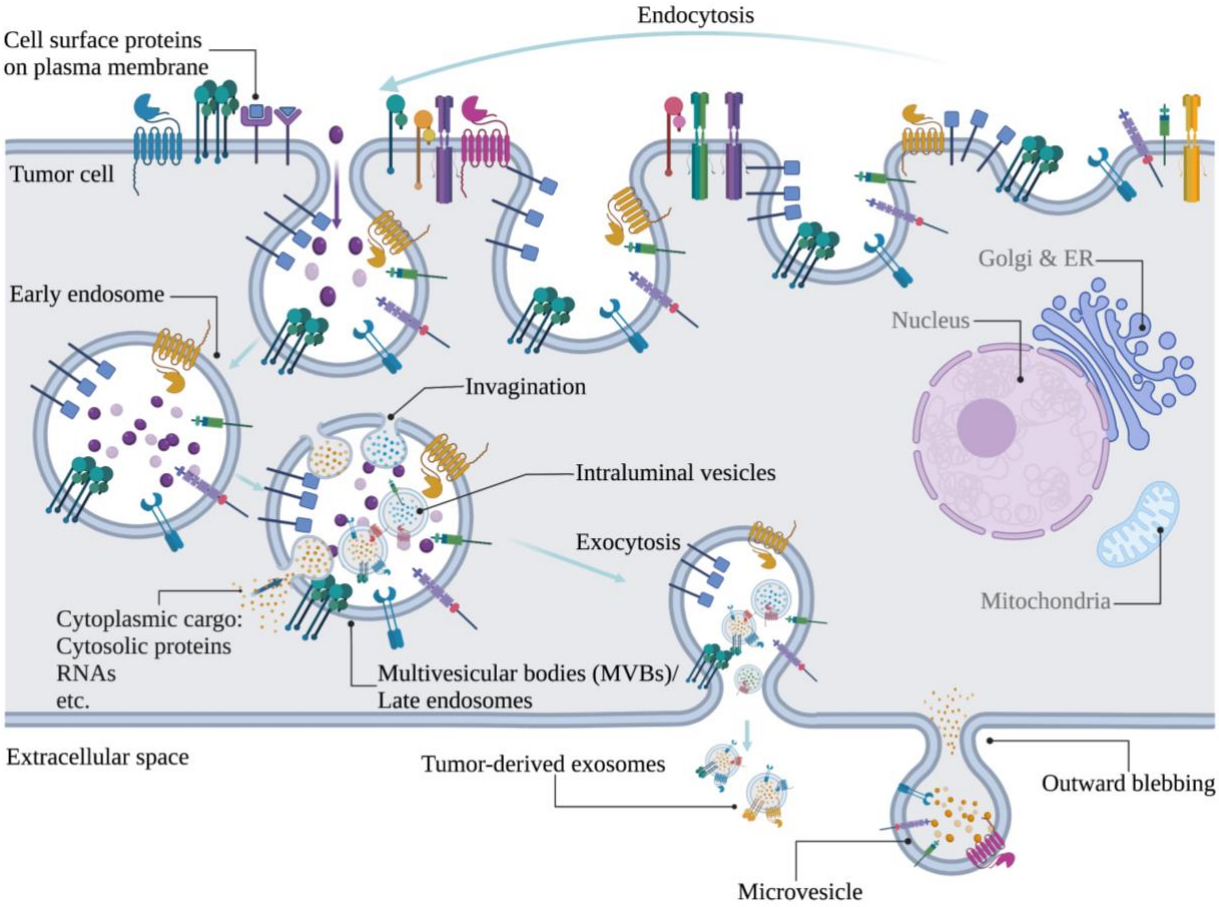

Figure 2.10.2 - EV biogenesis: *Exosomal biogenesis involves a complex series of events, including the formation of early endosomes, the maturation into late endosomes, and the inward budding of MVBs. MVBs are trafficked to the plasma membrane, which they fuse with to release their content, including exosomes, into the extracellular space. Exosomal biogenesis is a highly regulated process that involves numerous proteins and lipids and is vital for maintaining cellular homeostasis and facilitating intercellular communication. Microvesicles are formed by the outward blebbing of the plasma membrane, and so the microvesicle membrane retains the surface proteins of the cell. Created with BioRender.com, with inspiration from [99] and [101].*

Due to their small size, exosomes can traverse the endothelial barrier of the bloodstream. Once they reach a distant organ, they extravasate, and because of their size and unique membrane composition, they can cross biological barriers, including the BBB (**Fig. 2.9**). They are then taken up by recipient cells, releasing their contents into the cellular environment. The bioactive molecules carried by exosomes can exert functional effects on

the recipient cell, ultimately leading to altered conditions favourable for CTCs[102]. Exosomes can trigger these cellular changes by either docking to extracellular receptors and generating a downstream signalling cascade in the recipient cell, or by fusing with the plasma membrane and releasing their content into the cytosol of the recipient cell[97].

2.10.3 Exosomal Function in the TME and Cancer Progression

In addition to the release of growth factors such as vascular endothelial growth factor (VEGF) and TNF from malignant- and immune cells, as well as the induction of hypoxia, recent studies have shown that the transfer of miRNAs in exosomes from cancer cells to ECs facilitates the disintegration of the endothelial barrier. This ultimately promotes the release of cancer cells into the bloodstream[103]. Exosomes derived from cancer-associated fibroblasts (CAFs) found in the TME, and exosomes derived from tumour cells to activate CAFs, positively impact tumourigenesis by sustaining inflammation and producing MMPs that proteolyze ECM components. They also induce a hypoxic environment that stimulates ECs to release proangiogenic factors such as VEGF, which increases the tumour cell supply of oxygen and nutrients[104].

Depending on the cell of origin, exosomes can both suppress and promote the immune system. They have been shown to activate several immune cells, including natural killer (NK) cells, B and T cells, and macrophages. Oncogenic signalling from the activated immune cells can lead to the release of immune-stimulating exosomes that can further trigger a potent anti-tumour response. On the contrary, exosomes can prompt immune suppressive reactions, e.g., inhibition of CD4 and CD8 T helper cell activity, or by inhibiting immune cell differentiation[105].

The intricate and dynamic mechanisms underlying the ability of exosomes to modulate the immune system to accommodate tumour progression are subject to rigorous investigation. Nevertheless, it is clear that exosomes induce a prominent impact and that their cargo has been shown to influence key signalling pathways for tumour progression[105]. Consequently, circulating exosomes from cancer cells can aid in the detection of tumours. They can also be targeted therapeutically to disrupt the transfer of genetic materials and bioactive contents, potentially inhibiting tumour growth and progression once discovered.

Aims:

The main objectives of this master thesis are to generate models of the metastatic microenvironment in the brain and to investigate the development of a model to track exosomes for the detection and treatment of disease microenvironments. To achieve this, several sub-aims were carried out. The first sub-aim was to characterise BM cell lines of various origins and to evaluate their growth characteristics in 2D and 3D environments. The second sub-aim was to isolate exosomes from a human lung and melanoma BM cell lines using differential centrifugation and to load the isolated exosomes with iron-oxide particles through electroporation, to investigate their potential as labelled imaging agents that can aid in the detection and treatment of disease microenvironments. The lung and melanoma BM cell lines were also injected into NOD-SCID mice to evaluate their tumorigenicity and potentially establish models for additional characterization of the cell lines and drug testing.

Overall, this research aims to provide a better understanding of the metastatic microenvironment in the brain to potentially contribute to the ongoing efforts in the development of more effective strategies for the diagnosis and treatment of BM.

3.0 Materials and Methods

3.1 Cell Lines and Cell Culture

Written consent was obtained from the patients before tumour material was collected and subsequently used to prepare cell lines. The Regional Ethical Committee (REC) approved tissue collection, biobank storage of tumour biopsies, as well as development and use of cell lines (REC Approvals 2013/720 and 2020/65185). Cell line authentication was verified by short tandem repeat (STR) fingerprinting, and the cells were regularly tested for mycoplasma.

The LBM1, H16, BrBM1 and BrBM2 cell lines were established in the laboratory of Brain Metastasis Research Lab at the Department of Biomedicine, University of Bergen. The LBM1 cell line was derived from a 61-year-old female patient with BM from lung cancer, specifically non-small cell lung carcinoma (NSCLC), while the H16 cell line was developed from a BM biopsy of a 65-year-old male, melanoma patient. BrBM1 and BrBM2 were developed from BM biopsies (BrBM1; 44-year-old female, BrBM2; 67-year-old female), both with TNBC. All patient biopsies were collected after brain tumour surgery at Haukeland University Hospital.

All cell lines were used for a maximum of ten passages after thawing to minimise genotypic and phenotypic drift and were consistently split at 75-80 % confluency. All cells were stored in Nunc™ EasyFlask cell culture treated flasks with filter caps (Thermo Fisher Scientific, Nunc, Roskilde, Denmark), and LBM1 and H16 were grown in Dulbecco's modified eagle medium (Sigma-Aldrich Inc., St. Louis, MO, USA) supplemented with additives listed in **Table 3.1**, hereafter referred to as culture medium. All cells were kept in the incubator at 37 °C, 100 % humidity and 5 % CO_2, hereafter referred to as standard incubator conditions. BrBM1 and BrBM2 were grown in Advanced DMEM/F-12 (Thermo Fisher Scientific, Waltham, MA, USA) and supplemented with the same additives listed in **Table 3.1**, in addition to insulin (Sigma-Aldrich Inc.) (0,5 μL/mL) in Advanced DMEM/F12 culture medium.

For subculturing, the cells were washed twice with 10 mL 1x PBS prior to trypsinisation using 3 mL 0,25 % Trypsin-EDTA (Thermo Fisher Scientific) in the incubator for 3-5 min. The trypsin was neutralised using 7 mL culture medium and added to 25 mL fresh pre-warmed culture medium before the flask was placed in the incubator for further culturing.

When cell counting was required, 10 µL cell suspension was added to 10 µL of trypan blue dye (Thermo Fisher Scientific), to determine the number of cells per mL and the viability using the Countess Automated Cell Counter (Invitrogen, Toulouse, France).

Table 3.1: Reagents and providers used for cell culturing and handling of cells:

REAGENT	COMPANY/PROVIDER
Advanced DMEM/F12	Thermo Fisher Scientific
DMEM-ALT	
Dulbecco's modified eagle medium	Sigma-Aldrich Inc.
50 ML 10 % Heat-inactivated calf serum	Thermo Fisher Scientific
5 µg/mL Plasmocin	Invitrogen
2 % L-Glutamine	BioWhittaker, Verviers, Belgium
100 IU/mL Penicillin	BioWhittaker
100 µL/mL Streptomycin	BioWhittaker
1x PBS	
10x Dulbecco's phosphate-buffered saline	Sigma-Aldrich Inc.
Autoclaved MilliQ water	Sigma-Aldrich Inc.
0,25 % Trypsin-EDTA	Thermo Fisher Scientific
Trypan Blue Solution, 0.4 %	Thermo Fisher Scientific
Fetal Bovine Serum (FBS)	Thermo Fisher Scientific

3.2 Cryopreservation of Cells

The cryopreservation medium was prepared to prevent cellular damage from ice crystals forming due to the rapid decrease in temperature. 10 mL pre-made cryopreservation medium (sufficient for 10 cryovials) included 8 mL culture medium, 1 mL dimethyl sulfoxide (DMSO) (Sigma-Aldrich Inc.) and 1 mL FBS (Thermo Fisher Scientific). The cells were harvested as described in section 3.1 and transferred to a 15 mL falcon tube (pluriSelect Life Science, Leipzig, Germany). The tube was centrifuged at 800 rpm for 5 min, followed by removal of the culture medium and resuspension of the cell pellet in 10 mL of cryopreservation medium. 1 mL cell suspensions were aliquoted into cryovials (Nunc™ Biobanking and Cell Culture Cryogenic Tubes, Thermo Fisher Scientific), and placed in a isopropanol freezing container (Mr. Frosty™ Freezing Container, Thermo Fisher Scientific) and transferred to -80°. The vials were transferred to a liquid nitrogen storage tank the following day for long-term storage.

3.3 Thawing of Cells

Cryotubes containing the cells were transferred from the liquid nitrogen storage tank, and thawed in a water bath at 37°C. In the biological safety cabinet (BSC) the cells were transferred to 9 mL of pre-warmed culture medium and spun down at 1,200 rpm for 5 min (Jouan B4i, Thermo Fisher Scientific). The medium was removed, the cells resuspended in 1 mL culture medium and transferred to a T25 cm^2 flask (Thermo Fisher Scientific). The flask was then placed in the incubator at standard incubator conditions.

3.4 Lung- and Melanoma BM Cell Lines for Generation of Model Systems

Current model systems of BM have limitations in replicating the unique microenvironment of the brain, which differs significantly from the primary tumour and normal brain tissue. Developing better model systems is essential to understand the biology of BM, identifying new therapeutic targets, and testing the efficacy of treatments. Improved model systems of BM can lead to better outcomes for patients with this challenging disease. To make model systems for *in vivo* BM, patient biopsies were obtained and cultured as described in section 3.1, in order to remove normal brain cells from the cell cultures. The cell lines were then characterised for their genetic and phenotypic properties, such as expression of cancer markers through immunohistochemistry (IHC), their interaction with astrocytes through co-culture analysis, (without further evaluation via sectioning and staining), and their ability to form tumours in mice. *In vitro* models were established by culturing the cell lines in conditions mimicking the *in vivo* microenvironment, using co-culture systems with astrocytes present in the brain microenvironment, and optimising the culture conditions to maintain their cell phenotype. *In vivo* models were established by injecting the BM cell lines into NOD-SCID mice to study the metastatic progression. Finally, the BM cell lines were treated with thioridazine, a BBB-traversing drug to assess its efficacy in reducing the viability of these cancer cell lines, to determine the IC_{50} doses of the BM cell lines, the dose in which 50 % of the cells are still viable after drug treatment.

3.5 Real-Time Cell Proliferation Assay

100 µL of cell suspension of concentrations ranging from 50,000 cells/mL to 400,000 cells/mL were seeded in flat bottom 96-well plates (Nunc™, Thermo Fisher Scientific) and placed in the incubator for 24 h at standard incubator conditions. The following day the plate was transferred to the IncuCyte® Live-Cell analysis system (Sartorius AG, Göttingen, Germany) at standard incubator conditions. Microscopic phase contrast images were taken at 2 h intervals using a 10x objective for 5-7 days. The data was analysed using GraphPad Prism 9 (GraphPad software Inc., La Jolla, CA, USA). Each experiment was performed in triplicate.

To get a numerical comprehension of the growth, the doubling times were calculated using the following equation, where duration equals 72 h and concentration is measured in cells/mL:

$$\text{Doubling time} = \frac{\text{Duration} * \ln(2)}{\ln(\frac{\text{final concentration}}{\text{initial concentration}})}$$

3.6 Cell Morphology

100,000 cells/well were seeded in a 6-well plate (Nunc™, Thermo Fisher Scientific) using the same approach as described in section 3.5. Following 24 h incubation at standard incubator conditions, images were obtained using a Nikon Eclipse brightfield microscope equipped with a Fi3 colour camera (Nikon Corporation, Tokyo, Japan) and NIS-Elements AR software (version 5.30.05) (Nikon Corporation). Between 10-15 images were obtained for each cell line, using the 20x objective. This was done in duplicate.

3.7 Methylcellulose Preparation for Generation of Spheroids

250 mL culture medium was heated to 60 °C and added to a bottle containing 6 g autoclaved methylcellulose (Sigma-Aldrich). The bottle was placed on a magnetic stirrer for 2 h at 500 rpm at 60 °C. Following this, another 250 mL culture medium was added and stirred for an additional 2 h under the same conditions. The bottle was then stirred O/N at 4 °C before the solution was aliquoted into 50 mL falcon tubes (pluriSelect Life Science). The tubes were centrifuged at 5,000 xg for 2 h at RT, and stored at 4 °C until further use.

3.8 Spheroid Formation

Table 3.8: Spheroid plate map:

Concentration:	3,000 cells/well			6,000 cells/well			12,000 cells/well		
% Methylcellulose	0	2	4	0	2	4	0	2	4

LBM1 and H16 cells were harvested and counted as described in section 3.1, and the cell suspensions were added to 15 mL falcon tubes (pluriSelect Life Science). The following calculations were done to determine the volume of cell suspension and culture medium needed for the desired concentrations (**Table 3.8**):

$$\left(\frac{\text{Concentration of cells we want}}{0{,}2\ \text{mL}}\right) \text{x} \left(\frac{1\ \text{mL}}{\text{Concentration of cells we have}}\right) \text{ x total volume needed (mL)} = \text{volume of cell suspension (mL)}$$

$$\text{Total volume} - \text{volume of cell suspension} = \text{volume of culture medium needed}$$

For example:

$$\left(\frac{3{,}000\ \text{cells}}{0{,}2\ \text{mL}}\right) \text{x} \left(\frac{1\ \text{mL}}{2{,}05\ \text{x}\ 10\text{^}6}\right) \text{x}\ 8\ \text{mL} = 0{,}059\ \text{mL}$$

$$8\ \text{mL} - 0{,}059\ \text{mL} = 7{,}941\ \text{mL}$$

These volumes were then added to fresh falcon tubes, and either 0,060 mL or 0,120 mL methylcellulose was added to designated tubes to obtain the final concentrations of 2 % and 4 % methylcellulose (**Table 3.8**). 200 µL cell suspensions were seeded in Corning™ Costar™ Flat Bottom Cell Culture Plates (Thermo Fisher Scientific). The plates were sealed with parafilm and centrifuged at 1,000 rpm for 10 min at 31°C using Heraeus Multifuge 3SR (Thermo Fisher Scientific) before they were placed in the incubator at standard incubator conditions. 24 h later, the plates were placed in the IncuCyte® Live-Cell Analysis System (Sartorius AG) and imaged every 6 h for 7 days using the 10x objective. 100 µL culture medium was replaced every 96 h. The experiments were performed in duplicate.

3.9 Monolayer Viability Assay

Thioridazine is an antipsychotic drug that has been used in the treatment of schizophrenia. Due to its ability to cross an intact BBB, previous preliminary data from our group[58] shows that thioridazine effectively reduces the viability of melanoma BM cells *in vitro*. Through viability assays, the effect of thioridazine on LBM1 and H16 was tested. Thioridazine (Bio Techne, Minneapolis, MN, USA) was received in a powdered form and diluted in DMSO (Thermo Fisher Scientific) to obtain a solution of 50 mM. Aliquots were stored at -20 °C until use, when it was thawed at room temperature (RT) and diluted in culture medium to the desired concentrations of 0,1 μM, 1 μM, 5 μM, 10 μM, (15 μM for LBM1), 20 μM, 50 μM, 75 μM and 100 μM, in addition to one untreated control. The cell lines were seeded in 96-well plates (Nunc™, Thermo Fisher Scientific) at a concentration of 5,000 cells/well and incubated overnight (O/N). Following 24 h incubation, 100 μL of diluted thioridazine was added at the concentrations listed above, each to one column (8 repetitions (wells) per concentration. 100 μL of culture medium was added to two additional columns to serve as a blank for the subsequent readout, and a DMSO control with a concentration of DMSO equivalent to the highest concentration of thioridazine (0,6 %) to verify that growth inhibition was due to the inhibitory effect of the drug and not the toxicity of the DMSO. The cells were then incubated for 72 h at standard incubator conditions. 100 μL was then removed from all the wells, and 10 μL WST-1 (Sigma-Aldrich) was added. The cells were incubated for 3,5 h at standard incubator conditions. The WST-1 assay determined the viability of the cells by measuring the enzymatic cleavage of tetrazolium salts within the culture medium. Cellular enzymes converted these salts into formazan, and an increase in the number of viable cells led to increased activity of mitochondrial dehydrogenases, generating more formazan dye. Triplicates of this study were done to determine the concentration of thioridazine required to inhibit the growth of the cells.

The amount of metabolically active cells was quantified using a multi-well spectrophotometer (Multiskan™ FC Microplate Photometer, Thermo Fisher Scientific), at wavelengths of 420-480 nm, and the average background values were subtracted. An untreated control was used as a reference for 100 % viability, and thioridazine-treated wells were normalized to the control. The normalized values were logarithmically transformed and subjected to a normalized “response-variable slope logistic nonlinear regression analysis” using GraphPad Prism 9 (GraphPad software Inc.). Average IC_{50} values were determined for

both cell lines, establishing a therapeutic window giving safe and effective treatment which would likely yield minimal adverse effects *in vivo*. Three replicates were performed for each cell line to ensure reliability.

3.10 Formalin Fixing and Paraffin Embedding of Cells (FFPE) for IHC

To histologically examine the cell lines used, IHC was done. Prior to this, the cells were fixed, embedded in paraffin, and sectioned. The cells were harvested from confluent T175 flasks and transferred to 15 mL falcon tubes (pluriSelect Life Science). The tubes were centrifuged at 1,200 rpm for 5 min, washed with 1x PBS, centrifuged again under the same conditions, and resuspended in 5 mL 3,7 % formaldehyde for fixation. The tubes were then rotated at 12 rpm for 24 h in RT. The following day they were centrifuged at 400 xg for 10 min to remove the formaldehyde. The cells were washed again in 1x PBS and centrifuged for 5 min at 400 xg. A drop of methyl green (Sigma-Aldrich) was added to each of the pellets and incubated for 2-4 min before 10 mL of 1x PBS was added to each tube. The tubes were centrifuged at 400 xg for 5 min, and 50 μL pre-heated 1,6 % agarose was mixed with the cells. The suspension was transferred to pre-heated 50 mL tubes (pluriSelect Life Science) and centrifuged for 1 min at 400 xg to collect the cells to the bottom before the tubes were placed in the fridge for 30-60 min. Lastly, the cells were transferred to CellSafe™ cassettes (Ted Pella Inc., Redding, CA, USA) placed in 70 % ethanol. The cells were then embedded in wax blocks, which were sectioned into 5 μm thin slices placed on microscope slides. To provide information about the mutational status of the cell lines, the slides were then sent to the Department of Pathology at Haukeland University Hospital, where they performed IHC to identify the presence or absence of specific mutations commonly mutated in the particular cancer types, using the antibodies listed in **Table 3.10**. The sections were then examined under an Olympus VS120 slide scanner (Olympus Scientific Solutions, Waltham, MA, USA) to detect and visualize the presence/absence of the proteins of interest. The quantification of the IHC slides was performed using the Fiji software[106] (version 2.9.0 1.53t).

Table 3.10: Antibodies used in IHC to identify the presence or absence of gene mutations

H16	LBM1	BrBM1 and BrBM2
Melan-A	TTF-1	ER
HMB45	Napsin A	PR
SOX10	CK5/6	CK7
S100	CK7	Her-2
	p63	
	Synaptophysin	
	Chromogranin	

3.11 Intracardial Injections of BM Cell Lines into Mice

The animal experiment was conducted in accordance with the guidelines of the Norwegian Animal Research Authority (FDU) with ethical approval from the Norwegian Food Safety Authority. A total of 10 NOD-SCID mice were used in the study, including two untreated control mice. The mice were housed in a pathogen-free facility at The Laboratory Animal Facility at the Department of Clinical Medicine, and food and water were provided as required.

One melanoma (H16) and one lung cancer (LBM1) cell line were injected into four NOD-SCID mice each. The cells were harvested at ~80 % confluence and counted using an automated cell counter (Countess™, Invitrogen), and adjusted to a concentration of $5x10^6$ cells/mL using 1x PBS. The cells were kept on ice until injection was performed. The mice were anaesthetized with 3 % isoflurane in oxygen and maintained with 1,5 % isoflurane in oxygen during the injection process. The thoracic area of the mice was prepared by removing fur with hair removal cream, and the mice were then placed on a heated board, and the ultrasound probe was fixed onto a holder. The syringe holder containing an insulin needle (U100 0,3 mL BD Micro-Fine+™, Becton Dickinson, Franklin Lakes, NJ, USA) was loaded with 500,000 tumour cells in 100 µL 1x PBS. Warm ultrasound gel was applied to the thoracic area to visualize the left cardiac ventricle on the monitor. Using the ultrasound monitor as a guide, the needle was inserted into the chest and guided into the left cardiac ventricle. A small amount of bright red blood (oxygenated) was drawn into the syringe to confirm the successful piercing of the left ventricle. The BM tumour cells were then slowly injected, and the needle was carefully held in place for a few seconds to prevent backflow, before retracting the needle.

Following injections, the mice were observed daily for signs of illness, such as lethargy, hunched posture, and ruffled fur. The mice were weighed multiple times a week to monitor potential weight loss providing an indication of their overall health. *In vivo* MRI scans were done at weeks 2 and 4, using a Powerscan 7T PET/MR (MR Solutions, Guildford, UK). T2 weighted (T2W) imaging was done using the following scan parameters: Repetition time (TR): 4,000 ms, echo time (TE): 45 ms, slice thickness: 0,5 mm, number of averages: 2, field of view: 20 x 20 mm, acquisition matrix: 256 x 252, flip angle (FA): 90 °. To visualize the total number of tumours and their dimensions, MR images were analysed using the OsiriX Lite v.10.0.0 freeware software (Pixmeo SARL, Geneva, Switzerland). The volumes of the tumours were calculated using the following equation: $V = \frac{4}{3}\pi r^3$.

To ensure compliance with ethical and regulatory standards (Dyrevernloven § 9), the mice were euthanized by CO_2 inhalation and cervical dislocation when loss of 15 % or more of their body weight was observed, or when showing signs of morbidity. Autopsies were performed to visually assess the impact of the *in vivo* injection of the BM cell lines. Following euthanasia, the brains, and other organs, including the heart, lungs, liver, gastrointestinal tract, kidneys, adrenal glands, and spleen, were fixed in a 4 % paraformaldehyde (PFA) solution to preserve the tissues before dehydration in absolute ethanol. This was done to prepare the tissues for histological analyses, which will be performed after the end of this project.

3.12 Exosome-Depleted Culture Medium for Isolation of Exosomes

FBS is used to supplement culture medium to provide nutrients and growth factors. FBS contains EVs which therefore need to be depleted when intended for use in exosome isolation assays. The FBS (Thermo Fisher Scientific) was spun in an ultracentrifuge (L-70 Ultracentrifuge, Beckman Coulter, Brea, CA, USA) at 40,000 rpm for 18 h at 4 °C. Thereafter, the supernatant was transferred to a sterile bottle. The FBS was filtered through a 0,2 μM syringe filter (Sigma-Aldrich) and transferred to 50 mL tubes (pluriSelect Life Science). The FBS was heat-inactivated in a water bath at 56 °C for 30 min to prevent the action of complement components and contamination by mycoplasma. The exosome-free, heat-inactivated FBS was then stored at -20 °C until use. The EV-free medium was made according to **Table 3.12**:

Table 3.12: Composition of complete EV-free culture medium:

REAGENT AND COMPANY	VOLUME
Dulbecco's Modified Eagles Medium (Sigma-Aldrich)	450 mL
EV-free FBS (Thermo Fisher Scientific)	50 mL
L-Glutamine (BioWhittaker)	10 mL
Penicillin/Streptomycin (BioWhittaker)	10 mL
NEAA 100X Non-Essential Amino Acids (Lonza, Basel, Switzerland)	16 mL
Plasmocin (Invitrogen)	100 µL

3.13 Extraction of Exosomes Through Differential Centrifugation

The cells were cultured in 25-30 mL EV-free culture medium for 48-72 h (~90 % confluent). The culture medium was collected, hereafter referred to as conditioned culture medium, and the cells were washed with 1x PBS and harvested as described in section 3.1. 10 µL cell suspension was mixed with an equal volume of trypan blue (Thermo Fisher Scientific) for counting using the Countess Automated Cell Counter (Invitrogen). 10 mL of the cell suspension was centrifuged at 1,200 rpm for 5 min (Jouan B4i, Thermo Fisher Scientific). The cell pellet was resuspended in 10 mL 1x PBS centrifuged at 1,200 rpm for 5 min and stored at -80 °C to be used for subsequent Western blotting.

The conditioned culture medium was centrifuged at 1,200 rpm for 5 min (Jouan B4i, Thermo Fisher Scientific) to pellet down cells and cellular debris (**Fig. 3.13**). The supernatants were centrifuged again at 2,000xg for 20 min (Eppendorf® Centrifuge 5810/5810R, Hamburg, Germany) to remove apoptotic bodies. The conditioned culture medium was transferred to ultracentrifuge sealing tubes (Beckman Coulter) using a syringe and topped off with filtered 1x PBS. The tubes were sealed using Tube Topper (Beckman Coulter) to prevent leakage during the spinning. They were then ultracentrifuged for 25 min at 15,000 rpm using an L-70 Ultracentrifuge equipped with a Ti70 rotor (Beckman Coulter) to remove microvesicles (**Fig. 3.13**). Following this, the supernatants were transferred to new ultracentrifuge tubes and ultracentrifuged at 40,000 rpm for 2 h to spin down the exosomes (**Fig. 3.13**). Once completed, the supernatants were discarded, and 500 µL filtered 1x PBS was added. The exosome pellets were resuspended and transferred to a single 5 mL open-top ultracentrifuge tube. To ensure complete transfer of the pellet, an additional 500 µL of filtered 1x PBS was added to one of the tubes and then sequentially transferred to the other tubes. These tubes were ultracentrifuged at 100,000 xg in the Optima MAX-XP tabletop ultracentrifuge (Backman Coulter) for 1 h using the MLS50 swinging-bucket rotor (Backman Coulter) to

rinse the exosomes and eliminate free protein remnants (**Fig. 3.13**). All spins were performed at 4 °C. Finally, the pellet was resuspended in 100 µL filtered 1x PBS and stored at -80 °C until use.

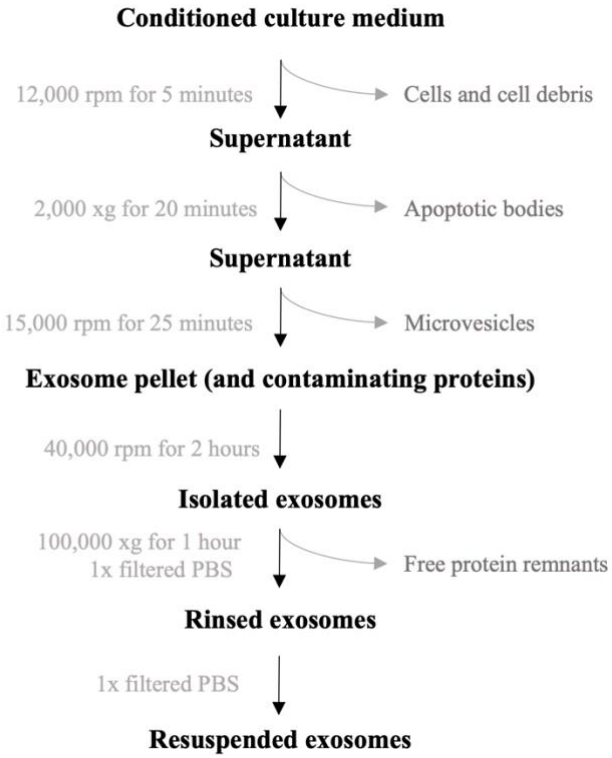

Figure 3.13: Protocol for differential centrifugation to isolate exosomes from conditioned culture medium: *The scheme delineates the workflow for the isolation of exosomes from conditioned culture medium harvested from cells grown in EV-free culture medium for 48-72 h. The exosomal isolation begins with three low-speed centrifugations to contract cells, cellular debris, apoptotic bodies and microvesicles. Ultimately, the exosomes are isolated and washed with 1x PBS by ultracentrifugation to remove free protein remnants and are stored until use. Revolutions per min (rpm), Relative centrifugal force (xg).*

3.14 SDS-PAGE and Western Blots for Detection of Exosomal Markers

Table 3.14.1: Regents and providers used for SDS-PAGE and Western Blots:

REAGENTS		COMPANY/PROVIDER
Lysis buffer:		
RIPA buffer	900 µL	Thermo Fisher Scientific
10x protease and phosphatase inhibitors	100 µL	Thermo Fisher Scientific
Running buffer:	50 mL 20x MOPS	NuPAGE™, Invitrogen
	950 mL deionized water	-
Transfer buffer:	50 mL 20x transfer buffer	NuPAGE™, Invitrogen
	100 mL Antioxidant	NuPAGE™, Invitrogen
	850 mL deionized water	-
TBS-Tween:	100 mL TRIS-buffered saline	Invitrogen
	1 mL Tween	Invitrogen
	900 mL deionized water	-
Blocking buffer:	50 ml TBS-Tween	-
	2,5g Skim milk	Sigma-Aldrich
4x LDS sample buffer		NuPAGE™, Invitrogen
10x Sample Reducing Agent		NuPAGE™, Invitrogen
SeeBlue™ Plus2 Pre-stained Protein Standard		Invitrogen
Ponceau staining solution		Thermo Fisher Scientific
SuperSignal West Pico Chemiluminescent Substrate		Thermo Fisher Scientific
Antibody diluent reagent solution		Life Technologies™, Carlsbad, CA, USA

To prepare the isolated exosomes and cells prepared in section 3.13, 5 µL of 4x lithium dodecyl sulfate (LDS) sample buffer, along with 2 µL of 10x reducing agent was added to each sample in Eppendorf tubes (**Table 3.14.2**). The cells and exosomes were lysed on ice for 30 min using 200 µL lysis buffer, vortexing every 10 min. The lysates were centrifuged at 12,000 rpm (Eppendorf™ 5424R Microcentrifuge, Thermo Fisher Scientific) at 4 °C for 10 min, and the supernatants were transferred to new tubes. The protein content of the samples was measured using Direct Detect® Spectrometer (Merck Millipore, Burlington, MA, USA), to determine the concentration of the lysates and volume of Milli-Q® water (Sigma-Aldrich) needed for a total loading volume of 20 µL (example shown in **Table 3.14.2**).

Table 3.14.2 – Constituents mixed to prepare samples for SDS-PAGE and Western blot:

Sample	Concentration (μg/μL)	μg Protein	4x LDS (μL)	10x reducing agent (μL)	Vol. water (μL)	Total loading vol. (μL)
LBM1 cells	4,68	4,3	5	2	8,7	20 μL
LBM1 exosomes	3,38	5,9	5	2	7,1	20 μL
H16 cells	6,69	3,0	5	2	1,0	20 μL
H16 exosomes	5,21	3,8	5	2	9,2	20 μL

Once all components were mixed, the tubes were placed in a heating block (Thermomixer R, Eppendorf, Hamburg, Germany) at 70 °C for 10 min allowing the sodium dodecyl sulfate (SDS) in the running buffer to bind in the hydrophobic regions and denature the proteins to enable the migration from the negative to positive anode. The samples were then vortexed and centrifuged (Ministar Silverline, VWR, Radnor, PA, USA) to mix the evaporated water back into the suspension.

The Minimal Information for Studies of Extracellular Vesicles (MISEV) proposed by The International Society for Extracellular Vesicles (ISEV) in 2018, strongly recommends the use of at least three positive protein markers typically seen in EVs, including at least one transmembrane/lipid-bound protein, one cytosolic protein and lastly minimum one negative protein marker typically seen in cells[107]. The protein markers used therefore include Calnexin ((C5C9) Rabbit mAb #2679), a 90kDa integral protein of the endoplasmic reticulum (ER). It is cell-specific and therefore serves as a negative marker for exosomes due to its ER location. The exosome surface protein markers include Flotillin-1 ((D2V7J) XP® Rabbit mAb #18634,), a 49 kDa protein involved in endocytosis and other cellular trafficking steps, Tsg101 ((E6V1X) Rabbit mAb #72312), a 44kDa positive intracellular marker, and lastly transmembrane markers from the tetraspanins family of proteins, CD9 (24-27 kDa, (D8O1A) Rabbit mAb #13174)) and CD81 (26 kDa, (D3N2D) Rabbit mAb #56039)). All markers were purchased from Cell Signaling Technologies (Danvers, MA, USA) and diluted 1:1,000 prior to use.

8μL of the SeeBlue™ Plus2 protein standard (Invitrogen) was loaded in the first lane of the gel, a 1 mm 12-well 4-12 % Bis-Tris gel (Invitrogen). 20μL of the samples were loaded in adjacent lanes. The chamber (Mini Gel Tank, Thermo Fisher Scientific) filled with running buffer (**Table 3.14.1**) was placed in a box of ice to run the gel under cooling conditions at 200V for 50 min. Once done, the gel was submerged in transfer buffer (**Table 3.14.1**) while

preparing for the protein transfer. The transfer was done using the XCell SureLock™ Mini-Cell Electrophoresis System (Invitrogen), where filter paper, a nitrocellulose membrane, and sponges were pre-soaked in transfer buffer. To prevent resistance to the electric current in the system, the transfer was done on ice to maintain a low temperature while running at 30V for 90 min. Following this, the membranes were incubated in Ponceau staining solution (Thermo Fisher Scientific) for 2-5 min, followed by washing with Milli-Q® water (Sigma-Aldrich). The membrane was then cut using the bands of the protein standard to estimate the position of the marker proteins. The membrane sections were blocked with blocking buffer for 1 h at RT. They were washed twice with TBS-Tween for 5 sec, before incubation with primary antibodies diluted in blocking buffer, O/N at 4°C on a SSL4 Rocker (Antylia Scientific, Vernon Hills, IL, USA).

The following day, the membrane sections were washed with TBS-Tween as follows: 2x 5 sec, 1x 15 min and 2x 5min. 2 mL of secondary antibodies (Cell Signaling Technology) diluted in blocking buffer was added to the membranes for 1 h at RT on an SSL4 Rocker (Antylia Scientific). The membranes were then washed as follows: 2x 5 sec, 1x 15 min and 4x 5 min.

The protein markers were visualized using Luminescent Image Analyser LAS-3000 (Fujifilm Life Science, Cambridge, MA, USA). SuperSignal West Pico Chemiluminescent Substrate (Thermo Fisher Scientific) was used to amplify the bands of the markers. 100-200 μL of the substrate was added to the membrane sections for the luminol in the chemiluminescent substrate to react with the horseradish peroxidase (HRP) enzyme conjugated to the secondary antibody. In the presence of HRP, the luminol reacts with hydrogen peroxide in the substrate, which emits light that can be detected by the luminescent image analyser.

3.15 Analysis of Exosome Size Distribution Using Dynamic light scattering (DLS)

DLS is a technique used to determine the size distribution profile of small particles in suspension, by measuring the Brownian motion of the molecules and establishing a correlation between this motion and the size of the particles. The Zetasizer Nano ZS (Malvern Panalytical, Malvern, UK) was used to analyse the size distribution of the exosome populations isolated as described in section 3.13. The samples were prepared to 5x, 10x and

50x dilutions (i.e., 10 μL exosome sample in 40 μL filtered 1x PBS). 40 μL was loaded into a clean, dust-free cuvette, and placed in the Zetasizer Nano instrument for analysis.

3.16 Fixation of Exosomes for TEM

To fix the exosomes for TEM, Karnovsky's fixative was prepared to a final volume of 1 mL 6-72 h before mounting for TEM (**Table 3.16**):

Table 3.16: Karnovsky's fixative:

REAGENT	COMPANY/PROVIDER
500uL 0,2M Na Cacodylate Buffer	
0,2 M Dimehylarsinic acid sodium salt trihylate	Sigma-Aldrich
0,2 M Sucrose	Sigma-Aldrich
0,005 M Calciumchlorid-dihydrate	Sigma-Aldrich
50uL 50 % Glutaraldehyde	Electron Microscopy Sciences (Hatfield, PA, USA)
200uL 10 % PFA	Sigma-Aldrich
250uL MilliQ H_2O	Sigma-Aldrich

3.17 Negative Staining of Exosomes for TEM

Exosomes resuspended in filtered 1x PBS were added to Karnovsky's Fixative to make the following dilutions: 1:2, 1:5 and 1:10. Two drops of uranyl acetate (~20-30 μL) were placed adjacently on parafilm. 5 μL of the samples were placed onto formvar carbon-coated grids for 1 min. The grids were held onto the first drop of uranyl acetate using tweezers, and the excess was absorbed by filter paper. This was repeated for the second drop, but for 30 seconds. The grids were then airdried and stored in a grid box until use.

3.18 Exosome Image Acquisition by TEM

Images of the exosomes were obtained using an HT7800 RuliTEM instrument (Hitachi, Tokyo, Japan), a 120 kV TEM with an Emsis Xarosa bottom-mounted CMOS camera (Emsis, Muenster, Germany), at a voltage of 100 kV. The copper grids coated by formvar carbon film were mounted on the MS2 holder and carefully inserted into the TEM for image acquisition. Their cup-shaped morphology and unimodal size distribution were examined to distinguish them from other contaminating extracellular vesicles, as they do not display a central depression, which is characteristic of exosomes under TEM. This was done in triplicate to ensure reliability and validity.

3.19 Loading Exosomes with SPIONs by Electroporation

Table 3.19: Parameters used for electroporation of exosomes: *kV = kilovolts, uF = microfarad*

Condition	Amount of Exosomes	Buffer	Voltage (kV)	Capacitance (uF)	Resistance	Pulse(s)
1	50ug	50mM trehalose	0,300	950	none	1
2	50ug	50mM trehalose	0,300	950	none	2
3	50ug	400mM sucrose	0,950	50	none	1
4	50ug	400mM sucrose	0,950	50	none	2
Passive control	50ug	1x PBS	-	-	-	-
Untreated control	50ug	1x PBS	-	-	-	-

The isolated exosomes were electroporated using the conditions listed in **Table 3.19** to incorporate carboxyl-coated SPIONs of 5 nm (Ocean Nanotech, San Diego, CA, USA) into the exosomes. The trehalose and sucrose buffers were diluted in 1x PBS to the desired concentrations of 50 mM and 400 mM, respectively. The resistance and capacitance values control the time constant, also referred to as the pulse length. It determines how fast the voltage decreases to one-third of its original value. The passive control was not subjected to any pulses, as this sample contained the exosomes and SPIONs incubated for 30 min on ice. The untreated control was neither electroporated nor incubated with SPIONs.

Batches of 50 μg of exosomes were added to Eppendorf tubes labelled with the respective condition (**Table 3.19**), and 2,5 ug/mL of the SPIONs was added to the samples. The tubes were incubated on ice for 30 min, mixing every 10 min. The tubes were topped up to 750 μL with their respective buffers (**Table 3.19**) before they were transferred to electroporation cuvettes equipped with aluminium electrode plates on either side with a gap width of 0,4 cm (Bio-Rad, Hercules, CA, USA). The samples were electroporated using the Gene Pulser II Electroporator (Bio-Rad) according to the conditions listed in **Table 3.19**. The pulse(s) induces a transmembrane potential that results in the formation of transient pores through which the iron oxide particles may penetrate into the exosomes. Thereafter, they were placed on ice for 30 min to retain the SPIONs within the exosomes. Following this, the exosomes were washed with 1x PBS by ultracentrifuging at 100,000 xg for 1 h using the Optima MAX-

XP tabletop ultracentrifuge (Beckman Coulter) with an ML-50 rotor to remove SPIONs that were not internalised into the exosomes. The pellets were resuspended in 25 μL 1x PBS before mixing 1:1 with Karnovsky's fixative to prepare for negative staining and TEM following the protocols described in sections 3.16 and 3.17.

3.20 Prussian Blue Staining for Detection of Ferric Ions (Fe3+)

Prussian blue was used to detect intracellular carboxyl-coated SPIONs (Ocean Nanotech) within LBM1 cells. The reaction of ferric ion (Fe^{+3}) present in the cells combined with the ferrocyanide results in the formation of a bright blue pigment called Prussian blue, or ferric ferrocyanide.

The cells were seeded in a 24-well plate (Nunc™, Thermo Fisher) with a concentration of 100,000 cells per well. The following day, increasing concentrations of carboxyl-coated SPIONs (Ocean Nanotech) ranging from 10 μg/mL to 30 μg/mL were added to the culture medium. The cells were left in the incubator for another 48 h before the culture medium was removed, and the cells were washed three times with 1x PBS. The cells were then fixed in 3,7 % PFA (in 1x PBS) at RT and washed 3x 5 min with 1x PBS. After 20 min, the cells were washed in distilled H_2O (dH_2O) and rinsed with 70 % EtOH for 2 min. Thereafter, they were washed 2 times with dH_2O and stained with the diluted potassium ferrocyanide solution ($K_4[Fe(CN)6] \times 3H_2O$) for 20 min in RT. Lastly, the plate was rinsed 2-3x with dH_2O. The plate was imaged using the Nikon Eclipse microscope (Nikon Corporation).

30 nm Dextran-coated SPIONs (BioPal Inc., Worcester, MA, USA) were also incubated with the LBM1 cells, to assess the internalization in comparison to the carboxyl-coated SPIONs (Ocean Nanotech). Increasing concentrations ranging from 2,5-30 μg/mL were added to the culture medium and incubated for 24 and 48 h followed by staining with Prussian blue as described above.

4.0 Results:

4.1 Growth Characteristics of LBM1 Cells

To assess the growth rate of LBM1, the IncuCyte Live imaging system was utilised to monitor and capture real-time images of the cells ranging from concentrations of 50,000 to 400,000 cells/mL throughout the incubation period. Cells seeded at concentrations above 100,000 cells/mL reached confluency within 36 h. Subsequent viability experiments were performed over 72 h, proving that these concentrations were too high (**Fig. 4.1 a**). Thus, lower cell concentrations were tested. The cell cultures reached 100 % confluency at around 100 h when seeded at a density of 50,000 cells/mL, and after around 60 h when seeded at 100,000 cells/mL (**Fig. 4.1 b**). Therefore, a seeding density of 50,000 cells/mL was used for subsequent and future experiments, as several assays, including viability, proliferation and toxicity, are commonly performed over 72 h. The cell growth doubling time was around 28 h.

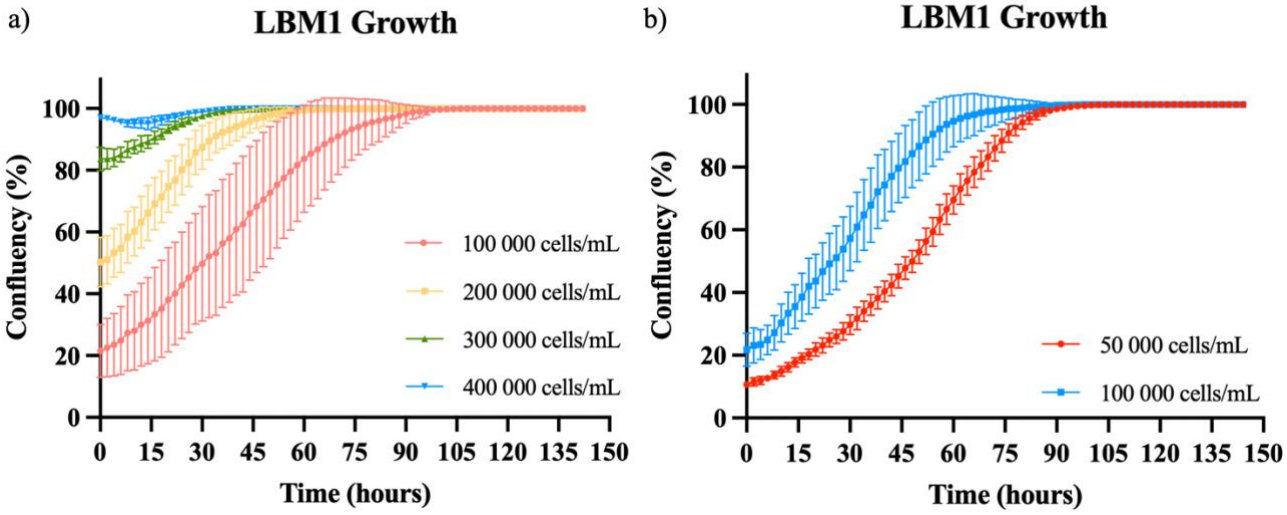

Figure 4.1 - Growth of LBM1 cells over a 6-day incubation period: *a) Cells of the LBM1 cell line seeded at concentrations ranging from 100,000 – 400,00 cells/mL. b) Cells of the LBM1 cell line seeded at concentrations 50,000 and 100,000 cells/mL. The error bars indicate the standard deviation (SD).*

4.2 Growth Characteristics of H16 Cells

H16 cells exhibited a slower growth rate compared to LBM1 cells. As seen in **Fig. 4.2 a**, the initial cell seeding densities of 300,000 and 400,000 cells/mL were too high, as the cells reached 100 % confluency at the beginning of the experiment. In contrast, the densities of 100,000 and 200,000 cells/mL allowed the cells to grow and expand for a longer duration before reaching full confluency around day 6. For subsequent experiments, 200,000 cells/mL were used, as they reached full confluency within 72-100 h (**Fig 4.2 b**). The cell growth

doubling time was 47 h. In contrast to LBM1, some H16 cell cultures exhibited a deceleration in their growth rate after exceeding passage number 29, indicating an alteration in the cellular physiology affecting the growth characteristics. It is therefore required to take caution when performing cell culture experiments using H16 cells past passage number 29.

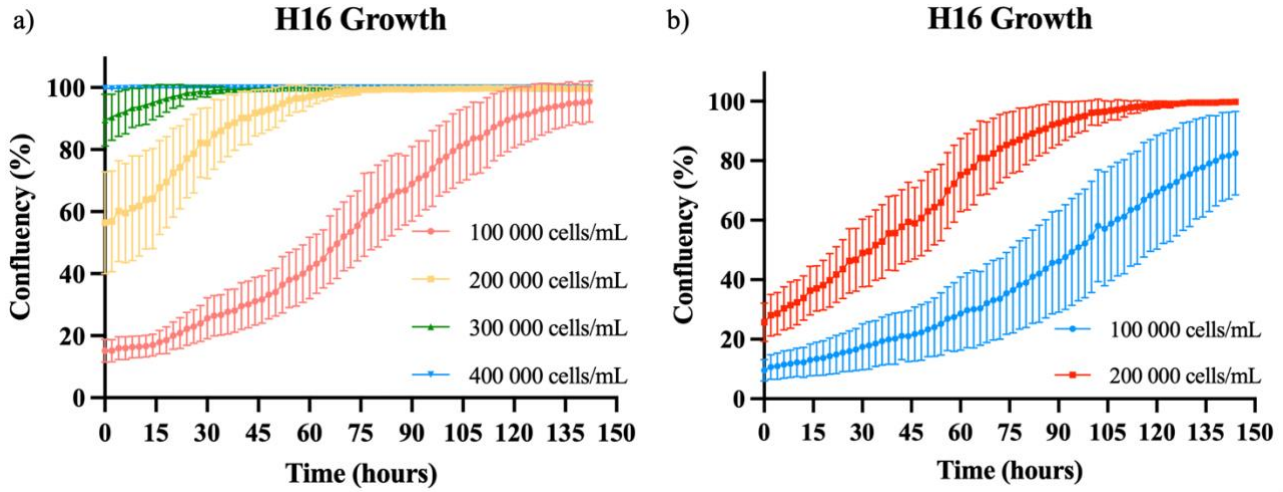

Figure 4.2 - Growth of H16 cells over a 6-day incubation period: *a) Cells of the H16 cell line seeded at concentrations ranging from 100,000 – 400,00 cells/mL. b) Cells of the H16 cell line seeded at concentrations of 100,000 and 200,000 cells/mL. Error bars indicate SD.*

4.3 Growth Characteristics of BrBM1 and BrBM2 Cells

BrBM1 and BrBM2 cells showed limited growth, as evidenced by the growth curves in **Fig. 4.3 a-b**. Concentrations ranging from 10,000 to 150,000 cells/mL exhibited restricted growth beyond that observed on day 1, despite being cultured for a period of 6 days and changes in culture medium every 96 h. Due to their limited growth potential, these cell lines were not used for further viability experiments.

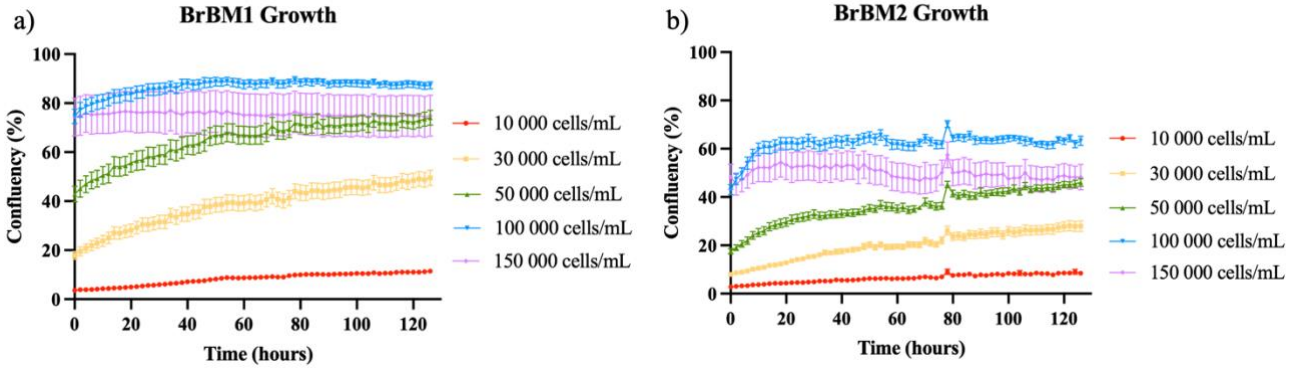

Figure 4.3 - Growth of BrBM1 and BrBM2 cells over a 6-day incubation period: *a) Cells of the BrBM1 cell line seeded at concentrations ranging from 10,000 – 150,00 cells/mL. b) Cells of the BrBM2 cell line seeded at concentrations of 10,000 and 150,000 cells/mL. Error bars indicate SD.*

Due to their slow growth in monolayers, the ability of these cell lines to form three-dimensional spheroids was not studied, as it is to be expected that the intrinsic growth properties of the cells seen in 2D monolayers will remain similar in 3D cultures.

4.4 Morphological Characteristics of LBM1, H16, BrBM1 and BrBM2 Cells

LBM1 cells exhibited characteristic morphologies resembling those of epithelial cells (**Fig. 4.4 a**), with short and few filopodia and a rounded shape as opposed to elongated cells such as e.g., neurons and fibroblasts. However, some pleomorphism was observed, which is the variability in the shape and size within the cell population, with the shape of the cells ranging from rounded to polygonal, reminiscent of epithelial cells. The cells appeared non-polarized due to the centrally located nucleus. The nucleus was round, with abundant cytoplasm. The cells displayed a compact appearance in confluent cultures and a high degree of cellular adhesion to each other.

As seen in **Fig. 4.4 b**, the H16 cells displayed a more homogenous spherical morphology compared to LBM1 cells, and limited cell-cell adhesion was observed in the cultures. They had little to no filopodia and appeared non-polarized like LBM1 cells. The nucleus-to-cytoplasm ratio was increased in comparison to LBM1 cells. H16 cells expressed some degree of pleomorphism, as a small proportion of the cells displayed a more elongated morphology resembling that of LBM1 cells, but the vast majority were rounded with distinct cell borders.

The BrBM1 and BrBM2 cell lines were characterised by a distinctly irregular and disorganized morphology with asymmetrical boundaries. They also exhibited pleomorphism. The extensive cellular protrusions and stellate morphology were significantly more prominent in comparison to LBM1 and H16 cells. **Fig. 4.4 c-d** shows that the BrBM1 and BrBM2 cell lines exhibited a more flattened morphology compared to LBM1 and H16 cells, resulting in poorly defined cell borders. They were distinguished by their elongated cell bodies and invasive projections, establishing connections across cell colonies.

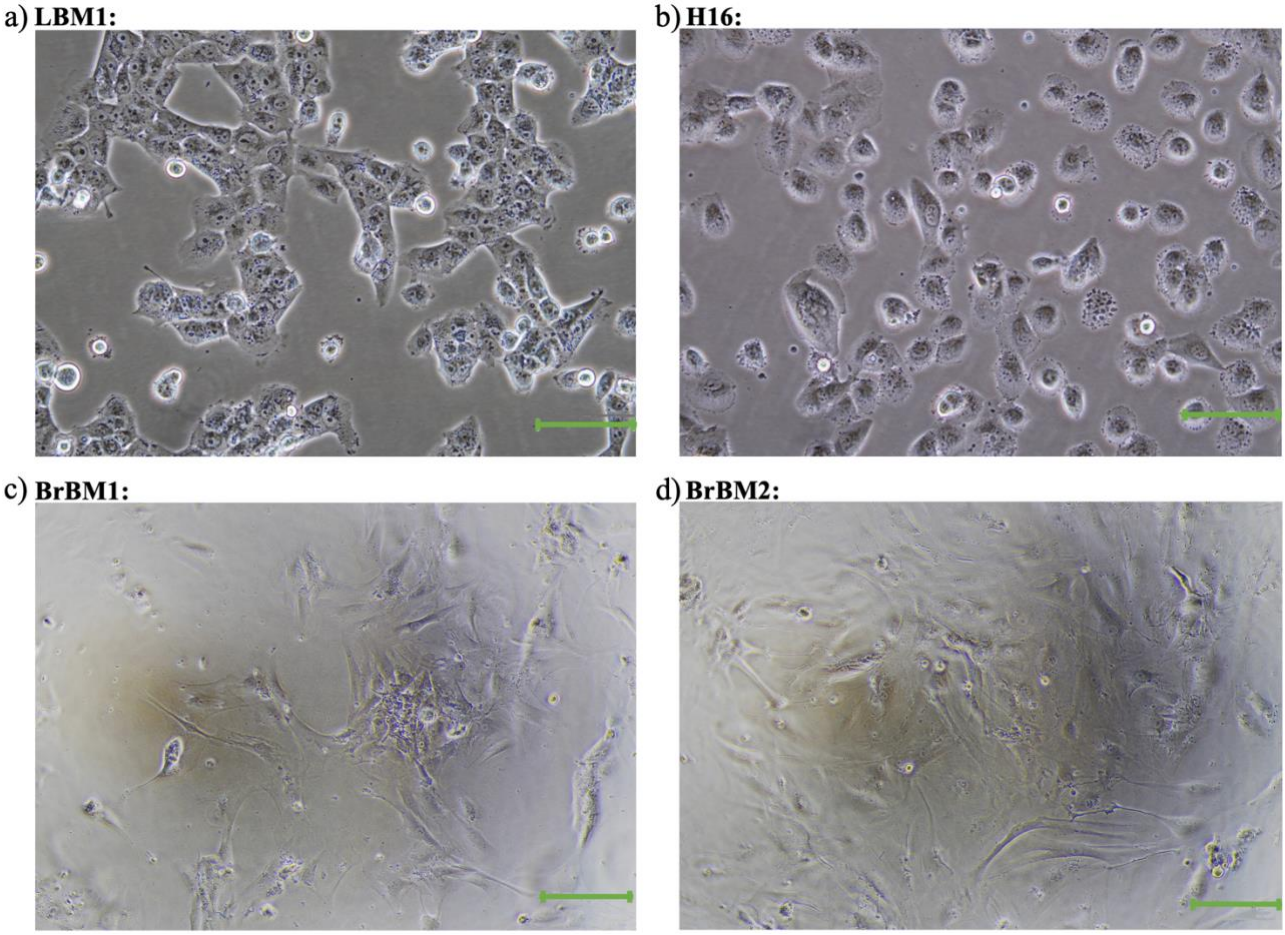

Figure 4.4 – Cellular morphology of BM cell lines: *The morphological appearance of metastasizing tumour cells of different origins, including, a) lung (LBM1), b) skin (H16), and c-d) breast (BrBM1 and BrBM2), displayed distinct cellular features due to their contrasting genetic and epigenetic backgrounds. All images were taken with a 20x objective, and all scale bars equal 100 um.*

4.5 LBM1 Cells are Able to Form Three-Dimensional Spheroids

To assess the ability of LBM1 cells to form three-dimensional spheroids and to study how they interact with each other in a more physiologically relevant model system, the cells were seeded with increasing concentrations ranging from 3,000 to 12,000 cells/well, and with different concentrations of methylcellulose to aid in the formation of stable and compact spheroids. The cells successfully formed multicellular aggregates within three days of incubation, with varying sizes depending on the initial seeding density (**Fig. 4.5 a-b**). The spheroids that were seeded as 12,000 cells/well displayed the most rapid initial growth (**Fig. 4.5 a**) and size expansion (**Fig. 4.5 c-d**) compared to 3,000 and 6,000 cells/well. During the initial phase, the spheroid size increased with increasing cell seeding density, proving a positive linear correlation between the spheroid size and cell seeding density. The maximum area over the 7-day incubation for spheroids seeded with 3,000 cells/well was 1,36 $x10^6$ μm^2,

1,23 x10^6 μm^2 for those seeded with 6,000 cells/well, and 1,15 x10^6 μm^2 for those seeded as 12,000 cells/well. As depicted in **Fig. 4.5 a**, the spheroids seeded as 6,000 and 12,000 cells/well reached a maximum size on days 6 and 3, respectively, whereas spheroids seeded with 3,000 cells/well were still exponentially growing on day 7.

Spheroids are complex three-dimensional structures that cannot be fully characterised by a growth curve alone. Images of the spheroids on each day in **Fig. 4.5 d** provide a visual representation of their size, shape, and organisation, supporting the conclusions made based on the growth curves in **Fig. 4.5 a-c**. LBM1 is a rapidly growing cell line, so these findings were consistent with previous experiments using LBM1 cells.

As seen in **Fig. 4.5 b**, there was no significant difference between the spheroids grown in the presence of methylcellulose and those grown in the absence of methylcellulose. This suggests that LBM1 cells effectively formed spheroids without the need for the additional support provided by methylcellulose. The diameter of the spheroids formed by LBM1 cells significantly increased between day 3 and day 7 (**Fig. 4.5 c**) for those seeded as 3,000 and 6,000 cells/well. In contrast, the spheroids seeded as 12,000 cells/well decreased in size from day 3 to day 7. 3,000 cells/well without the addition of methylcellulose will therefore be used for future experiments using LBM1 cells.

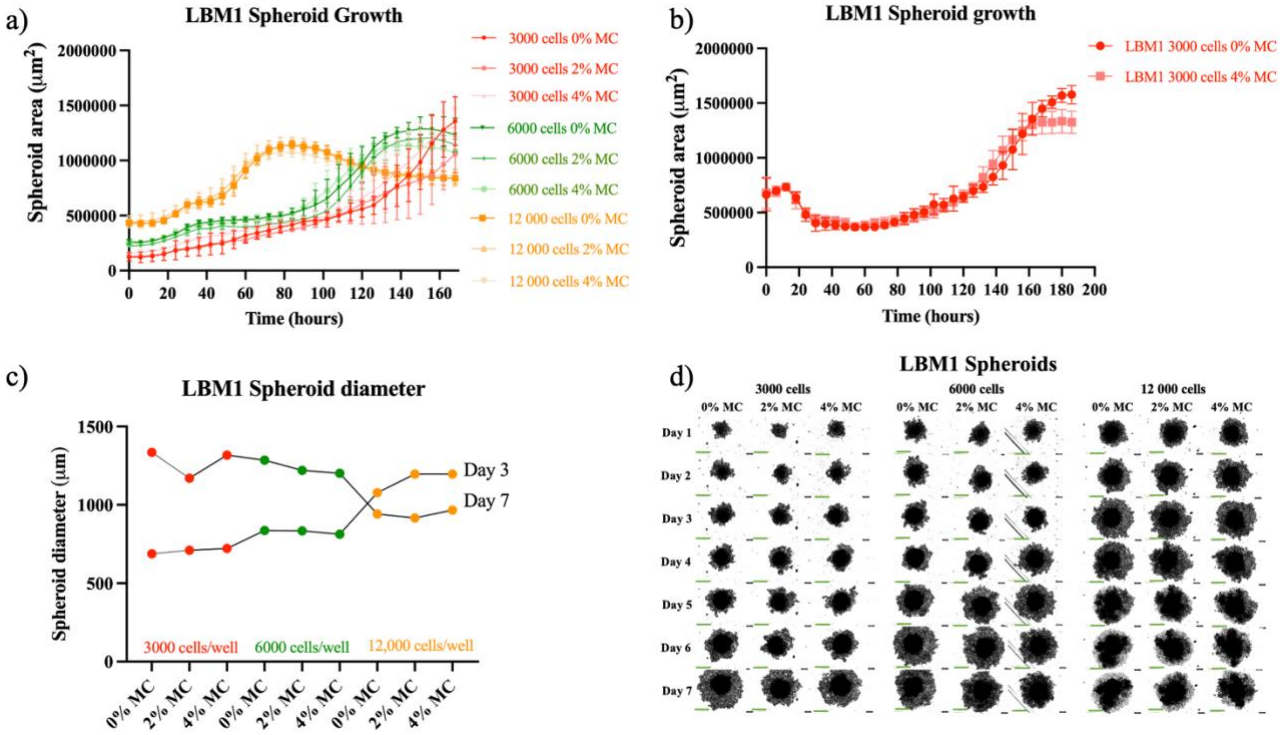

Figure 4.5 – Growth of spheroids formed with LBM1 cells: *a) Growth curve of spheroids composed of LBM1 cells, grown with varying concentrations of cells and methylcellulose. Their area (measured in µm²) was tracked over 7 days. b) 7-day growth of spheroids seeded as 3,000 cells/mL, with 0 % and 4 % methylcellulose. c) Comparison of the spheroid diameter at day 3 and day 7, measured in µm. d) Microscopic images of each spheroid throughout the 7-day incubation period. All scalebars are 400 µm. MC = methylcellulose.*

4.6 H16 Cells are Able to Form Three-Dimensional Spheroids

H16 cells were seeded to examine their ability to form multicellular spheroids, both with and without the addition of methylcellulose. H16 cells generated well-formed structures which were uniform in shape and size. As seen in **Fig. 4.6 a** and **c**, the spheroids seeded as 12,000 cells/well entered a plateau phase where the growth of the spheroids slowed down significantly. Spheroids seeded at a density of 6,000 cells per well exhibited initial growth rates similar to those seeded at a density of 3,000 cells per well. However, by day 7, the growth of the former reached a plateau phase (**Fig. 4.6 a**), in contrast to those seeded as 3,000 cells/well.

Furthermore, the spheroids seeded as 12,000 cells/well displayed the most rapid initial growth (**Fig. 4.6 a**) and size expansion (**Fig. 4.6 c-d**) compared to 3,000 and 6,000 cells/well. During the initial phase, the spheroid area increased correspondingly with increasing cell number, providing a positive linear correlation between the spheroid size and cell seeding

density, as seen with LBM1-derived spheroids. The maximum size area for spheroids seeded with 3,000 cells/well was 1,26 x10^6 µm^2, 1,61 x10^6 µm^2 for those seeded with 6,000 cells/well, and 1,58 x10^6 µm^2 for those seeded as 12,000 cells/well. As depicted in **Fig. 4.6 a**, the spheroids seeded with 6,000 and 12,000 cells/well reached a maximum size limit on day 7, whereas spheroids seeded with 3,000 cells/well were still exponentially growing on this day.

3,000 cells/well was the selected seeding density for subsequent experiments, given their sustained growth by day 7 and well-organized morphology (**Fig. 4.6 d**). Similarly, to LBM1, spheroids were effectively formed by H16 cells, without requiring the additional support provided by methylcellulose (**Fig. 4.6 b**). **Fig. 4.6 d** provides crucial visual information that correlates to the growth curves and enhances the understanding of their progression from day to day.

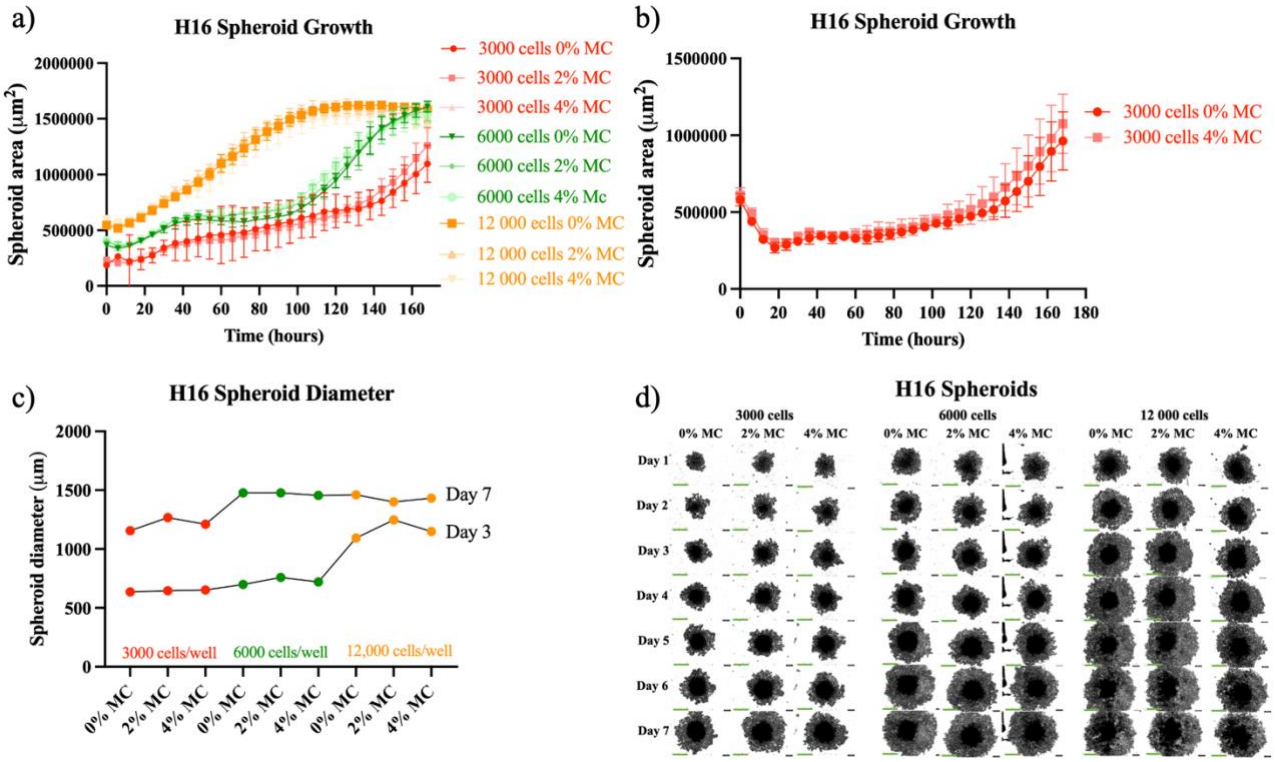

Figure 4.6 - Growth of spheroids formed with H16 cells: *a) The growth of spheroids composed of H16 cells with varying concentrations of cells and methylcellulose, represented by their area measured in µm^2 over 7 days. b) 7-day growth of spheroids seeded as 3,000 cells/mL, with 0 % and 4 % methylcellulose. c) Comparison of the spheroid diameters at days 3 and day 7, measured in µm. d) Microscopic images of each spheroid throughout the 7-day incubation period. All scalebars are 400 µm. MC = methylcellulose.*

4.7 Heterogenous Spheroids with Astrocytes

Normal human astrocytes (NHA) were mixed with LBM1 or H16 cells to study the interactions between the two cell types in a more physiologically relevant model. Varying ratios of cancer cells and astrocytes were seeded to investigate the potential role of NHA in promoting or inhibiting cancer cell growth. As displayed in **Fig. 4.7 a**, the spheroids composed of LBM1 and NHA cells showed that the addition of NHA did not affect the growth of the spheroids. As expected, considering the results presented in section 4.5, spheroids composed of LBM1 and NHA (**Fig. 4.7 a**) were larger in size compared to those composed of H16 and NHA (**Fig. 4.7 b**). Both spheroids composed of LBM1 and NHA, and of H16 and NHA, displayed an initial drop in surface area due to the gradual aggregation of the cells over the first hours.

Neither the spheroids composed of LBM1 cells and NHA, nor H16 cells and NHA, were markedly affected by the addition of NHA. In comparison to the homogenous spheroids depicted in **Fig. 4.5 a** and **4.6 a**, the growth of the heterogeneous spheroids was only slightly smaller. In contrast, the spheroids composed of NHA only were significantly smaller and did not grow, in comparison to both the LBM1- and H16-cells only-spheroids and heterogeneous spheroids (**Fig. 4.7 a-b**). **Fig. 4.7 c** displays their respective size at day 6, visually demonstrating the notable size difference between the spheroids.

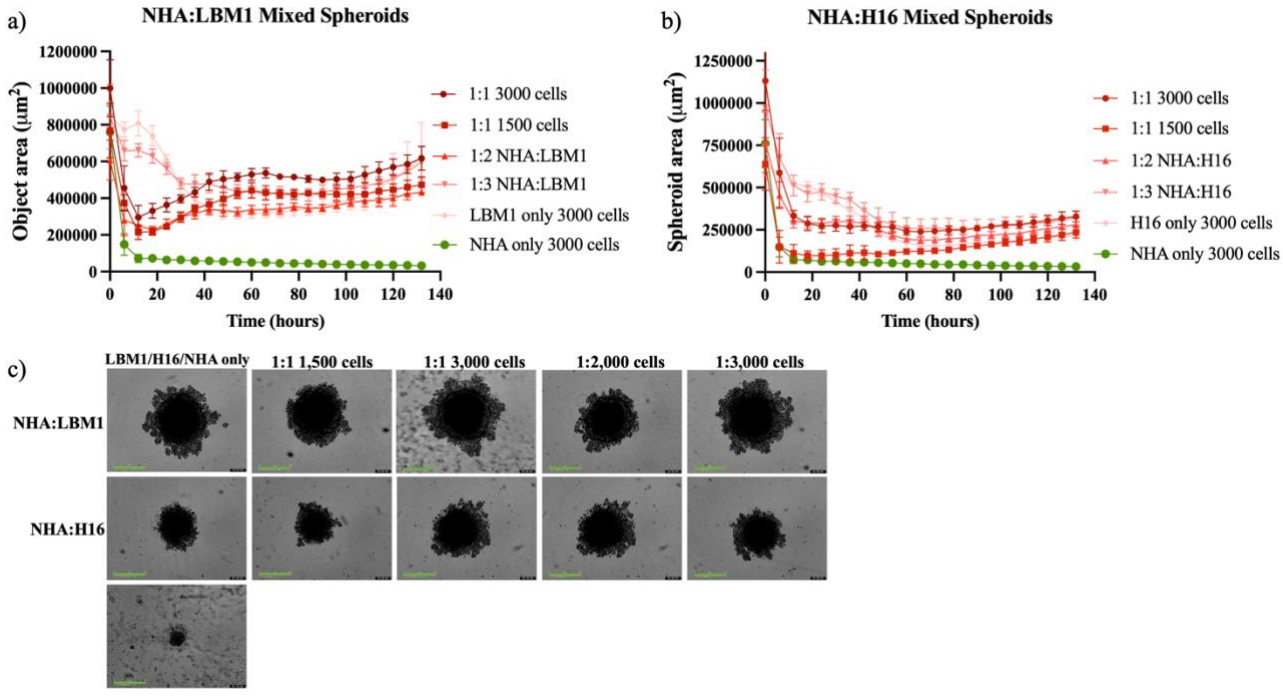

Figure 4.7 – Growth of heterogeneous spheroids composed of NHA and LBM1 or H16 cells: *a) Growth curve displaying the growth pattern of spheroids composed of NHA and*

LBM1 cells, represented by their area measured in μm^2 over 6 days. b) Growth curve displaying the growth pattern of spheroids composed of NHA and H16 cells, represented by their area measured in μm^2 over 6 days. c) Images of the spheroids on day 6, to visually compare their overall sizes, shapes, and the size of their cores. Spheroids seeded with LBM1 cells, H16 cells and NHA only, were seeded as 3,000 cells/well. All scalebars are 400 μm.

4.8 Thioridazine Effectively Reduces Cell Viability

LBM1 and H16 cells were treated with thioridazine for 72 h to examine the effectiveness of the drug in inhibiting the growth of the BM cell lines. As seen in **Fig. 4.8 a** and **b**, thioridazine effectively inhibited the viability of both LBM1 and H16 cells with concentrations of 11 μM and beyond. The average IC_{50} dose (half maximal inhibitory concentration) for LBM1 cells after three replicates was 11,09 μM, meaning that this concentration of thioridazine is required to inhibit the growth of the cells by 50 % compared to untreated LBM1 cells. Similarly, for H16 cells, an average of 10,98 μM of thioridazine was required to inhibit cellular viability by 50 %.

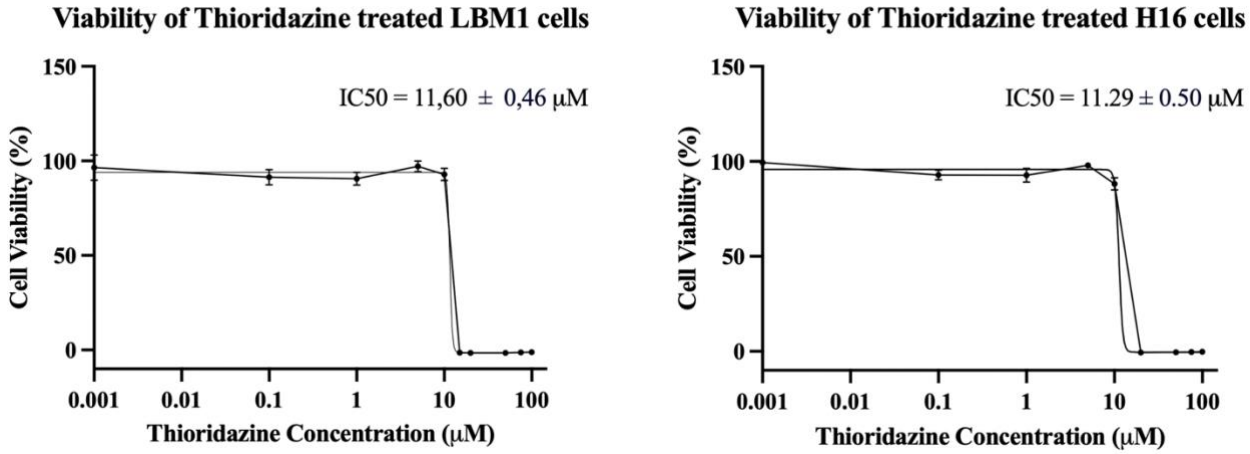

Fig. 4.8 – Viability graphs of LBM1 (a) and H16 (b) cells from WST-1 assay over 72 h: *The cells were treated with concentrations of thioridazine ranging from 0,1-100 μM to determine an IC_{50} dosage.*

4.9 Immunohistochemical Analysis of BM Cell Lines

Four BM cell lines were analysed with IHC to assess the expression of specific markers typically observed for the specific types of cancer: LBM1, H16, BrBM1 and BrBM2. Based on the results shown in **Fig. 4.9 a**, LBM1 was determined to be of non-small cell lung carcinoma (NSCLC) origin, specifically adenocarcinoma. The positive staining for CK7 (97,6 %) and TTF1 (95,6 %) confirms the lung lineage and adenocarcinoma properties, respectively. Although Napsin A was not expressed in LBM1 cells, the positive expression of TTF1, a widely used adenocarcinoma marker, provided sufficient indication that the cell line

is of adenocarcinoma origin. CK5/6 is typically negative in adenocarcinoma in contrast to other NSCLCs, such as large cell and squamous carcinomas, providing additional support to the diagnosis of adenocarcinoma. The negative staining for CK5/6 and p63, therefore, confirms that the tumour is not squamous cell carcinoma. Synaptophysin and chromogranin A are markers of neuroendocrine differentiation and are, therefore, negative in adenocarcinoma.

H16 was as confirmed by the IHC analysis, a melanoma cell line expressing SOX10 and S100 (**Fig. 4.9 b**). SOX10 and S100 are markers of malignant melanoma. Hence, their weak staining (0,53 and 0,98 %, respectively) still classifies them as melanoma. However, negative expression of Melan-A and HMB45 is atypical of melanoma cell lines. Thus, these findings are indicative of the loss of expression of these typical melanoma markers from the primary tumour from which the H16 cells were derived.

The IHC analysis confirms that BrBM1 and BrBM2 are TNBC cell lines (**Fig. 4.9 c**), as neither cell line expresses ER, PR, or HER2. Weak cytoplasmic CK7 expression was detected for both BrBM cell lines, as 3,6 % (BrBM1) and 11,12 % (BrBM2) of the cells expressed this marker.

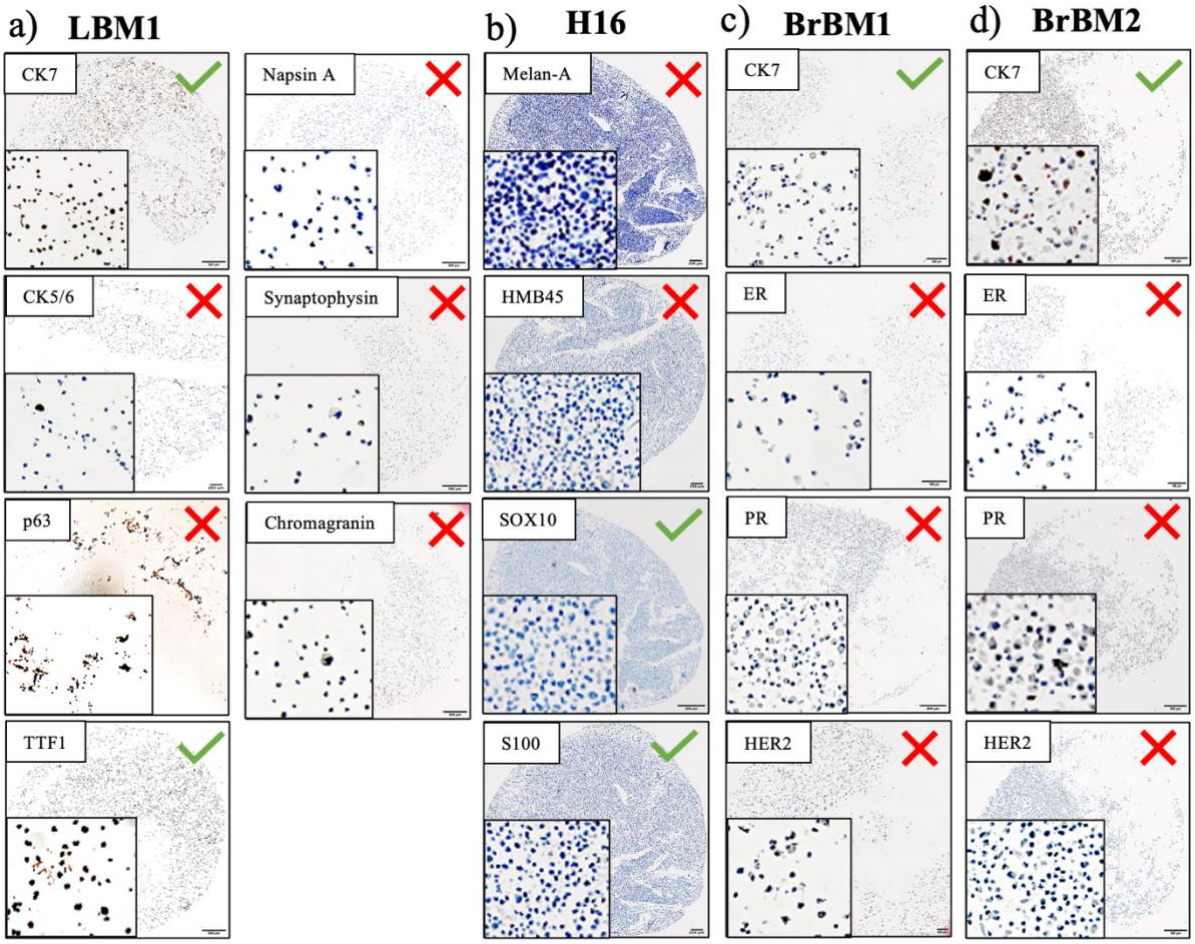

Figure 4.9 – Immunohistochemical results for four BM cell lines with different origins*: a) The immunohistochemical results for LBM1, a lung cancer BM cell line. The analysis confirms a NSCLC diagnosis. b) The immunohistochemical results of H16 support the diagnosis of melanoma. c-d) The immunohistochemical analysis of two breast cancer BM cell lines, confirming TNBC. Diaminobenzidine (DAB) was used to reveal positively stained cells. Green checkmark = positive expression. Red cross = negative expression.*

4.10 *In Vivo* Injection of BM Cells to Investigate Their Tumourigenic Potential

The brains of LBM1 and H16 injected mice were scanned using MRI at weeks 2 and 4 (**Fig. 4.10.2**) to identify the tumours that formed. BrBM1 and BrBM2 cells were not injected due to their slow growth rate. **Fig. 4.10.1** shows the survival of the mice following the injection of the cells. It was necessary to euthanize the two male mice injected with H16 cells due to aggressive behaviour, thus suffering and discomfort. The median survival time for mice intracardially injected with LBM1 cells was 39 days after injection and 48 days for mice injected with H16 cells. Excluding the two mice that were euthanized due to unrelated causes, it was observed that mice injected with H16 cells exhibited a 23 % longer survival time

compared to those injected with LBM1 cells. Despite the limited sample size, the data yielded representative outcomes that provide insights into the tumorigenic potential of the two BM cell lines.

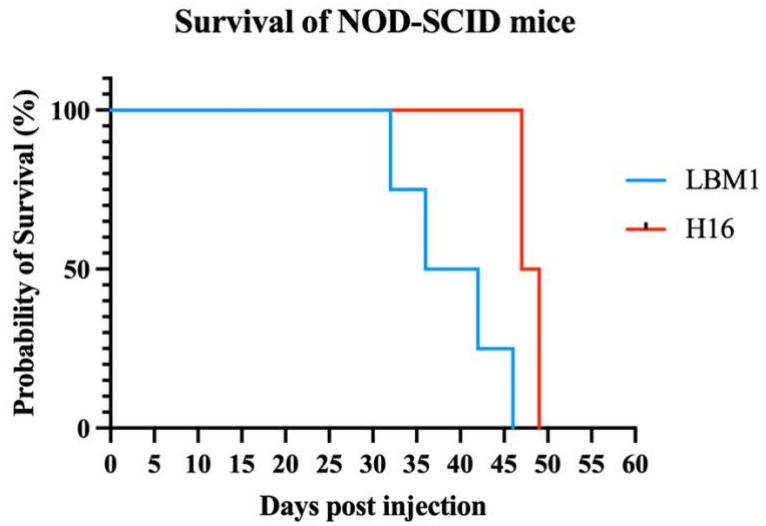

Figure 4.10.1 – Kaplan Meier survival curve for eight NOD-SCID mice intracardially injected with LBM1 cells (blue) or H16 cells (red): *The graph shows the days following injection on day 0, plotted against probability of survival in percentage, with day 0 counting as 100 % viability. The two male mice administered with H16 cells were excluded from this dataset, as they were euthanized due to causes unrelated to tumour formation.*

As displayed in **Table 4.10.1**, no tumours were observed two weeks after injection for either cell line. However, on the scans from week 4, three of the mice injected with LBM1 cells displayed signs of tumours arising in different areas of the brain (**Fig. 4.10.2**). The two male LBM1-injected mice exhibited one tumour each in the mid-frontal lobe, of 0,016 mm^3 and 0,034 mm^3, respectively (**Table 4.10.2**). The first female LBM1-injected mouse had a significantly larger tumour at the left interface between the frontal and temporal lobe, with a volume of 37,28 mm^3 (**Table 4.10.2**). None of the H16-injected mice exhibited tumour formation at week 4. However, this observation does not preclude the possibility of tumour development in subsequent stages. Due to maintenance on the MRI machine, a scan on week 6 was not performed as initially planned, as the scanner downtime was longer than first anticipated. Thus, all mice were sacrificed before the next MRI scan was possible. All brains were therefore harvested after sacrificing the animals.

Table 4.10.1 – Scanning schedule and observed BM in mice injected with LBM1 or H16 cells:

Cell line:	Week 2	Week 4
LBM1	0/4	3/4
H16	0/4	0/4

Table 4.10.2 – Dimensions of tumours observed in LBM1-injected mice at week 4:

	LBM1 ♂ mouse 1	LBM1 ♀ mouse 1	LBM1 ♂ mouse 2
Dimensions (mm):	0,4 x 0,4	0,31 x 0,31	6,15 x 2,14
Volume (mm^3):	0,034	0,016	37,28

The remaining mice injected with H16 cells were euthanized as a result of evident signs of distress, indicating the presence of intra- or extracranial tumours manifesting physical discomfort in the animals. *Ex vivo* MRI scans were performed of all brains, but the image quality was too poor to make firm conclusions on intracranial tumour burden. Thus, histology on these brains will be done in the future for studies on tumour development, as there was no time available to include the analysis in this thesis.

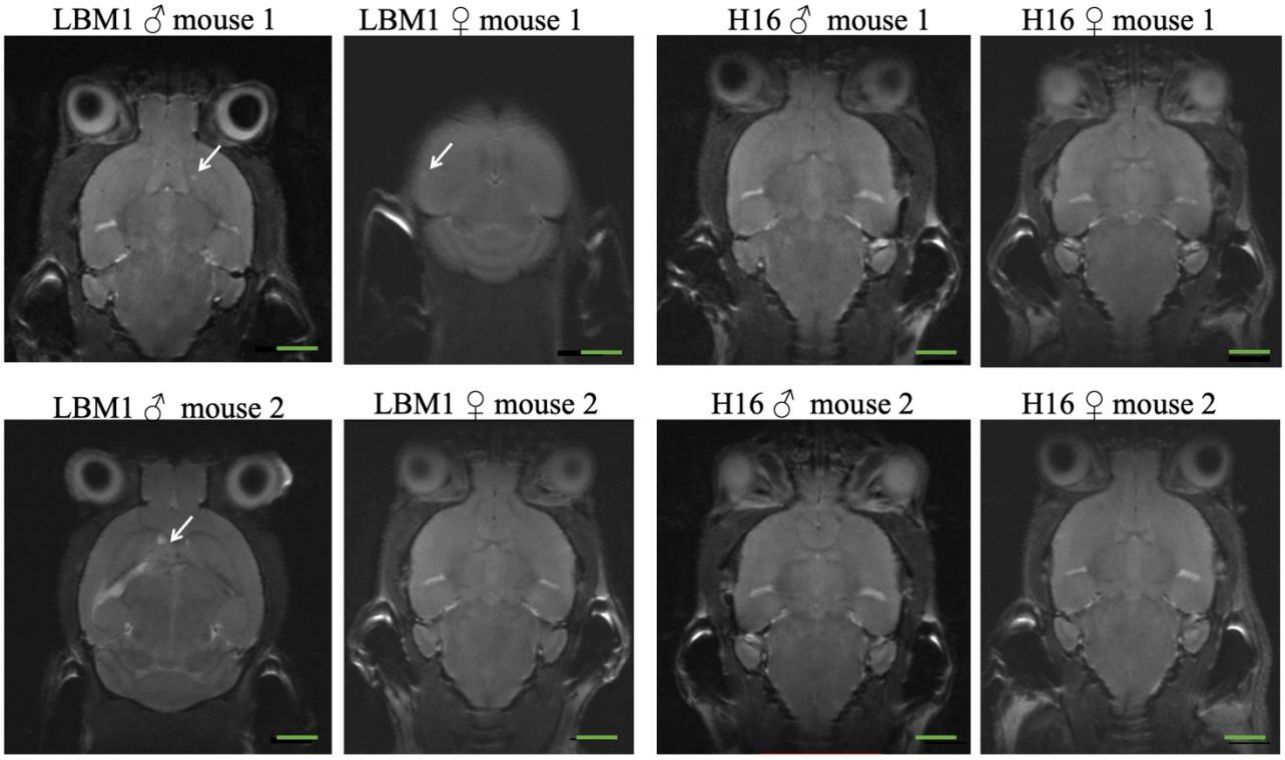

Figure 4.10.2 – MRI scans of mice injected with LBM1 and H16 cells*: T2W MRI scans of male and female mouse brains, at week 4 (the two male H16-injected mice were only imaged at week 2) following injection with the two BM cell lines. No tumours were observed at the two-week time point (scans not included), but tumours were apparent in three of the four LBM1-injected mice at week 4, with volumes of 0,034, 0,016 and 37,28 mm^3, respectively. All scalebars are 100 mm. All images were acquired with the parameters stated in section 3.11.*

4.11 Successful Isolation of Exosomes from BM Cell Lines

Differential centrifugation separated particles in the conditioned culture medium from LBM1 and H16 cells. Exosomes were not isolated from BrBM1 and BrBM2 due to their slow growth rates. TEM was done to verify that the isolation procedure was successful at isolating exosomes from other EVs. When viewed with TEM, the lipid bilayer of the exosomes appeared as two parallel membranes with a hydrophobic space between them, as depicted in **Fig. 4.11.1 a-c** (white arrows). Some exosomes also exhibited an irregular and rough surface (**Fig. 4.11.1 c**).

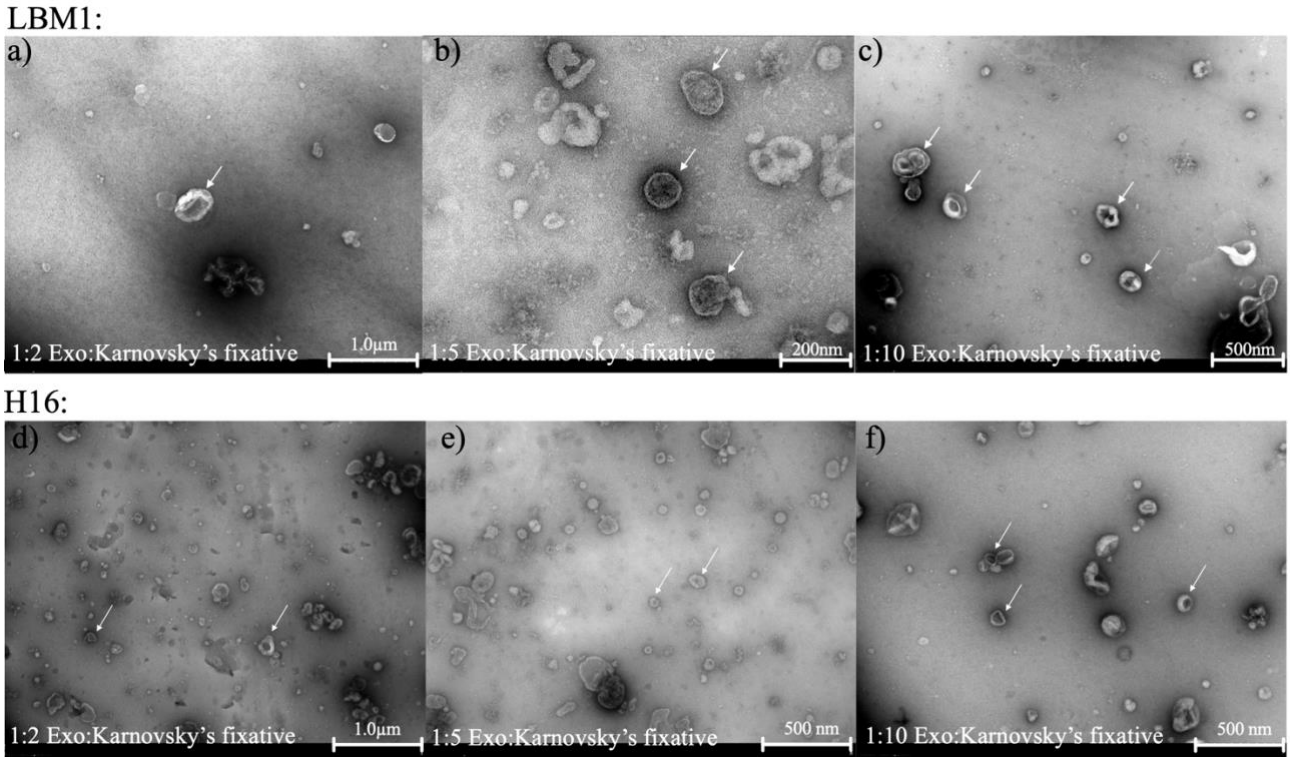

Figure 4.11.1 – Exosomes viewed by TEM to confirm successful isolation: *a-c) LBM1 derived exosomes isolated using differential centrifugation d-f) H16 derived exosomes isolated using differential centrifugation. The white arrows indicate exosomes.*

Successful isolation of exosomes was also verified by Western blot. The results in **Fig. 4.11.2**, revealed that calnexin, the positive marker for cells, was not expressed in the exosomes. The exosomal markers Flotillin-1, Tsg-101, CD9, and CD81 were positive in all exosomal samples while negative in cell samples. This effectively ensured the absence of contaminating materials such as other types of EVs in the isolated samples from LBM1 and H16 cells.

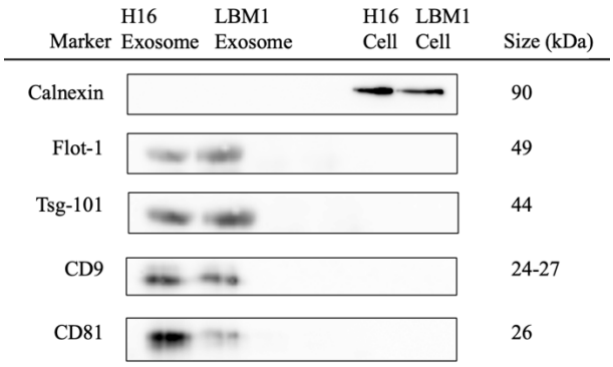

Figure 4.11.2 – Western blot to confirm the presence of exosomal markers and absence of a cell-specific marker*: The western blot was done to ensure the reliability and accuracy of the isolation process, as recommended by ISEV. Calnexin was used as a negative marker for exosomes, and Flot-1, Tsg-101, CD9, and CD81 were used as indicators of exosomal presence in the samples. The combination of the absence of calnexin and the presence of the four positive markers confirmed the successful isolation of exosomes from the conditioned culture medium derived from LBM1 and H16 cells.*

To further support the evidence of successful exosome isolation and to ensure consistency and quality across all isolated exosome batches, DLS was utilised as a third analytical step. The exosome samples were resuspended in 1x PBS to obtain the following concentrations: 5x, 10x, and 50x. As seen in **Table 4.11**, a 50x dilution of the samples provided the most reliable outputs across triplicates, as the exosomes observably aggregated the least when using this concentration. The observed size of 154,3 nm for LBM1 cells, and 159,1 nm for H16 cells, falls within the typical size range previously reported for exosomes (**Fig. 4.11.3 a-b**).

The shape of the size distribution curve (**Fig. 4.11.3**) revealed details about the nature of the exosomes. As seen in **Fig. 4.11.3 b**, the curve is broader compared to the curve seen in **Fig. 4.11.3 a**. The broad curve, in combination with multiple smaller peaks, indicated a polydisperse sample, with particles of different sizes. The curve in **Fig. 4.11.3 a** showed a sharper peak indicating a more monodisperse sample, yet multiple peaks were observed. The position of the most prominent peak corresponded to the most abundant particle size in the sample, taking both the size, shape, and surface charge into consideration.

Table 4.11 – DLS output for three different sample dilutions in 1x PBS:

	LBM1			*Average*	**H16**			*Average*
5x	255,6	254,7	152,3	*220,86*	172,6	489,9	163,6	*275,4*
10x	366,4	204,4	208,9	*259,9*	159,1	433,1	177,2	*226,8*
50x	198,2	200.2	154,3	*184,2*	160,9	342,0	169,7	*224,2*

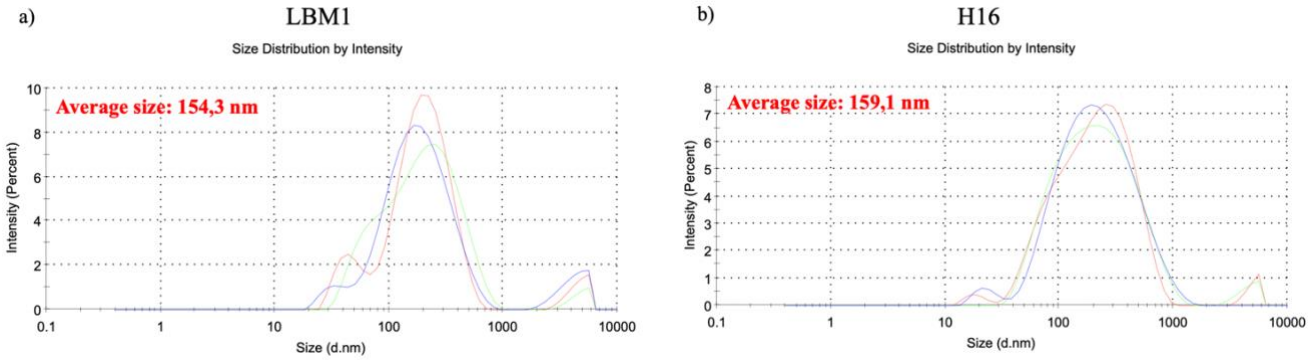

Figure* Fig. 4.11.3 – *The size distribution plot obtained from DLS analyses*: The plot obtained from DLS analyses provided information about the size (in nm) and relative abundance of the particles in the samples represented by the intensity of the scattered light (%). a) Size distribution plot LBM1-derived exosomes diluted 50x in 1x PBS. b) Size distribution plot H16-derived exosomes diluted 50x in 1x PBS.***

Although the DLS analyses suggested exosome size distribution profiles toward the upper end of the size spectrum described in the literature, the presence of exosomal markers and absence of a negative exosomal marker, in addition to the visual examination using TEM, the results provide strong evidence that differential centrifugation of conditioned culture medium successfully isolated exosomes from both LBM1 and H16 cells.

4.12 Electroporation of Exosomes to Incorporate Iron Oxide Particles

Electroporation of exosomes isolated from LBM1 and H16 cells was done to integrate carboxyl-coated SPIONs into the lumen of the exosomes (**Fig. 4.12.1** and **Fig. 4.12.2**). Due to a limited quantity of exosomes derived from H16 cells, the electroporation was only performed with a restricted number of experimental groups, namely protocols 1 and 3, in addition to an untreated control. However, the selected protocols provided a valid basis for evaluating the effects of electroporation on H16-derived exosomes under the given experimental conditions. The images in **Fig. 4.12.1 a-f** and **Fig. 4.12.2 a-c** were used to compare the control and the electroporated samples. Exosomes that are successfully electroporated and thus contain SPIONs should appear darker than non-electroporated exosomes when viewed with TEM, due to the iron oxide particles absorbing more electrons than the exosome membrane. Given the visual comparison depicted in **Fig. 4.12.1 a-f** and

Fig. 4.12.2 a-c, determining the effectiveness of electroporation solely based on the variance in colour proved to be challenging. Some aggregation was observed amongst the exosomes electroporated in the sucrose buffer (conditions 3 and 4) compared to those electroporated in the trehalose buffer (conditions 1 and 2) (**Fig. 4.12.1 c-d** and **Fig. 4.12.2 b**).

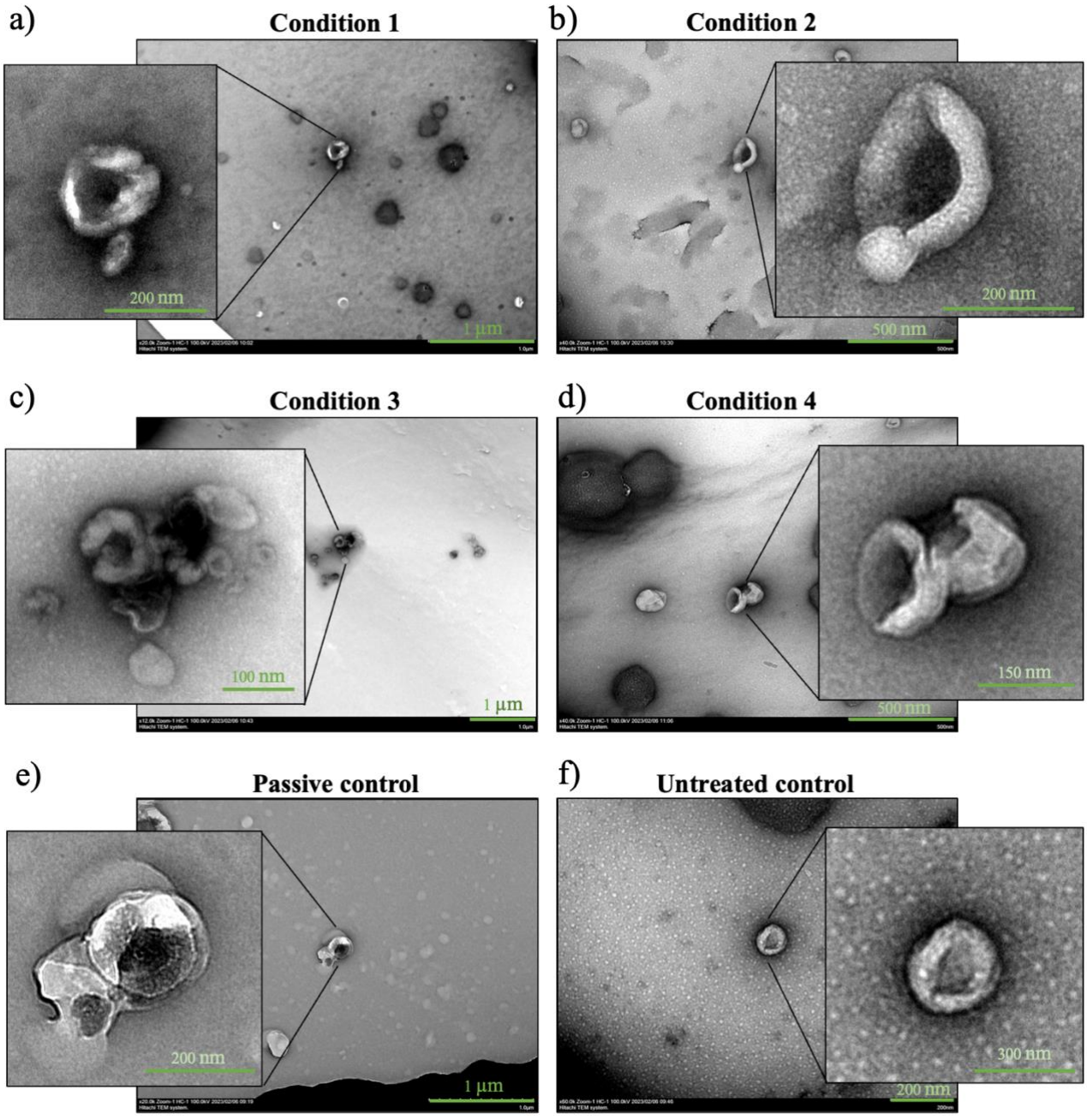

Figure 4.12.1 – TEM images of electroporated exosomes derived from LBM1 cells*: Four different protocols were followed when electroporating the exosomes derived from LBM1 cells. The protocols differed both in procedure and buffers used (**Table 3.19**), but 50 µg of exosomes, and 2,5 ug/mL SPIONs were used across all conditions. a) Protocol 1 used a 50 mM trehalose buffer, 0,300 kV voltage and a capacitance of 950 µF, and only one pulse was given. b) Protocol 2 used the same parameters, but two pulses were given. c-d) Protocols 3 and 4 used a 1:1 ratio of a 400 mM sucrose solution and 1x PBS, a voltage of 950 kV, and a capacitance of 50 µF. One pulse was given for protocol 3, and two pulses for protocol 4. e-f)*

The passive incubation control and the untreated control were both resuspended in 1x PBS without undergoing electroporation.

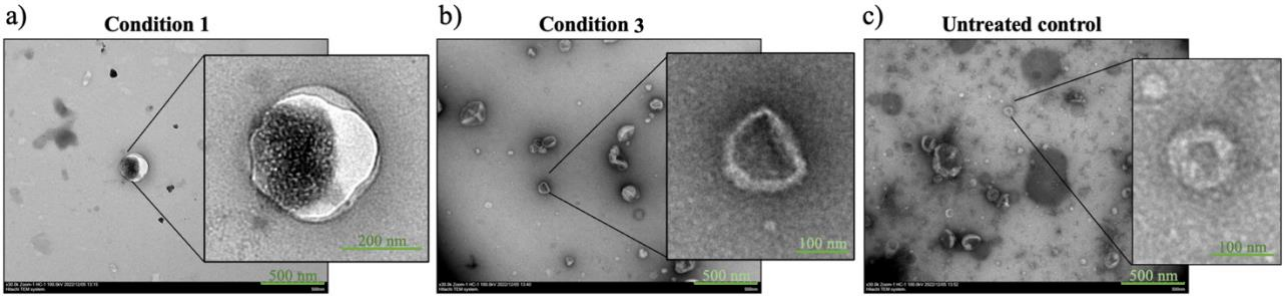

Figure 4.12.2 – TEM images of electroporated exosomes derived from H16 cells*: a) Exosomes derived from H16 cells were electroporated following protocol 1 listed in* ***Table 3.19****. b) Exosomes derived from H16 cells were electroporated following protocol 3 (****Table 3.19)****. c) H16-derived exosomes that underwent no electroporation were used as untreated controls for comparison.*

4.13 Prussian Blue Staining to Detect Cellular Uptake of SPIONs

To assess the ability of the LBM1 cells to take up iron oxide particles, the cells were first incubated with varying concentrations of carboxyl-coated SPIONs; 10 µg/mL (**Fig. 4.13.1 a**), 20 µg/mL (**Fig. 4.13.1 b**), and 30 µg/mL (**Fig. 4.13.1 c**). LBM1 cells were used for this pilot experiment due to their rapid proliferation. As shown in **Fig. 4.13.1**, LBM1 cells did not take up the carboxyl-coated iron oxide particles, as evidenced by the lack of blue staining.

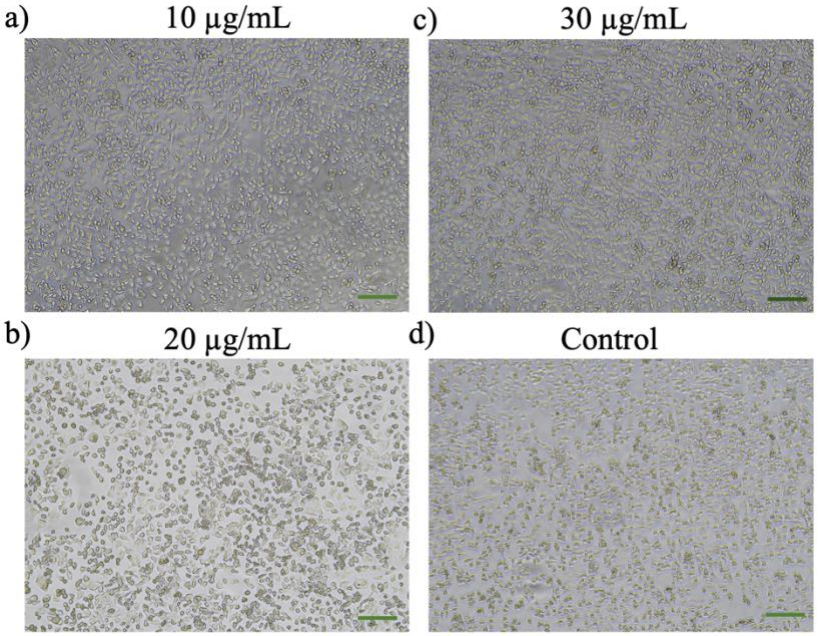

Figure 4.13.1 – Microscopic images of LBM1 cells after 48 h incubation with carboxyl-coated SPIONs and staining with Prussian blue*: a) LBM1 cells incubated with a) 10 µg/mL SPIONs, b) 20 µg/mL SPIONs and c) 30 µg/mL SPIONs. d) Control cells that were not incubated with SPIONs. All scalebars are 200 µm, and images were taken using a 10x objective.*

Based on these results, SPIONs with a dextran coating were used to investigate whether the coating could be responsible for the inability of the cells to uptake the iron oxide particles. The same protocol for Prussian blue staining was followed and the cells were incubated with SPIONs for 24 h and 48 h, with concentrations ranging from 2,5-30 μg/mL. The dextran-coated SPIONs were successfully taken up by the LBM1 cells, as evidenced by the blue pigment seen in **Fig. 4.13.2**. No discernible visual distinction was observed between the cells subjected to 24 h and 48 h incubation periods. This confirms that the carboxyl-coating on the SPIONs initially used, was likely the reason for the lack of internalisation of the iron oxide particles by LBM1 cells.

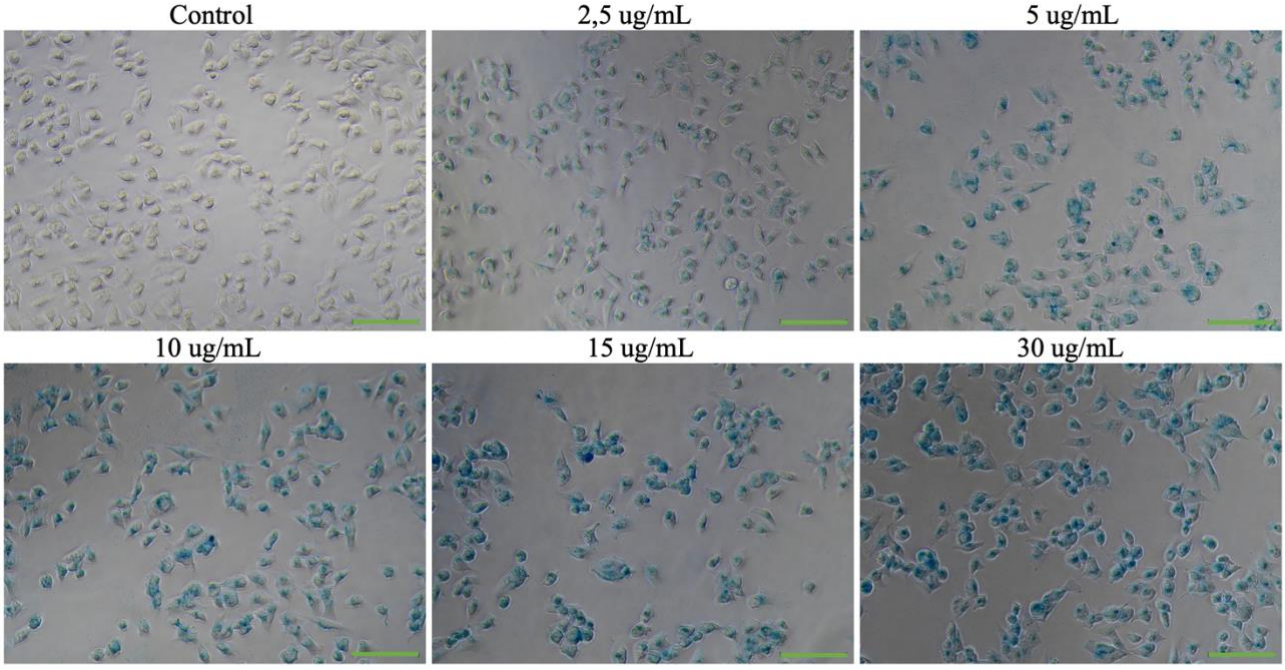

Fig. 4.13.2 – Microscopic images of LBM1 cells after 24 h incubation with dextran-coated SPIONs and Prussian blue staining*: LBM1 cells incubated with dextran-coated SPIONs for 24 h with concentrations ranging from 2,5-30 μg/mL, followed by Prussian blue staining to visualize the cells that had taken up the nanoparticles. All scalebars are 100 μm, and images were taken using a 20x objective.*

As displayed in **Table 4.13.1** and **Fig. 4.13.2** and **Fig. 4.13.3**, nearly 100 % of the cells internalised the dextran-coated SPIONs both when incubated for 24 and 48 h. Concentrations of 2,5 μg/mL and above provided effective uptake, but satisfactory labelling was achieved using 10 μg/mL (**Fig. 4.13.2** and **Fig. 4.13.3**).

Table 4.13.1 – The average number of positively stained cells following 24 h incubation with dextran-coated SPIONs:

Concentration	Average number of positive cells (%)	SD
2,5 µg/mL	97,33	1,3
5 µg/mL	98,88	1,09
10 µg/mL	99,58	0,52
15 µg/mL	99,58	0,58
30 µg/mL	99,76	0,41

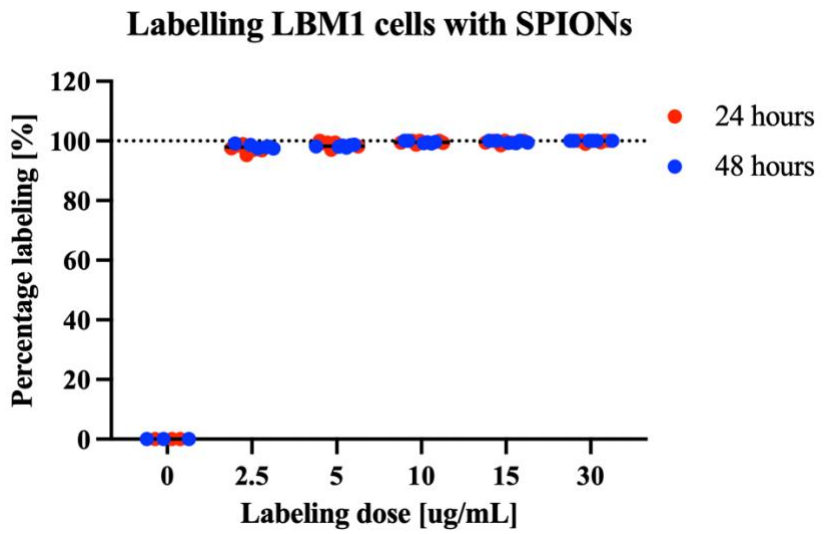

Fig. 4.13.3 – Labelling of LBM1 cells with dextran-coated SPIONs: *LBM1 cells incubated with dextran-coated SPIONs for 24 h with concentrations ranging from 2,5-30 µg/mL. The graph shows that concentrations from 2,5 µg SPIONs per mL culture media resulted in high uptake, both when incubated for 24 and 48 h. No significant differences were seen between the two incubation lengths.*

To evaluate the potential influence of dextran-coated SPIONs on cellular viability, a t-test was employed with a significance level (alpha value) of 0,05 to determine whether statistically significant differences existed in the total cell count between unlabelled cells and cells labelled with dextran-coated SPIONs. As displayed in **Table 4.13.2** and visualized in **Fig. 4.13.4**, only a slight discrepancy between the labelled cells and the control cells was seen for almost all concentrations across both incubation times. Only one parameter displayed discrepancy, namely cells incubated with 30 µg/mL for 48 h. Except for this one parameter, the data, therefore, suggests that the SPIONs did not significantly affect the cell growth or viability at any of the concentrations or incubation times employed.

To conclude, for this cell line, a labelling concentration of 10 µg/mL and an incubation duration of 24 h will be used for future experiments using LBM1 cells, as no significant

differences were observed between this protocol and the alternative 48 h incubation length, and cell proliferation was not affected by this labelling dose.

Table 4.13.2 – Unpaired t-test values to determine whether there was a statistically significant difference between the number of cells labelled with dextran-coated SPIONs and unlabelled cells:

Concentration	P-value 24 h incubation	P-value 48 h incubation
2,5 μg/mL	0,31	0,92
5 μg/mL	0,16	0,45
10 μg/mL	0,51	0,27
15 μg/mL	0,25	0,29
30 μg/mL	0,36	0,01

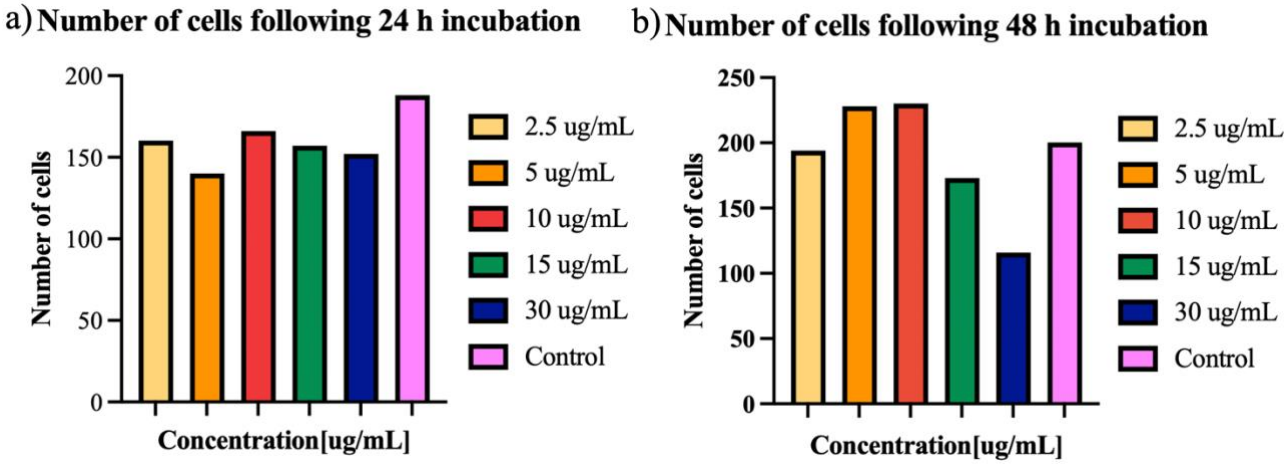

Fig. 4.13.4 – Total number of cells following labelling with dextran-coated SPIONs: *The total number of labelled cells following 24 h (a) and 48 h (b) incubation with dextran-coated SPIONs with concentrations ranging from 2,5-30 μg/mL, compared to the number of control cells to examine the cellular toxicity of the nanoparticles.*

5.0 Discussion:

Palliative management is often the treatment of choice for BM patients, as the metastatic spread that is often seen with tumours from lung, breast, or melanoma, results in limited treatment success and minimal improvements in patient survival. In the absence of medical intervention, most BM patients die shortly after diagnosis[108]. One possible explanation for the poor survival is likely the inability of many current chemotherapeutic agents to cross the BBB. The search for alternative pharmacological approaches, such as the repurposing of thioridazine, which is able to penetrate into the brain, in addition to the use of improved model systems to fully understand the complex interplay between cancer cells and normal brain cells, is therefore vital to improve the survival of BM patients. Thus, this master project aimed to establish new *in vitro* and *in vivo* model systems for BM research, by investigating the potential of different BM cell lines derived from patient biopsies, including but not limited to, the evaluation of their proliferation properties, tumour-stromal interactions, and *in vivo* tumourigenesis.

5.1 Growth Characteristics of BM Cell Lines

Four BM cell lines developed from different primary tumours were characterised in this project. LBM1 and H16 cells, derived from lung and melanoma BM respectively, grew well in the DMEM-ALT culture medium, while BrBM1 and BrBM2 cells, derived from breast cancer BM, displayed a significantly reduced growth rate in DMEM-ALT in comparison to LBM1 and H16 cells. They were therefore cultured in Advanced DMEM/F12 culture medium supplemented with the same additives as DMEM-ALT (**Table 3.1**), in addition to insulin. Insulin was added to the growth medium, as it has been reported to increase mitogenic effects of breast cancer cells in culture[109]. This improved their proliferative potential to a limited extent, but their growth remained restricted in comparison to the lung and melanoma cell lines. Future culturing of BrBM1 and BrBM2 cells may benefit from the addition of estrogen to the culture medium, as the combination of insulin and estrogen has been shown to synergistically enhance the growth of breast cancer cells *in vitro*[109]. However, neither BrBM1 nor BrBM2 cells expressed ER as described in section 4.9, hence, the same favourable impact on their growth may not be observed. While optimising growth conditions is critical to promote the ideal growth of cells, experimenting with culture conditions is a time-consuming process that was not feasible within the project timeline, and therefore, the focus was directed towards LBM1 and H16 cells. Further optimisation of the growth

conditions for BrBM1 and BrBM2 cells is therefore necessary for them to be used in future breast cancer BM research.

The focus of the project was thus to continue with LBM1 and H16, through characterising their properties and behaviour *in vitro*, including evaluation of their growth patterns and doubling time. LBM1 cells showed the strongest proliferative ability between the two. When cultured with a seeding ratio of 1:10, the cell line required passaging after 3-4 days, even after continuous culture beyond 10 passages. These findings position LBM1 cells as a promising candidate for conducting research on lung cancer BM. In comparison, H16 cells with a seeding density of 1:5 required passaging after the same number of days. However, these cells displayed a decline in proliferation beyond passage number 29, possibly providing a reflection of the cell health[110,111], which resulted in variable data for H16 cells when used after passage 29 (data not included). Therefore, using a low passage number is vital when working with H16 cells.

To conclude, the overall proliferative capacities of LBM1 and H16 cells highlight the advantageous properties exhibited by these BM cell lines, making them valuable tools for further utilisation in model systems.

5.2 Morphological Differences

The rounded shape and short filopodia of LBM1 cells revealed morphological characteristics similar to epithelial cells (**Fig. 4.4 a**), which is not unexpected given that these cells were derived from human lung cancer BM. Despite the resemblance, LBM1 cells exhibited a reduced differentiation with respect to filopodia compared to *in vivo* epithelial cells, as the filopodia were short and scarce. In contrast, H16 cells were more rounded compared to previously described primary melanoma cell lines, which typically display more extensive surface projections[112]. The cytoplasm of H16 cells contained structures suggesting an abundance of e.g., rough ER, free ribosomes, mitochondria, and/or melanosomes, the melanin-synthesizing organelles (**Fig. 4.4 b**). BrBM1 and BrBM2 cells were in stark contrast to the other two BM cell lines (**Fig. 4.4 c-d**, respectively). The stellate morphology exhibited by BrBM1 and BrBM2 cells has previously been documented by Kenny et. al.[113], whose cells with similar morphology were derived from a patient with basal-like breast cancer, a subtype of breast cancer that is widely regarded as closely associated with TNBC. Thus, these

morphological features are not atypical for the cell type. However, the irregular and flattened morphology made it challenging to visualize the cells under the microscope. Their flat morphology further challenged the process of establishing optimal parameters for use in growth assays, as the IncuCyte live imaging system did not accurately differentiate between the cells and the background.

In conclusion, the LBM1 and H16 cells maintained a consistent morphology across continuous passaging, enabling the establishment of a standard baseline of their behaviour and characteristic morphological features. This implies that the cells are suitable for long-term studies.

5.3 Strong 3D Spheroid Formation for *In Vitro* Modelling

The conventional 2D monolayer culturing of cells does not reveal the complex interplay between the cancer cells and the cellular microenvironment during metastasis. Therefore, *in vitro* models of both lung and melanoma BM cell lines were generated to study their ability to self-organize into three-dimensional structures resembling the *in vivo* architecture, thus providing an accessible and biologically relevant model. Spheroids seeded with 12,000 cells/well in **Fig. 4.5 a** and **Fig. 4.6 a**, demonstrate that the spheroids have a maximum size limit, observed on day 3 for LBM1 cells and day 4 for H16 cells. This rapid saturation and subsequent plateau phase were likely attributed to the high seeding number of cells causing a dense core that was depleted of oxygen. This led to a state of hypoxia which ultimately resulted in necrosis of the core, thus inhibiting further growth. Such spheroids, accompanied by layers of quiescent cells, have been shown to be less suitable for drug toxicity assays, as the reduced number of proliferative cells may yield unreliable results[114]. It has however, been mathematically proven by Browning et.al., that spheroids of the same cell line seeded at different concentrations, eventually grow to a certain maximum size, independent of the initial number of cells used[115]. Considering this, spheroids seeded at a density of 3,000 cells/well would be the most optimal for both LBM1 and H16 cells, as this number produced stable spheroids while still allowing sufficient space for the growth and maintenance of their shape over the span of 7 days and beyond. This seeding density should therefore be used for subsequent experiments using these BM cell lines to generate three-dimensional spheroids.

The spheroids seen in **Fig. 4.5 b, Fig. 4.6 b**, and **Fig. 4.7 a** and **b**, all exhibited an initial drop in the spheroid surface area. This was caused by the initial aggregation of the cells into a more dense structure over the first 24 h. It has been shown that cells initially form loose cell-cell connections between integrins and the ECM, before forming tighter connections between N-cadherin-to-E-cadherin interactions[116]. Once the spheroids had stabilized and grew as a cohesive entity, they were analysed by the predetermined masking parameters in the IncuCyte live imaging system, to measure the largest object area in the well.

For future characterization of spheroids, TEM can be utilised to image cell junctions within a compact spheroid. Additionally, preliminary western blots can be done to detect the highest level of E-cadherin expression across different cell lines, as this indicates a strong ability to form tight cell-cell interactions within a spheroid[116].

As discussed by Friedrich and colleagues, the clinical relevance of spheroids is partly attributed to the genetic resemblance of the clinical expression of 3D structures derived from tumour biopsies, in comparison to 2D monolayers from the same tumour cells[117]. Spheroids derived from patient biopsy cell lines can therefore be used as a prognostic personalisation strategy, where drugs, or a combination of drugs, can be tested to assess the best therapeutic response *ex vivo* through measurements of their viability and IC_{50} doses, before administering the drug(s) to the patient[118,119]. In a study by Shuford and colleagues on patient-derived spheroids for response predictions of ovarian cancer patients, an overall prediction accuracy of 89 % proves the relevance and potential of spheroids in predicting a patient-specific response, before initiating treatments in the clinic[120].

In conclusion, spheroids provide a valuable tool for drug screening and for predicting a personalised treatment response *ex vivo*. Methylcellulose was not required for the spheroid formation of LBM1 cells, as was also seen with H16 cells, as they were capable of forming tight cell-cell interactions to form stable and consistent spheroids, which maintained their well-organized morphology when seeded as 3,000 cells/well. The spheroid experiments provided insight into their characteristics and behaviour in a microenvironment that closely mimics that of *in vivo* tissue and demonstrated their tumour-like phenotype. Subsequent objectives of spheroid formation using these BM cell lines, may therefore include drug screening and efficacy testing of e.g., thioridazine, to assess their response, sensitivity, and

resistance. Concurrently, confocal microscopy or live-cell imaging can be utilised to monitor dynamic processes such as cellular interactions, and responses to drugs within the spheroids.

5.4 Heterogenous Spheroids Comparable to Homogenous Spheroids

A 3D coculture spheroid model was developed, consisting of BM cell lines and astrocytes, to study if the interaction between normal cells and tumour cells would affect spheroid growth. The heterogeneous spheroids seen in **Fig. 4.7**, displayed similar characteristics to the homogenous spheroids seen in **Fig. 4.5 a** and **Fig. 4.6 a**. The heterogeneous spheroids displayed a slightly smaller size when compared to their homogeneous counterparts, which can be attributed to the reduced spatial niche available for the BM cells, which was occupied by the slowly proliferating astrocytes. The closely comparable results to the homogenous spheroids can be attributed to the highly metabolic and proliferative LBM1 and H16 cells, evident by their rapid spheroid formation in the absence of structural support. As a result, the BM cells outcompeted the astrocytes during spheroid formation, resulting in growth kinetics equivalent to that seen with the homogenous spheroids. Similar observations have been made with spheroids composed of glioblastoma cells and astrocytes[121], and pancreatic cancer cells and fibroblasts[122].

The spheroids composed of only astrocytes were also significantly smaller in comparison to spheroids of LBM1 and H16 cells. This demonstrated that the NHAs have a reduced ability to self-organize into three-dimensional structures without the additional support provided by methylcellulose. For future heterogenous spheroids using NHAs, compounds supporting cell aggregation such as methylcellulose or collagen, should be employed to obtain the maximal potential 3D growth of the NHA cells. Additionally, the required nutrients of NHA may have been absent from the DMEM-ALT culture medium used. Therefore, using an astrocyte-specific medium supplemented with growth factors known to enhance astrocyte growth may prove beneficial[123].

In conclusion, the addition of astrocytes to LBM1 and H16 cells did not enhance the growth of spheroids. Rather, their presence slightly slowed the growth of the heterogeneous spheroids, and astrocytes alone exhibited a limited ability to form three-dimensional structures, supporting the conclusion that their presence induced suboptimal growth when combined with BM cells.

5.5 Thioridazine Treatment Reduces Viability of BM Cells

The antipsychotic drug thioridazine has been previously tested in our group as a novel treatment for melanoma BM. The dopamine receptor antagonist proved strong cytotoxic effects on melanoma BM cell lines, while NHAs tolerated similar concentrations[58]. Since the drug can cross an intact BBB[124,125], and has shown anti-glioblastoma properties in a mouse xenograft model[125], it may be a promising adjuvant drug in the treatment of BM. Thus, in this thesis, the effect of thioridazine was studied on an additional melanoma BM cell line (H16), as well as a cell line generated from lung cancer BM (LBM1).

Viability assays on thioridazine-treated LBM1 and H16 cells exerted a potent cytotoxic effect, demonstrating that the IC_{50} doses for LBM1 and H16 cells were in the 10-11 µM range. This was consistent with the findings of Taule et al., who established IC_{50} doses ranging from 9-12 µM for several melanoma BM cell lines[58].

To conclude, further investigations are needed *in vitro*, especially testing on a wider range of lung cancer BM cell lines to firmly establish the efficacy of thioridazine on such tumour cells. Also, additional *in vivo* experiments are needed, to establish treatment efficacy, toxicity, and pharmacological and pharmacodynamic parameters to establish the drug as a potential adjuvant treatment in the clinical setting.

5.6 IHC Confirms Primary Diagnoses of BM Cell Lines

Lung cancer is a complex disease with a wide range of histologic subtypes and molecular variations. Thus, it is of vital importance to classify individual patients to determine suitable treatments and molecular-targeted therapies. IHC was done to potentially differentiate between cancerous and non-cancerous cells by identifying specific protein markers that are characteristic of the cancer type, as non-cancerous cells may be collected during BM resection. Moreover, primary tumours can express distinct immunohistological profiles compared to secondary lesions. Therefore, it is essential to establish the marker expression profile, particularly when variations are observed, as it can provide valuable insights into the treatment required for the secondary tumour.

The IHC results presented in **Fig. 4.9 a**, showed that the LBM1 cell line was of NSCLC origin, more specifically adenocarcinoma, which accounts for 85 % of all lung cancers[126],

from which 7-10 % of NSCLC patients present with BM at time of diagnosis[70]. The positive expression of CK7 confirmed that the cell line is a lung cancer BM cell line, as CK7 is a commonly used marker for the determination of the origin of metastatic cancer tissues[127]. The positive staining for TTF1, a highly specific marker for adenocarcinoma, conclusively confirmed the diagnosis. Although Napsin A, another adenocarcinoma marker, was negative in LBM1 cells, it is important to note that the presence of either marker (TTF1 or Napsin A) can strongly indicate adenocarcinoma. Along with this, the negative staining for CK5/6 and p63, markers for squamous cell NSCLC, in combination with the absence of the two neuroendocrine markers, synaptophysin and chromogranin A, further supported the diagnosis[126].

Melan-A, HMB45, S100 and SOX10 are all commonly used as markers of malignant melanoma. Therefore, the combination of negative Melan-A and HMB45, in addition to weakly expressed SOX10 and S100 (**Fig. 4.9 b**), was atypical in comparison to reported cases of melanoma[128]. As mentioned previously, primary tumours may exhibit a different immunohistological profile than the secondary lesion(s). Thus, loss of expression may be a possible explanation for the aberrant marker expression in the melanoma BM cells, as reported in a study by Agaimy et.al., where 13 cases of metastatic melanoma showed loss of S100, SOX10, Melan A, and HMB45 expression[129]. Agaimy et.al. described them with an undifferentiated status or in a process of "dedifferentiation". This phenomenon may complicate the process of correctly identifying the melanocytic lineage, or worse, result in an incorrect diagnosis. An alternative explanation is that melanocytic schwannoma, a rare soft-tissue tumour, is commonly misdiagnosed as melanoma[130].

In the case of breast cancer, IHC is used as a prognostic and treatment-response predictor. Estrogen and progesterone receptors, as well as HER2, are markers used for this verification. Based on the IHC results presented in **Fig. 4.9 c-d**, both BrBM1 and BrBM2 were classified as TNBC, as neither cell line expressed ER, PR, or HER2, which therefore limits the treatment options as they do not respond to a wide range of targeted therapies[131]. In comparison to other types of breast cancer, the survival time of TNBC patients is shorter, with 70 % of deaths occurring within 5 years of diagnosis[132]. Ck7 is expressed in the cytoplasm of the vast majority of TNBCs but is not typically used in the diagnosis of primary breast cancers unless secondary tumours are suspected[133]. Despite the lack of ER, PR and HER2 expression in the two breast cancer BM cell lines, the primary tumours may have

expressed one or multiple of these receptors, as loss of expression in metastatic neoplasms is more common than a gain of expression. This occurrence is associated with a decreased survival rate than those exhibiting concordance between the primary and metastatic tumours[134].

In conclusion, the marker expression profiles of the four BM cell lines were determined through IHC. With this information at hand, further characterisation of their *in vitro* behaviour can be done, including e.g., investigating the distribution of cell cycle phases using flow cytometry, as cancer cells are known to rapidly acquire genomic mutations in "checkpoint" genes that regulate the progression through the cell cycle[135]. Further characterisation may also include investigating their migratory and invasive properties using e.g., a scratch wound assay, or evaluating their apoptotic reaction in response to e.g., thioridazine treatment using western blotting. With this information available, the BM cell lines would be largely characterised by many fundamental behavioural properties, that collectively hold significant value for future studies.

5.7 The Tumourigenic Potential of LBM1 and H16 Cells *In Vivo*

To investigate whether lung- and melanoma-derived BM cells excised from patient biopsies would selectively metastasize to the brain in a mouse model system, the tumour cells were injected intracardially into four NOD-SCID mice each. To examine the metastatic progression following injection, T2W MR imaging was performed on weeks 2 and 4, showing that three of the four LBM1-injected mice display one tumour each at the four-week mark. This effectively indicated that LBM1 cells injected into NOD-SCID mice can potentially serve as an animal model for lung cancer BM research. However, due to the untimely unavailability of the MRI, scans at weeks 6 and 8 are required to conclusively investigate its future potential. Additionally, confirmation with IHC would provide more conclusive results by providing visualization of, and characterisation of specific proteins or markers within the tumour tissue.

Contrary, H16-injected mice displayed no signs of intracranial tumours but were nevertheless euthanized due to signs of discomfort and reduced mobility. This suggested that the extracranial tumours observed during autopsy, exerted a notable impact on their overall health, and further, intracranial tumours cannot be ruled out. Despite the lack of brain

tumours at week 4, this does not preclude H16 cells as a possible animal model for investigating tumourigenic potential of melanoma-derived BM cell lines. Therefore, a repetition of the *in vivo* experiment should include additional MRI scans at weeks 6 and 8, to potentially record the presence of brain tumours following injection into the bloodstream. Furthermore, bioluminescence can be employed to visualize colonisation and growth both in the brain and extracranial organs to better comprehend the tumour dynamics and behaviour beyond the confines of the brain, as previously done by Thorsen et.al[136]. Moreover, for the sake of convenience, it is advisable to exclude male mice from future experiments due to their tendency to behave aggressively towards one another, which can decrease the overall sample size and thus introduce bias to the results. The aggressiveness observed has previously been reported as a desire by the male mice to establish their own territories, from which the inferior animals are unable to escape, leading to stress, pain and even death[137].

5.8 Isolation of Exosomes from BM Cell Lines

Exosomes were successfully isolated from LBM1- and H16-derived conditioned culture medium. Differential centrifugation was the method of choice using an established and validated protocol from our lab, making it easy to compare and reproduce results across different cell lines. Immunoprecipitation may potentially produce a higher yield than differential centrifugation by using antibodies specific to exosomal surface markers, but the use of selected markers may limit the exosome population yielded. In addition to its higher cost, immunoprecipitation may be better suited for studies that require the separation of different subgroups of exosomes[138].

The fast and effective size-exclusion chromatography (SEC) may also be an alternative due to the high yield in combination with sample compatibility regarding high centrifugal forces related to differential centrifugation. However, differential centrifugation allows for the processing of larger volumes of culture medium, in addition to preventing loss of exosomes due to adherence to other particles present in the sample or inefficient elution of the exosomes from the SEC column. Similar observations were made in a study by Baranyai et.al., in which the exosomal yield was intentionally reduced to minimise contamination from albumin present in the blood plasma sample from which the exosomes were isolated[139].

Although differential centrifugation proved to be a straightforward and successful method, it is not without limitations related to the sedimentation rates of particles in the culture medium. As stated by Livshts et.al., differential centrifugation is an ideal method for isolating particles with substantial differences in sedimentation coefficients[140]. EVs however, exhibit only a slight difference in size, with exosomes typically ranging between 30-150 nm, and microvesicles ranging between 0,1-1 μm[98]. Consequently, it may be challenging to extract pure exosomes due to the likelihood of other similarly sized particles being deposited simultaneously. However, the isolated particles in this study were indeed exosomes (**Figure 4.11.1**), as confirmed by their average size and morphological characteristics provided by DLS and TEM.

The irregular and rough surface visible on some of the exosomes (**Fig. 4.11.1)**, is likely due to the presence of transmembrane proteins such as tetraspanins, integrins or MHC proteins. The cup-shaped morphology typically seen with TEM, is a result of the fixing and dehydration of the exosomes prior to imaging. Thus, the exosomes were not imaged in their native spherical state[141]. However, TEM analysis confirmed that the isolation technique utilised, successfully isolated exosomes within the expected size range and morphology. In future studies in our group, the exosomes will be labelled with dextran-coated SPIONs to serve as a contrast agent for MRI to investigate their biodistribution *in vivo*, as previously done by Hu et.al.[142].

As reported by Lyu et.al., DLS may potentially overestimate the size of the exosomes. DLS measures transient fluctuations in the intensity of the scattered light, which is affected by the Brownian motion of the particles in the sample. If the exosomes form larger structures by aggregating, this Brownian motion is slowed down, distorting the signal output[143]. This may cause a substantial increase in the measured size, as the DLS is unable to differentiate between single exosomes and aggregates, which can therefore result in a flawed output that overestimates the size of the exosomes, as suggested in **Table 4.11**. It is, however, possible to differentiate aggregates from single exosomes using TEM, so the true size of the exosomes was confirmed by the images in **Fig. 4.11.1**. Although the observed sizes of the exosomes presented in **Fig. 4.11.3 a-b** were slightly larger than the expected range of 30-150 nm, it is important to note that the sizes of exosomes can vary due to size heterogeneity within a sample, which may also contribute to variability in size measurements across the isolated exosome batches. Therefore, the observed sizes were still considered acceptable within the

context of the study and did not significantly impact the overall conclusions drawn from the results previously presented.

5.9 Inconclusive Electroporation of Exosomes

While tracking of exosomes is currently a highly researched topic, the imaging aspect exhibits some limitations. Labelling exosomes with fluorescent dyes for fluorescent imaging is highly sensitive, but deep tissue penetration and aggregation of the exosomes induced by the labelling dyes confines its potential[144]. Alternatively, positron emission tomography (PET) is a sensitive modality, but the long-term tracking ability is limited by the short half-life of radioactive tracers[145]. Therefore, SPIONs provide an alternative regarding the reproducible preparations using electroporation for spontaneous pore formation in exosomes, and long-term tracking ability. With SPIONs, exosomes can be visualized *in vitro* and *in vivo* by for example MRI[146,147]. The iron oxide core of SPIONs has a high magnetic susceptibility causing a local magnetic field gradient, which decreases the T2 relaxation time in adjacent tissue[148]. This enhances the contrast of T2W MR images and allows for the visualisation of e.g., exosomes or cells.

With its easily reproducible approach and fast processing time, electroporation may provide a straightforward and efficient means for labelling exosomes. However, the high voltage may cause them to aggregate or burst, altering the morphology and integrity of the exosomes, as described by Sancho-Albero et.al.[149]. Therefore, a trehalose buffer was used for two of the conditions (**Table 3.18**), as Hood et.al., revealed its protective abilities when electroporating exosomes with 5 nm SPIONs[150]. The results presented in **Fig. 4.12.1** and **Fig. 4.12.2** are in accordance with the findings by Hood et.al., as some aggregation was seen with the exosomes electroporated with the sucrose buffer in comparison to those electroporated with the trehalose buffer, where there was minimal exosome aggregation, and their morphology was well-preserved. To demonstrate the need for electroporation, a control group of exosomes incubated with the SPIONs was included in the study.

The results from the electroporation of exosomes are inconclusive, as electroporated exosomes should appear darker than non-electroporated exosomes when viewed with TEM. The iron oxide particles absorb more electrons than the exosome membrane, resulting in a darker appearance. It was, therefore, challenging to accurately determine the effectiveness of

the electroporation of the exosomes depicted in **Fig. 4.12.1** and **Fig. 4.12.2**, as the darkening can vary by several factors such as variations in lighting conditions, image quality, and potential overlapping colours in the samples. These factors introduced ambiguity and made it challenging to draw definitive conclusions regarding the efficacy of the electroporation. To provide definitive confirmation of the observations, future experiments should include a quantitative analysis, such as spectrophotometry, to measure the absorbance of the iron oxide particles at a specific wavelength before and after electroporation. This would provide an objective and accurate method to quantify the incorporation of the iron oxide particles, as opposed to relying on a subjective visual evaluation of their darkness using TEM. Due to time limitations, these experiments were not performed in this thesis.

5.10 SPION Coating Affects Cellular Uptake

After the inconclusive results yielded from electroporation of LBM1-derived exosomes with carboxyl-coated SPIONs, the ability of the LBM1 cells to uptake the same particles was assessed by incubating them with the cells for 24 and 48 h with varying concentrations. This was followed by Prussian blue staining to examine the cellular localization and distribution of the particles. However, as depicted in **Fig. 4.13.1**, the iron oxide particles were not internalised by the cells, as no staining was observed. Consequently, this finding suggested that the exosomes that were electroporated also failed to internalise the particles. Considering this, a qualitative assessment of the electroporation by utilizing e.g., mass spectrometry, would yield conclusive results at an earlier stage.

The unsuccessful attempt to induce cellular uptake of the SPIONs may be attributed to the composition of the particle surface coating. The carboxyl-coated SPIONs used may not be compatible with the membrane of the LBM1 cells, consequently resulting in ineffective uptake by the exosomes. The compatibility of the SPIONs with the cells depends both on the size and surface chemistry of the nanoparticles. The SPIONs used were 5 nm in size, and the carboxyl-coated SPIONs were negatively charged. This specific coating may not be compatible with the LBM1 cells, since cancer cells in general are known to possess a negatively charged cell membrane due to lactate secretion in relation to increased glycolysis, one of the cancer hallmarks[151]. SPIONs with a different surface coating such as e.g., polysaccharides like dextran, which is currently in commercial use as MRI contrast agents, may provide improved stability[152].

Based on this, dextran-coated SPIONs were used, with the expectation that they would be internalised by the LBM1 cells. As seen in **Fig. 4.13.2**, the dextran-coated SPIONs were indeed internalised by the LBM1 cells following 24- and 48-h incubation and staining with Prussian blue. This unequivocally confirms that LBM1 cells were not able to internalise the carboxyl-coated SPIONs, as the same protocol was followed in the second attempt using the dextran-coated SPIONs. As shown in the graph in **Fig. 4.13.3**, concentrations as low as 2,5 μg/mL displayed labelling in close to 100 % of the cells both when incubated for 24 and 48 h. Nevertheless, 10 μg/mL displayed the most satisfactory results and will be used in subsequent experiments using LBM1 cells. Furthermore, the number of stained cells did not significantly vary between the samples incubated for 24 and 48 h. Therefore, for time-saving purposes and to minimise potential cellular toxicity, a 24 h incubation period will be utilised in subsequent experiments. As illustrated by **Fig. 4.13.4**, there was no statistical difference in the number of cells between those labelled with SPIONs and the controls, with the exception of those incubated with 30 μg/mL for 48 h. Thus, as SPIONs may induce accumulation of ROS in response to digestion of their coating, thus exposure to iron oxide[153], a more comprehensive evaluation of these SPIONs should be included in future experiments. By measuring the viability of the cells following addition of the nanoparticles at varying concentrations, the toxicity of the SPIONs can be measured more accurately, and a maximum concentration yielding the greatest uptake can be determined. This has previously been done by Sunstrøm et.al., who demonstrated that a range of melanoma BM cells did not display any changes in viability with increasing SPION concentrations up to 15 μg/mL[154]. It is, however, worth noting that according to the literature, higher labelling concentrations are often used, such as in the article by Sibson et.al[155].

References:

1. Weinberg RA. How Cancer Arises. *Scientific Amierican*. 1996;275(3):62-70. doi:https://www.jstor.org/stable/24993349
2. Colditz GA, Wolin KY, Gehlert S. Applying What We Know to Accelerate Cancer Prevention. *Science Translational Medicine*. 2012;4(127):1-10. doi:10.1126/scitranslmed.3003218
3. Costello LC, Franklin RB. The genetic/metabolic transformation concept of carcinogenesis. *Cancer Metastasis*. 2012;31(0):123-130. doi:10.1007/s10555-011-9334-8
4. Vogelstein B, Kinzler KW. Cancer genes and the pathways they control. *Nature Medicine*. 2004;10(8):789-799.
5. Hanahan D, Weinberg RA. Hallmarks of Cancer: The Next Generation. *Cell*. 2011;144(5)doi:10.1016/j.cell.2011.02.013
6. Zhou L, Zhang Z, Huang Z, Nice E, Zou B, Huang C. Revisiting cancer hallmarks: insights from the interplay between oxidative stress and non-coding RNAs. *Molecular Biomedicine*. 2020;1(4):1-24. doi:10.1186/s43556-020-00004-1
7. Feitelson MA, Arzumanyan A, Kulathinal RJ, et al. Sustained proliferation in cancer: mechanisms and novel therapeutic targets. *Seminars in Cancer Biology*. 2016;35:25-54. doi:10.1016/j.semcancer.2015.02.006
8. Amin ARMR, Karpowicz PA, Carey TE, et al. Evasion of anti-growth signaling: A key step in tumorigenesis and potential target for treatment and prophylaxis by natural compounds. *Seminars in Cancer Biology*. 2015;35:55-77. doi:10.1016/j.semcancer.2015.02.005
9. Safa AR. Resistance to Cell Death and Its Modulation in Cancer Stem Cells. *Critical Reviews in Oncogenesis*. 2016;21(3-4):203-219. doi:10.1615/CritRevOncog.2016016976
10. Sjöström J, Bergh J. How apoptosis is regulated, and what goes wrong in cancer. *British Medical Journal*. 2001;322(7301):1538-1539. doi:10.1136/bmj.322.7301.1538
11. Skommer J, Brittain T, Raychaudhuri S. Bcl-2 inhibits apoptosis by increasing the time-to-death and intrinsic cell-to-cell variations in the mitochondrial pathway of cell death. *Apoptosis*. 2010;15:1223-1233. doi:10.1007/s10495-010-0515-7
12. Wright WE, Shay JW. Time, telomeres and tumours: is cellular senescence more than an anticancer mechanism? *Trends in Cell Biology*. 1995;5(8):293-297. doi:10.1016/s0962-8924(00)89044-3
13. Yaswena P, MacKenzie KL, Keithc WN, et al. Therapeutic targeting of replicative immortality. *Seminars in Cancer Biology*. 2015;35:104-128. doi:10.1016/j.semcancer.2015.03.007
14. Saman H, Raza SS, Uddin S, Rasul K. Inducing Angiogenesis, a Key Step in Cancer Vascularization, and Treatment Approaches. *Cancers*. 2020;12(5)doi:10.3390/cancers12051172
15. Fares J, Fares MY, Khachfe HH, Salhab HA, Fares Y. Molecular principles of metastasis: a hallmark of cancer revisited. *Signal Transduction and Targeted Therapy*. 2020;5(28)doi:10.1038/s41392-020-0134-x
16. Neagu M, Constantin C, Popescu ID, et al. Inflammation and Metabolism in Cancer Cell—Mitochondria Key Player. *Frontiers Oncology*. 2019;9(348)doi:10.3389/fonc.2019.00348
17. Beatty GL, Gladney WL. Immune escape mechanisms as a guide for cancer immunotherapy. *Clinical Cancer Research*. 2015;15(4):687-692. doi:10.1158/1078-0432.CCR-14-1860
18. Hanahan D, Weinberg RA. The Hallmarks of Cancer. *Cell*. 2000;100(1):50-70.
19. Ghosal G, Chen J. DNA damage tolerance: a double-edged sword guarding the genome. *Transl Cancer Res*. 2013;2(3):107-129. doi:10.3978/j.issn.2218-676X.2013.04.01

20. Marei HE, Althani A, Afifi N, et al. p53 signaling in cancer progression and therapy. *Cancer Cell International*. 2021;21(703)doi:10.1186/s12935-021-02396-8
21. Vogelstein B, Lane D, Levine AJ. Surfing the p53 network. *Nature*. 2000;408(6810):307-310. doi:10.1038/35042675
22. Greten FR, Grivennikov SI. Inflammation and Cancer: Triggers, Mechanisms, and Consequences. *Immunnity*. 2019;51(1):27-41.
23. Shacter E, Weitzman SA. Chronic inflammation and cancer. *Oncology Reports*. 2002;16(2):217-226.
24. Varmus H. The New Era in Cancer Research. *American Association for the Advancement of Science*. 2006;312(5777):1162-1165.
25. Jiang WG, Mansel RE. *Metastatic cascade, molecular/cellulsar events and new therapeutic opportunities. Cancer Metastasis — Biology and Treatment*. Springer; 2000. Accessed 03.02.23.
26. Dujon AM, Capp J-P, Brown JS, et al. Is There One Key Step in the Metastatic Cascade? *Cancers*. 2021;13(15)doi:10.3390/cancers13153693
27. Bhutta BS, Alghoula F, Berim I. *Hypoxia*. StatPearls Publishing; 2022.
28. Tameemi WA, Dale TP, Al-Jumaily RMK, Forsyth NR. Hypoxia-modified cancer cell metabolism. *Frontiers in Cell and Developmental Biology*. 2019;7(4)doi:10.3389/fcell.2019.00004
29. Eslami-S Z, Cortés-Hernández LE, Alix-Panabières C. The Metastatic Cascade as the Basis for Liquid Biopsy Development. *Frontiers in Oncology*. 2020;10(1055)doi:10.3389/fonc.2020.01055
30. Wirtz D, Konstantopoulos K, Searson PC. The physics of cancer: the role of physical interactions and mechanical forces in metastasis. *Nature Reviews Cancer*. 2011;11(7):512-522. doi:10.1038/nrc3080
31. Fidler IJ. Metastasis: Quantitative Analysis of Distribution and Fate of Tumor Emboli Labeled With 125I-5-Iodo-2′ -deoxyuridine. *JNCI: Journal of the National Cancer Institute*. 1970;45(4):773-782. doi:10.1093/jnci/45.4.773
32. Aceto N, Bardia A, Miyamoto DT, et al. Circulating Tumor Cell Clusters Are Oligoclonal Precursors of Breast Cancer Metastasis. *Cell*. 2014;158:1110-1122. doi:10.1016/j.cell.2014.07.013
33. Schillaci O, Fontana S, Monteleone F, et al. Exosomes from metastatic cancer cells transfer amoeboid phenotype to non-metastatic cells and increase endothelial permeability: their emerging role in tumor heterogeneity. *Scientific Reports*. 2017;7(1):1-15. doi:10.1038/s41598-017-05002-y
34. McGranahan N, Rosenthal R, Hiley CT. Allele-Specific HLA Loss and Immune Escape in Lung Cancer Evolution. *Cell*. 2017;171(6):1259-1271. doi:10.1016/j.cell.2017.10.001
35. Kitamura T, Qian B-Z, Pollard JW. Immune cell promotion of metastasis. *Nature Reviews Immunology*. 2015;15(2):73-86. doi:10.1038/nri3789
36. Doglioni G, Parik S, Fendt S-M. Interactions in the (Pre)metastatic Niche Support Metastasis Formation. *Frontiers in Oncology*. 2019;9doi:10.3389/fonc.2019.00219
37. Wong J, Hird A, Kirou–Mauro A, BSc JN, MBBS EC. Quality of life in brain metastases radiation trials: a literature review. *Current Oncology*. 2008;15(5):25-45.
38. Soffietti R, Abacioglu U, Baumert B, et al. Diagnosis and treatment of brain metastases from solid tumors: guidelines from the European Association of Neuro-Oncology (EANO). *Neuro-Oncology*. 2017;19(2):162-174. doi:10.1093/neuonc/now241
39. Nussbaum ES, Djalilian HR, Cho KH, Hall WA. Brain metastases: Histology, multiplicity, surgery, and survival. *Cancer: Interdisciplinary International Journal of the American Cancer Society*. 1996;78(8):1781-1788.

40. Parsons MW, Peters KB, Floyd SR, Brown P, Wefel JS. Preservation of neurocognitive function in the treatment of brain metastases. *Neuro-Oncology Advances*. 2021;3(5):96-107. doi:10.1093/noajnl/vdab122
41. Liu Z, Lei B, Zheng M, Li Z, Huang S, Deng Y. Prognostic factors in patients treated with surgery for brain metastases: A single-center retrospective analysis of 125 patients. *International Journal of Surgery*. 2017;44:204-209. doi:10.1016/j.ijsu.2017.05.033
42. Nieder C, Haukland E, Mannsåker B, Pawinski AR, Yobuta R, Dalhaug A. Presence of Brain Metastases at Initial Diagnosis of Cancer: Patient Characteristics and Outcome. *Cureus*. 2019;11(2):1-7. doi:10.7759/cureus.4113
43. Patchell RA. The management of brain metastases. *Cancer Treatment Reviews*. 2003;29:533-540. doi:10.1016/S0305-7372(03)00105-1
44. Chow E, Fan G, Hadi S, Wong J, Kirou-Mauro A, Filipczak L. Symptom Clusters in Cancer Patients with Brain Metastases. *Clinical Oncology*. 2008;20:76-82. doi:10.1016/j.clon.2007.09.007
45. Wong J, Hird A, Zhang L, et al. Symptoms and Quality of Life in Cancer Patients With Brain Metastases Following Palliative Radiotherapy. *International Journal of Radiation Oncology, Biology & Physics*. 2009;75(4):1125-1131. doi:10.1016/j.ijrobp.2008.12.013
46. Arnold SM, Patchell RA. Diagnosis and Management of Brain Metastases. *Neuro-Oncology*. 2001;15(6):1085-1107. doi:10.1016/S0889-8588(05)70269-0
47. Fink KR, Fink JR. Imaging of brain metastases. *Neuro-Oncology*. 2013;4(4):209-220.
48. Akshulakov SK, Kerimbayev TT, Biryuchkov MY, Urunbayev YA, Farhadi DS, Byvaltsev VA. Current Trends for Improving Safety of Stereotactic Brain Biopsies: Advanced Optical Methods for Vessel Avoidance and Tumor Detection. *Frontiers in Oncology*. 2019;9(947):1-9. doi:10.3389/fonc.2019.00947
49. Bekaert L, Emery E, Levallet G, Lechapt-Zalcman E. Histopathologic diagnosis of brain metastases: current trends in management and future considerations. *Brain Tumor Pathology*. 2017;34:8-19. doi:10.1007/s10014-016-0275-3
50. McTyre E, Scott J, Chinnaiyan P. Whole brain radiotherapy for brain metastasis. *Neuro-Oncology*. 2013;4(4):236-245. doi:10.4103/2152-7806.111301
51. Scaringi C, Agolli L, Minniti G. Technical Advances in Radiation Therapy for Brain Tumors. *Anticancer Research*. 2018;38(11):6041-6045. doi:10.21873/anticanres.12954
52. Bent MJvd. The role of chemotherapy in brain metastases. *European Journal of Cancer*. 2003;39(15):2114-2120. doi:10.1016/S0959-8049(03)00577-X
53. Ryken TC, Kuo JS, Prabhu RS, Sherman JH, Kalkanis SN, Olson JJ. Congress of neurological surgeons systematic review and 3 evidence-based guideline on the role of steroids in the treatment 4 of adults with metastatic brain tumors. *Neurosurgery*. 2019;84(3)doi:10.1093/neuros/nyy546
54. Nieblas-Bedolla E, Nayyar N, Singh M, Sullivan RJ, Brastianos PK. Emerging Immunotherapies in the Treatment of Brain Metastases. *The Oncologist*. 2021;26(3):231-241. doi:10.1002/onco.13575
55. Bindal AK, Bindal RK, Hess KR, et al. Surgery versus radiosurgery in the treatment of brain metastasis. *Journal of Neurosurgery*. 1996;84:748-754. doi:10.3171/jns.1996.84.5.0748
56. Bhangoo SS, Linskey ME, Kalkanis SN. Evidence-Based Guidelines for the Management of Brain Metastases. *Neurosurgery Clinics of North America*. 2011;22(1):97-104. doi:10.1016/j.nec.2010.09.001
57. Mut M. Surgical treatment of brain metastasis: A review. *Clinical Neurology and Neurosurgery*. 2012;114(1):1-8. doi:10.1016/j.clineuro.2011.10.013

58. Taule EM, Wikerholmen T, E Rigg KS, Wang J, Thorsen F. A Repurposing thioridazine as a novel treatment of melanoma brain metastasis. *Neuro-Oncology*. 2022;24(2):52. doi:10.1093/neuonc/noac174.181
59. Mitra D, Chen Y-H, Li R, et al. EGFR mutant locally advanced non-small cell lung cancer is at increased risk of brain metastasis. *Clinical and Translational Radiation Oncology*. 2018;18:32-38. doi:10.1016/j.ctro.2019.06.008
60. Garcia-Alvarez A, Papakonstantinou A, Oliveira M. Brain Metastases in HER2-Positive Breast Cancer: Current and Novel Treatment Strategies. *Cancers*. 2021;12(2927)doi:10.3390/
61. Yuan J, Cheng Z, Feng J, et al. Prognosis of lung cancer with simple brain metastasis patients and establishment of survival prediction models: a study based on real events. *BMC Pulm Med*. 2022;22(162)doi:10.1186/s12890-022-01936-w
62. Ramakrishna R, Rostomily R. Seed, soil, and beyond: The basic biology of brain metastasis. *Surcigal Neurology International*. 2013;4(2)(4):256-264. doi:10.4103/2152-7806.111303
63. Weiss L. Comments on hematogenous metastatic patterns in humans as revealed by autopsy. *Clinical and Experimental Metastasis*. 1992;10(3):191-199.
64. Davis FG, Dolecek TA, McCarthy BJ, Villano JL. Toward determining the lifetime occurrence of metastatic brain tumors estimated from 2007 United States cancer incidence data. *Neuro-Oncology*. 2012;14(9):1171-1177. doi:10.1093/neuonc/nos152
65. Barnholtz-Sloan JS, Sloan AE, Davis FG, Vigneau FD, Lai P, Sawaya RE. Incidence Proportions of Brain Metastases in Patients Diagnosed (1973 to 2001) in the Metropolitan Detroit Cancer Surveillance System. *Journal of Clinical Oncology*. 2004;22(14):2865-2872. doi:10.1200/JCO.2004.12.149
66. Butowski NA. Epidemiology and Diagnosis of Brain Tumors. *American Academy of Neurology*. 2015;21(2):301-313.
67. Sleemana J, Steegc PS. Cancer metastasis as a therapeutic target. *Eur J Cancer*. 2010;46(7):1177-1180. doi:10.1016/j.ejca.2010.02.039
68. Mehlen P, Puisieux A. Metastasis: a question of life or death. *Nat Rev Cancer*. 2006;6:449-458. doi:10.1038/nrc1886
69. YAMANAKA R. Medical management of brain metastases from lung cancer. *Oncology Reports*. 2009;22:1269-1276. doi:10.3892/or_00000564
70. mbbs AA, Goffin JR, Arnold A, Ellis PM. Survival of patients with non-small-cell lung cancer after a diagnosis of brain metastases. *Current oncology*. 2013;20(4):300-306. doi:10.3747/co.20.1481
71. Patchell RA, Tibbs PA, Walsh JW, et al. A Randomized Trial of Surgery in the Treatment of Single Metastases to the Brain. *The New England Journal of Medicine*. 1990;322(8):494—500.
72. Wilson TG, Winter H, Taylor H, Herbert C. Treating brain metastases in melanoma: What is the optimal CNS-directed and systemic management? *Journal of Radiosurgery and SBRT*. 2021;7(4):279-285.
73. Damsky WE, Rosenbaum LE, Bosenberg M. Decoding Melanoma Metastasis. *Cancers*. 2011;3(1):126-163. doi:10.3390/cancers3010126
74. Fidler IJ, Schackert G, Zhang R-d, Radinsky R, Fujimaki T. The biology of melanoma brain metastasis. *Cancer and Metastasis Reviews*. 1999;18(3):387-400.
75. Lin NU, Bellon JR, Winer EP. CNS Metastases in Breast Cancer. *Journal of Clinical Oncology*. 2004;22(17):3608-3617. doi:10.1200/JCO.2004.01.175
76. Reis-Filho JS, Pusztai L. Gene expression profiling in breast cancer: classification, prognostication, and prediction. *The Lancet*. 2011;378(9805):1812-1823.

77. Sperduto PW, Kased N, Roberge D, et al. The effect of tumor subtype on the time from primary diagnosis to development of brain metastases and survival in patients with breast cancer. *Journal of Neuro-Oncology*. 2013;(112):467-472. doi:10.1007/s11060-013-1083-9
78. Guo S, Deng C-X. Effect of Stromal Cells in Tumor Microenvironment on Metastasis Initiation. *International Journal of Biological Scienes*. 2018;14(14):2083-2093. doi:10.7150/ijbs.25720
79. Hida K, Maishi N, Torii C, Hida Y. Tumor angiogenesis—characteristics of tumor endothelial cells. *International Journal of Clinical Oncology*. 2016;21:206-2012. doi:10.1007/s10147-016-0957-1
80. Albini A, Sporn MB. The tumour microenvironment as a target for chemoprevention. *Nature Reviews Cancer*. 2007;7:139-147. doi:10.1038/nrc2067
81. Lorger M. Tumor Microenvironment in the Brain. *Cancers*. 2012;4(1):218-243. doi:10.3390/cancers4010218
82. Rossum Dv, Hanisch U-K. Microglia. *Metabolic Brain Disease*. 2004;19(3):393-411.
83. Jessen KR. Glial cells. *The International Journal of Biochemistry & cell Biology*. 2004;36:1861-1867. doi:10.1016/j.biocel.2004.02.023
84. Poitelon Y, Kopec AM, Belin S. Myelin Fat Facts: An Overview of Lipids and Fatty Acid Metabolism. *Cells*. 2020;9(4)doi:10.3390/cells9040812
85. Abbott NJ, Patabendige AAK, Dolman DEM, Yusof SR, Begley DJ. Structure and function of the blood–brain barrier. *Neuobiology of Disease*. 2010;37(1):13-25. doi:10.1016/j.nbd.2009.07.030
86. Serlin Y, Shelef I, Knyazer B, Friedman A. Anatomy and Physiology of the Blood-Brain Barrier. *Seminars in Cell Developmental Biology*. 2015;38:2-6.
87. Daneman R. The Blood–Brain Barrier in Health and Disease. *Annals of neurology*. 2012;72(5):648-672. doi:10.1002/ana.23648
88. Alahmari A. Blood-Brain Barrier Overview: Structural and Functional Correlation. *Neural Plasticity*. 2021:1-10. doi:10.1155/2021/6564585
89. Noda M. The Brain Microenvironment. *Central Nervous System Metastasis, the Biological Basis and Clinical Considerations Cancer Metastasis - Biology and Treatment*. Springer Science; 2012:43-54:chap 3.
90. Placone AL, Quiñones-Hinojosa A, Searson PC. The role of astrocytes in the progression of brain cancer: complicating the picture of the tumor microenvironment. *Tumor Biology*. 2016;37(1):61-69. doi:10.1007/s13277-015-4242-0
91. Samdani AF, Kuchner EB, Rhines L, et al. Astroglia Induce Cytotoxic Effects on Brain Tumors via a Nitric Oxide-Dependent Pathway Both in Vitro and in Vivo. *Neuosurgery*. 2004;54(5):1231-1238. doi:10.1227/01.NEU.0000119576.76193.B8
92. Srinivasan ES, Deshpande K, Neman J, Winkler F, Khasraw M. The microenvironment of brain metastases from solid tumors. *Neuro-Oncology Advances*. 2021;3(5):121-132. doi:10.1093/noajnl/vdab121
93. Chen Q, Boire A, Jin X, et al. Carcinoma–astrocyte gap junctions promote brain metastasis by cGAMP transfer. *Nature*. 2016;533:493-498. doi:10.1038/nature18268
94. Seano G, Nia HT, Emblem KE, et al. Solid stress in brain tumours causes neuronal loss and neurological dysfunction and can be reversed by lithium. *Nat Biomed Eng*. 2019;3(3):230-245. doi:10.1038/s41551-018-0334-7
95. Nemana J, Terminib J, Wilczynskic S, et al. Human breast cancer metastases to the brain display GABAergic properties in the neural niche. *Proc Natl Acad Sci USA*. 2014;111(3):984-989. doi:10.1073/pnas.1322098111
96. Zeng Q, Michael IP, Zhang P, et al. Synaptic proximity enables NMDAR signalling to promote brain metastasis. *Nature*. 2019;573:526-531. doi:10.1038/s41586-019-1576-6

97. Gurung S, Perocheau D, Touramanidou L, Baruteau J. The exosome journey: from biogenesis to uptake and intracellular signalling. *Cell Communication and Signaling*. 2021;19(1):1-19. doi:10.1186/s12964-021-00730-1
98. Ståhl A-l, Johansson K, Mossberg M, Kahn R, Karpman D. Exosomes and microvesicles in normal physiology, pathophysiology, and renal diseases. *34*. 2019;(1):11-30. doi:10.1007/s00467-017-3816-z
99. Tai Y-L, Chen K-C, Hsieh J-T, Shen T-L. Exosomes in cancer development and clinical applications. *Cancer Science*. 2018;109(8):2364-2374. doi:10.1111/cas.13697
100. Mashouri L, Yousefi H, Aref AR, Ahadi Am, Molaei F, Alahari SK. Exosomes: composition, biogenesis, and mechanisms in cancer metastasis and drug resistance. *Molecular Cancer*. 2019;18(75)doi:10.1186/s12943-019-0991-5
101. Hessvik NP, Llorente A. Current knowledge on exosome biogenesis and release. *Cellular and Molecular Life Sciences*. 2018;75:193-208. doi:10.1007/s00018-017-2595-9
102. Meng X, Pan J, Sun S, Gong Z. Circulating exosomes and their cargos in blood as novel biomarkers for cancer. *Translational Cancer Research*. 2018;7(2):227-244.
103. Zhou W, Fong MY, Min Y, et al. Cancer-secreted miR-105 destroys vascular endothelial barriers to promote metastasis. *Cancer Cell*. 2014;25(4):501-515. doi:10.1016/j.ccr.2014.03.007
104. Rundhaug JE. Matrix Metalloproteinases, Angiogenesis, and Cancer:. *Clinical Cancer Research*. 2003;9(2):551-554.
105. Li I, Nabet BY. Exosomes in the tumor microenvironment as mediators of cancer therapy resistance. *Molecular Cancer*. 2019;18(32):1-10. doi:10.1186/s12943-019-0975-5
106. Schindelin J, Arganda-Carreras I, Frise E, et al. Fiji: an open-source platform for biological-image analysis. *Nature methods*. 2012;9(7):676-682. doi:10.1038/nmeth.2019
107. al. CTe. Minimal information for studies of extracellular vesicles 2018 (MISEV2018): a position statement of the International Society for Extracellular Vesicles and update of the MISEV2014 guidelines. *Journal of Extracellular Vesicles*. 2018;7(1)doi:10.1080/20013078.2018.1535750
108. Lassman AB, DeAngelis LM. Brain metastases. *Neurologic Clinics of North Amierica*. 2003;21(1):1-23. doi:10.1016/S0733-8619(02)00035-X
109. Burg BvV, Rutteman GR, Blankenstein MA, Laat SWD, Zoelen EJJv. Mitogenic Stimulation of Human Breast Cancer Cells in a Growth Factor-Defined Medium: Synergistic Action of Insulin and Estrogen. *Journal of Cellular Physiology*. 1988;132:101-108. doi:10.1002/jcp.1041340112
110. Cao J, Wu X, Qin X, Li Z. Uncovering the Effect of Passage Number on HT29 Cell Line Based on the Cell Metabolomic Approach. *Journal of Proteome Research*. 2021;20(3):1582-1590. doi:10.1021/acs.jproteome.0c00806
111. Kwist K, Bridges WC, Burg KJL. The effect of cell passage number on osteogenic and adipogenic characteristics of D1 cells. *Cytotechnology*. 2016;68:1661-1667. doi:10.1007/s10616-015-9883-8
112. Barkla DH, Allen BJ, Brown JK, Mountford M, Mishima Y, Ichihashi M. Morphological Changes in Human Melanoma Cells Following Irradiation With Thermal Neutrons. *Pigment Cell Research*. 1989;2(4):345-348.
113. Kenny PA, Lee GY, Myers CA, et al. The morphologies of breast cancer cell lines in three-dimensional assays correlate with their profiles of gene expression. *Molecular Oncology*. 2007;1(1):84-96. doi:10.1016/j.molonc.2007.02.004
114. Singh SK, Abbas S, Saxena AK, Tiwari S, Sharma LK, Tiwari M. Critical role of three-dimensional tumorsphere size on experimental outcome. *Biotechnologies*. 2020;69(5)doi:10.2144/btn-2020-0081

115. Browning AP, Sharp JA, Murphy RJ, et al. Quantitative analysis of tumour spheroid structure. *eLife*. 2021;10doi:10.7554/eLife.73020
116. Han SJ, Kwon S, Kim KS. Challenges of applying multicellular tumor spheroids in preclinical phase. *Cancer Cell International*. 2021;21(152)doi:10.1186/s12935-021-01853-8
117. Friedrich J, Seidel C, Ebner R, Kunz-Schughart LA. Spheroid-based drug screen: considerations and practical approach. *Nature Protocols*. 2009;4(3)doi:10.1038/nprot.2008.226
118. Rozenberg JM, Filkov GI, Trofimenko AV, et al. Biomedical Applications of Non-Small Cell Lung Cancer Spheroids. *Front Oncology*. 2021;11doi:10.3389/fonc.2021.791069
119. Feodoroffa M, Mikkonen P, Turunen L, et al. Comparison of two supporting matrices for patient-derived cancer cells in
3D drug sensitivity and resistance testing assay (3D-DSRT). *SLAS Discovery*. 2023;doi:10.1016/j.slasd.2023.03.002
120. Shuford S, ChristineWilhelm, Rayner M, et al. Prospective Validation of an Ex Vivo, Patient-Derived 3D Spheroid Model for Response Predictions in Newly Diagnosed Ovarian Cancer. *Scientific Reports*. 2019;9(1):1-13. doi:10.1038/s41598-019-47578-7
121. Nakod PS, Kim Y, Rao SS. The Impact of Astrocytes and Endothelial Cells on Glioblastoma Stemness Marker Expression in Multicellular Spheroids. *Cellular and Molecular Bioengineering*. 2021;14(6):639-651. doi:10.1007/s12195-021-00691-y
122. Lazzari G, Nicolas V, Matsusaki M, Akashi M, Couvreur P, Mura S. Multicellular spheroid based on a triple co-culture: A novel 3D model to mimic pancreatic tumor complexity. *Acta Biomaterialia*. 2018;78:296-307. doi:10.1016/j.actbio.2018.08.008
123. Morrison RS, Vellis JD. Growth of purified astrocytes in a chemically defined medium. *Proceedings of the National Academy of Sciences*. 1981;78(11):7205-7209.
124. Chu C-W, Ko H-J, Chou C-H, et al. Thioridazine Enhances P62-Mediated Autophagy and Apoptosis Through Wnt/β-Catenin Signaling Pathway in Glioma Cells. *International Journal of Molecular Sciences*. 2019;20(473)doi:10.3390/ijms20030473
125. Cheng H-W, Liang Y-H, Kuo Y-L, et al. Identification of thioridazine, an antipsychotic drug, as an antiglioblastoma and anticancer stem cell agent using public gene expression data. *Cell Death & Disease*. 2015;6 doi:10.1038/cddis.2015.77
126. Inamura K. Update on Immunohistochemistry for the Diagnosis of Lung Cancer. *Cancers (Basel)*. 2018;10(3)doi:10.3390/cancers10030072
127. Dum D, Menz A, Volkel C, et al. Cytokeratin 7 and cytokeratin 20 expression in cancer: A tissue microarray study on 15,424 cancers. *Experimental and Molecular Pathology*. 2022;126doi:10.1016/j.yexmp.2022.104762
128. Saliba E, Bhawan J. Aberrant Expression of Immunohistochemical Markers in Malignant Melanoma: A Review. *Dermatopathology*. 2021;8:359-370. doi:10.3390/dermatopathology8030040
129. Agaimy A, Specht K, Stoehr R, et al. Metastatic Malignant Melanoma With Complete Loss of Differentiation Markers (Undifferentiated/Dedifferentiated Melanoma): Analysis of 14 Patients Emphasizing Phenotypic Plasticity and the Value of Molecular Testing as Surrogate Diagnostic Marker. *The American Journal of Surgical Pathology*. 2016;40(2):181-191. doi:10.1097/PAS.0000000000000527.
130. Kaehler KC, Russo PAJ, Katenkamp D, et al. Melanocytic schwannoma of the cutaneous and subcutaneous tissues: three cases and a review of the literature. *Melanoma Research*. 2008;18(6):438-442. doi:10.1097/CMR.0b013e32831270d7.
131. Yin L, Duan J-J, Bian X-W, Yu S-c. Triple-negative breast cancer molecular subtyping and treatment progress. *Breast Cancer Research*. 2020;22(61)doi:10.1186/s13058-020-01296-5

132. Dent R, Trudeau M, Pritchard KI, et al. Triple-Negative Breast Cancer: Clinical Features and Patterns of Recurrence. *Clinical Cancer Research*. 2007;13(15):4429-4434. doi:10.1158/1078-0432.CCR-06-3045
133. Lu S, Yakirevich E, Wang LJ, Resnick MB, Wang Y. Cytokeratin 7-negative and GATA binding protein 3-negative breast cancers: Clinicopathological features and prognostic significance. *BMC Cancer*. 2019;19(1085)doi:10.1186/s12885-019-6295-8
134. Broglio K, Moulder SL, L. Hsu SK, et al. Prognostic impact of discordance/concordance of triple-receptor expression between primary tumor and metastasis in patients with metastatic breast cancer. *Journal of Clinical Oncology*. 2008;26(15):1000-10001. doi:10.1200/jco.2008.26.15_suppl.1001
135. Lengauer C, Kinzler KW, Vogelstein B. Genetic instabilities in human cancers. *Nature*. 1988;396(6712):643-649. doi:10.1038/25292
136. Thorsen F, Fite B, Mahakian LM, et al. Multimodal imaging enables early detection and characterization of changes in tumor permeability of brain metastases. *Journal of Controlled Release*. 2013;172(3):812-822. doi:10.1016/j.jconrel.2013.10.019
137. Lidster K, KathrynOwen, Browne WJ, Prescott MJ. Cage aggression in group-housed laboratory male mice: an international data crowdsourcing project. *Scientific Reports*. 2019;9(7)doi:10.1038/s41598-019-51674-z
138. Gao J, Li A, Hu J, Feng L, Liu L, Shen Z. Recent developments in isolating methods for exosomes. *Bioengineering and Biothecnology*. 2023;10doi:10.3389/fbioe.2022.1100892
139. Baranyai T, Herczeg K, Onódi Z, et al. Isolation of Exosomes from Blood Plasma: Qualitative and Quantitative Comparison of Ultracentrifugation and Size Exclusion Chromatography Methods. *PLoS One*. 2015;10(12)doi:10.1371/journal.pone.0145686
140. Livshts MA, Khomyakova E, Evtushenko EG, et al. Isolation of exosomes by differential centrifugation: Theoretical analysis of a commonly used protocol. *Scientific Reports*. 2015;5(1)doi:10.1038/srep17319
141. Chuo ST-Y, Chien JC-Y, Lai CP-K. Imaging extracellular vesicles: current and emerging methods. *Journal of Biomedical Science*. 2018;25(91)doi:10.1186/s12929-018-0494-5
142. Hu L, Wickline SA, Hood JL. Magnetic resonance imaging of melanoma exosomes in lymph nodes. *Magnetic Resonance in Medicine*. 2015;74(1):266-271. doi:10.1002/mrm.25376
143. Lyu TS, Ahn Y, Im Y-J, et al. The characterization of exosomes from fibrosarcoma cell and the useful usage of Dynamic Light Scattering (DLS) for their evaluation. *PLoS ONE*. 2021;16(1):1-14. doi:10.1371/journal.pone.0231994 J
144. Betzer O, Barnoy E, Sadan T, et al. Advances in imaging strategies for in vivo tracking of exosomes. *WIREs Nanomed Nanobiotechnology*. 2019;12(2)doi:10.1002/wnan.1594
145. Barjesteh T, Mansur S, Bao Y. Inorganic Nanoparticle-Loaded Exosomes for Biomedical Applications. *Molecules*. 2021;26(4)doi:10.3390/molecules26041135
146. JB M, JM M, EF C, A T, PH S, LF G. In vivo magnetic resonance imaging tracking of C6 glioma cells labeled with superparamagnetic iron oxide nanoparticles. *einstein*. 2012;10(2):164-170.
147. Ros PR, Freeny PC, Harms SE, et al. Hepatic MR Imaging with Ferumoxides: A Multicenter Clinical Trial ofthe Safety and Efficacy In the Detection ofFocal Hepatic Lesions'. *Radiology*. 1995;196(2):481-488. doi:10.1148/radiology.196.2.7617864
148. Wang Y-XJ. Superparamagnetic iron oxide based MRI contrast agents: Current status of clinical application. *Quantitative Imaging in Medical Surgery*. 2011;1(1):35-40. doi:10.3978/j.issn.2223-4292.2011.08.03
149. Sancho-Albero M, Encabo-Berzosa MdM, Beltrán-Visiedo M, et al. Efficient encapsulation of theranostic nanoparticles in cell-derived exosomes: leveraging the exosomal

biogenesis pathway to obtain hollow gold nanoparticle-hybrids. *The Royal Society of Chemistry*. 2019;11(18825-18836)doi:10.1039/c9nr06183e
150. Hood JL, Scott MJ, Wickline SA. Maximizing Exosome Colloidal Stability Following Electroporation. *Analytical Biochemistry*. 2014;448:41-49. doi:10.1016/j.ab.2013.12.001
151. Chen B, Le W, Wang Y, et al. Targeting Negative Surface Charges of Cancer Cells by Multifunctional Nanoprobes. *6*. 2016;(11):1887-1899. doi:10.7150/thno.16358
152. Cheng W, Ping Y, Zhang Y, Chuang K-H, Liu Y. Magnetic Resonance Imaging (MRI) Contrast Agents for Tumor Diagnosis. *Jounal of Healthcare Engineering*. 2013;4(1):23-46. doi:10.1260/2040-2295.4.1.23
153. Badman RP, Moore SL, Killian JL, et al. Dextran-coated iron oxide nanoparticle-induced nanotoxicity in neuron cultures. *Scientific Reports*. 2020;10(1)doi:10.1038/s41598-020-67724-w
154. Sundstrøm T, Daphu I, Wendelbo I, et al. Automated Tracking of Nanoparticle-labeled Melanoma Cells Improves the Predictive Power of a Brain Metastasis Model. *Cancer Research*. 2013;73(8):2445–2456. doi:10.1158/0008-5472.CAN-12-3514
155. Buck J, Perez-Balderas F, Zarhami N, et al. Imaging angiogenesis in an intracerebrally induced model of brain macrometastasis using αvβ3-targeted iron oxide microparticles. *NMR in Biomedicine*. 2021;doi:10.1002/nbm.4948